Accepted for publication in *The Astronomical Journal*
Preprint typeset using LaTeX style emulateapj v. 08/13/06

THE STAR FORMATION EFFICIENCY IN NEARBY GALAXIES: MEASURING WHERE GAS FORMS STARS EFFECTIVELY

Adam K. Leroy[1], Fabian Walter[1], Elias Brinks[2], Frank Bigiel[1], W.J.G. de Blok[3,4], Barry Madore[5], M. D. Thornley[6]

Accepted for publication in The Astronomical Journal

ABSTRACT

We measure the star formation efficiency (SFE), the star formation rate per unit gas, in 23 nearby galaxies and compare it to expectations from proposed star formation laws and thresholds. We use H I maps from THINGS and derive H_2 maps from CO measured by HERACLES and BIMA SONG. We estimate the star formation rate by combining GALEX FUV maps and SINGS 24μm maps, infer stellar surface density profiles from SINGS 3.6μm data, and use kinematics from THINGS. We measure the SFE as a function of: the free–fall and orbital timescales; midplane gas pressure; stability of the gas disk to collapse (including the effects of stars); the ability of perturbations to grow despite shear; and the ability of a cold phase to form. In spirals, the SFE of H_2 alone is nearly constant at $5.25 \pm 2.5 \times 10^{-10}$ yr^{-1} (equivalent to an H_2 depletion time of 1.9×10^9 yr) as a function of all of these variables at our 800 pc resolution. Where the ISM is mostly H I, on the other hand, the SFE decreases with increasing radius in both spiral and dwarf galaxies, a decline reasonably described by an exponential with scale length 0.2–0.25 r_{25}. We interpret this decline as a strong dependence of GMC formation on environment. The ratio of molecular to atomic gas appears to be a smooth function of radius, stellar surface density, and pressure spanning from the H_2–dominated to H I–dominated ISM. The radial decline in SFE is too steep to be reproduced only by increases in the free–fall time or orbital time. Thresholds for large–scale instability suggest that our disks are stable or marginally stable and do not show a clear link to the declining SFE. We suggest that ISM physics below the scales that we observe — phase balance in the H I, H_2 formation and destruction, and stellar feedback — governs the formation of GMCs from H I.

Subject headings: galaxies: evolution — galaxies: ISM — radio lines: galaxies — stars: formation

1. INTRODUCTION

In nearby galaxies, the star formation rate (SFR) is observed to correlate spatially with the distribution of neutral gas, at least to first order. This is observed using a variety of SFR and gas tracers, but the quantitative relationship between the two remains poorly understood. Although it is common to relate SFR to gas surface density via a power law, the relationship is often more complex. The same surface density of gas can correspond to dramatically different SFRs depending on whether it is found in a spiral or irregular galaxy or in the inner or outer part of a galactic disk. Such variations have spurred suggestions that the local potential well, pressure, coriolis forces, chemical enrichment, or shear may regulate the formation of stars from the neutral interstellar medium (ISM).

In this paper, we compare a suite of proposed star formation laws and thresholds to observations. In this way, we seek to improve observational constraints on theories of galactic-scale star formation. Such theories are relevant to galaxy evolution at all redshifts, but must be tested mainly in nearby galaxies, where observations have the spatial resolution and sensitivity to map star formation to local conditions. An equally important goal is to calibrate and test empirical star formation recipes. In lieu of a strict theory of star formation, such recipes remain indispensable input for galaxy modeling, particularly because star formation takes place mostly below the resolution of cosmological simulations. This requires the implementation of "subgrid" models that map local conditions to the SFR (e.g., Springel & Hernquist 2003).

Our analysis is based on the highest quality data available for a significant sample of nearby galaxies: H I maps from The H I Nearby Galaxy Survey (THINGS, Walter et al. 2008), far ultraviolet (FUV) maps from the GALEX Nearby Galaxies Survey (Gil de Paz et al. 2007), infrared (IR) data from the *Spitzer* Infrared Nearby Galaxies Survey (SINGS, Kennicutt et al. 2003), CO $1 \rightarrow 0$ maps from the BIMA Survey of Nearby Galaxies (BIMA SONG, Helfer et al. 2003) and CO $2 \rightarrow 1$ maps from the HERA CO-Line Extragalactic Survey (HERACLES Leroy et al. 2008). This combination yields sensitive, spatially resolved measurements of kinematics, gas surface density, stellar surface density, and SFR surface density across the entire optical disks of 23 spiral and irregular galaxies.

The topic of star formation in galaxies is closely linked to that of giant molecular cloud (GMC) formation. In the Milky Way, most star formation takes place in GMCs, which are predominantly molecular, gravitationally bound clouds with typical masses $\sim 10^5 - 10^6$ M$_\odot$

[1] Max-Planck-Institut für Astronomie, Königstuhl 17, D-69117, Heidelberg, Germany
[2] Centre for Astrophysics Research, University of Hertfordshire, Hatfield AL10 9AB, U.K.
[3] Research School of Astronomy & Astrophysics, Mount Stromlo Observatory, Cotter Road, Weston ACT 2611, Australia
[4] Department of Astronomy, University of Cape Town, Private Bag X3, Rondebosch 7701, South Africa
[5] Observatories of the Carnegie Institution of Washington, Pasadena, CA 91101, USA
[6] Department of Physics and Astronomy, Bucknell University, Lewisburg, PA, 17837, USA

(Blitz 1993). Similar clouds dominate the molecular ISM in Local Group galaxies (e.g., Fukui et al. 1999; Engargiola et al. 2003). If the same is true in other galaxies, then a close association between GMCs and star formation would be expected to be a general feature of our data. Bigiel et al. (2008) study the relationship between atomic hydrogen (H I), molecular gas (H_2), and the SFR in the same data used here. Working at a resolution of 750 pc, they do not resolve individual GMCs, but do find that a single power law with index $n = 1.0 \pm 0.2$ relates H_2 and SFR surface density over the optical disks of spirals. This suggests that as in the Milky Way, a key prerequisite to forming stars is the formation of GMCs (or at least H_2).

Bigiel et al. (2008) find no similar trend relating H I and SFR. Instead the ratios of H_2-to-H I and SFR-to-H I vary strongly within and among galaxies. GMC formation, therefore, appears to be a function of local conditions. Here we investigate this dependence. We focus on where the ISM can form gravitationally bound, predominantly molecular structures, i.e., the "star formation threshold," and investigate how the molecular fraction of the ISM varies with local conditions. In equilibrium, the fraction of the ISM in GMCs may be set by the timescale over which these structures form. Therefore we also consider suggested timescales for the formation of GMCs and compare them to observations.

Maps with good spatial coverage and sensitivity are critical to distinguish between the various proposed thresholds and timescales. Perhaps *the* key observation to test theories of galactic–scale star formation is that the star formation per unit gas mass decreases in the outer disks of spiral and irregular galaxies (e.g., Kennicutt 1989; Martin & Kennicutt 2001; Thornley et al. 2006). The details of this decrease vary with the specifics of the observations. For example, Martin & Kennicutt (2001) observed a sharp drop in the distribution of H II regions, while UV maps suggest a steady decline (Boissier et al. 2007), but it is without dispute that the SFR per unit gas mass does indeed decline (see also Wong & Blitz 2002). Maps with good spatial extent contain both regions where GMC formation proceeds efficiently and regions where it is suppressed. Including both H I-rich dwarf galaxies and H_2-dominated spirals offers a similar contrast.

In §2, we present a set of star formation laws and thresholds that we will compare to observations. We phrase these in terms of the star formation per unit neutral gas, which we call the "star formation efficiency." This quantity, the inverse of the gas depletion time, removes the basic scaling between stars and gas and measures how effectively each parcel of the ISM forms stars.

In §3, we briefly describe our sample, data, and methodology. In order to focus the main part of the paper on analysis, we defer most detailed discussion of data and methodology to the appendices.

In §4 we look at how the star formation efficiency relates to other basic quantities (§4.1), proposed laws (§4.2), and thresholds (§4.3) described in §2. In §5 we analyze and interpret these results. In §6, we illustrate our conclusions by comparing predictions for the star formation efficiency to observations. In §7, we summarize our results.

Appendices A – D contain all the information required to reproduce our calculations, including descriptions of the data and how we convert from observables to physical quantities. We present our data as an electronic table of radial profiles described in Appendix E and as maps and plotted profiles for each galaxy in Appendix F.

2. BACKGROUND

Following, e.g., Kennicutt (1989), we break the topic of star formation in galaxies into two parts. Where star formation is widespread, we refer to the quantitative relationship between neutral gas and the SFR as the star formation *law*. To predict the SFR over an entire galactic disk, it is also necessary to know which gas is actively forming stars. This topic is often phrased as the star formation *threshold*, but may be more generally thought of as the problem of where a cold phase ($n \sim 4$–80 cm^{-3}, $T \sim 50$–200 K) or gravitationally bound clouds can form; both are thought to be prerequisites to star formation. We give a brief background on both laws and thresholds, first noting that neither term is strictly accurate: "laws" here refer to observed (or predicted) correlations and the "threshold" is probably a smooth variation from non-star forming to actively star forming gas.

We cast this discussion in terms of the *star formation efficiency* (SFE). There are many definitions for the SFE, but throughout this paper we use the term only to refer to the star formation rate surface density per unit neutral gas surface density along a line of sight, i.e., SFE$=\Sigma_{\rm SFR}/\Sigma_{\rm gas}$ with units of yr^{-1}. We will also discuss SFE (H_2) which refers to the SFR per unit H_2 ($\Sigma_{\rm SFR}/\Sigma_{\rm H2}$), and SFE (H I) ($\Sigma_{\rm SFR}/\Sigma_{\rm HI}$). The SFE is the inverse of the gas depletion time, the time required for present day star formation to consume the gas reservoir. It represents a combination of the real timescale for neutral gas to form stars and the fraction of gas that ends up in stars, e.g., if 1% of the gas is converted to stars every 10^7 yr, the SFE$= 10^{-9}$ yr^{-1}. Because it is normalized by $\Sigma_{\rm gas}$, the SFE is more useful than $\Sigma_{\rm SFR}$ alone to identify where conditions are conducive to star formation (i.e., where gas is "good at forming stars").

As we describe proposed laws (§2.1) and thresholds (§2.2), we present quantitative forms for each that can be compared to the observed SFE. Table 1 collects these expressions, which we compare to observations in §4.

2.1. *Star Formation Laws*

A star formation law should predict the SFE from local conditions. Here we describe three proposals for the limiting timescale over which gas forms stars: the free-fall timescale in the gas disk, the orbital timescale, and the characteristic timescale for cloud-cloud collisions. We also describe proposals that GMCs form stars with a fixed SFE and that the midplane gas pressure regulates the fraction of the ISM in the molecular phase. We present each proposal as a prediction for the SFE in terms of observables. These appear together in the upper part of Table 1. We expect a successful star formation law to reproduce the observed SFE (in practice, combined with an empirical calibration).

2.1.1. *Disk Free-Fall Time With Fixed Scale Height*

The most common formulation of the star formation law is a power law relating gas and star formation (sur-

TABLE 1
STAR FORMATION LAWS AND THRESHOLDS

Theory	Form	Observables
Star Formation Laws		
disk free–fall time		
. . . fixed scale height	$\mathrm{SFE} \propto \Sigma_{\rm gas}^{0.5}$	$\Sigma_{\rm gas}$
. . . variable scale height	SFE or $R_{\rm mol} \propto \frac{\Sigma_{\rm gas}}{\sigma_{\rm g}} \left(1 + \frac{\Sigma_*}{\Sigma_{\rm gas}} \frac{\sigma_{\rm g}}{\sigma_{*,z}}\right)^{0.5}$	$\Sigma_{\rm gas}$, Σ_*, σ_g, σ_*
orbital timescale	SFE or $R_{\rm mol} \propto \tau_{\rm orb}^{-1} = \frac{v(r_{\rm gal})}{2\pi r_{\rm gal}}$	$v(r_{\rm gal})$
cloud-cloud collisions	$\mathrm{SFE} \propto \tau_{\rm orb}^{-1}\ Q_{\rm gas}^{-1}\ (1 - 0.7\ \beta)$	$v(r_{\rm gal})$
fixed GMC efficiency	$\mathrm{SFE} = \mathrm{SFE}\,(\mathrm{H_2})\ \frac{R_{\rm mol}}{R_{\rm mol}+1}$	$\Sigma_{\rm H2}$
pressure and ISM phase	$R_{\rm mol} \propto \left(\Sigma_{\rm gas}\ \left(\Sigma_{\rm gas} + \frac{\sigma_{\rm g}}{\sigma_{*,z}}\Sigma_*\right)\ P_0^{-1}\right)^{1.2}$	$\Sigma_{\rm gas}$, Σ_*, $\sigma_{\rm g}$, σ_*
Star Formation Thresholds		
gravitational instability		
. . . in the gas disk	$Q_{\rm gas} = \left(\frac{\sigma_g\ \kappa}{\pi\ G\ \Sigma_{\rm gas}}\right) < 1$	$\Sigma_{\rm gas}$, $\sigma_{\rm g}$, $v(r_{\rm gal})$
. . . in a disk of gas and stars	$Q_{\rm stars+gas} = \left(\frac{2}{Q_{\rm stars}}\frac{q}{1+q^2} + \frac{2}{Q_{\rm gas}}\ R\ \frac{q}{1+q^2R^2}\right)^{-1} < 1$	$\Sigma_{\rm gas}$, Σ_*, $\sigma_{\rm g}$, σ_*, $v(r_{\rm gal})$
competition with shear	$\Sigma_{\rm gas} > \frac{2.5\ A\ \sigma_g}{\pi\ G}$	$\Sigma_{\rm gas}$, $\sigma_{\rm g}$, $v(r_{\rm gal})$
cold gas phase	$\Sigma_{\rm gas} > 6.1\ \mathrm{M_\odot\ pc^{-2}}\ f_{\rm g}^{0.3}\ Z^{-0.3}\ I^{0.23}$	$\Sigma_{\rm gas}$, Σ_*, Z, I

face) densities following Schmidt (1959, 1963). Kennicutt (1989, 1998a) calibrated this law in its observable (surface density) form. Averaging over the star-forming disks of spiral and starburst galaxies, he found

$$\Sigma_{\rm SFR} \propto \Sigma_{\rm gas}^{1.4}\ , \tag{1}$$

often referred to as the "Kennicutt–Schmidt law."

The exponent in Equation 1, $n \approx 1.5$, can be approximately explained by arguing that stars form with a characteristic timescale equal to the free–fall time in the gas disk, which in turn depends inversely on the square root of the gas volume density, $\tau_{\rm ff} \propto \rho_{\rm gas}^{-0.5}$ (e.g., Madore 1977). For a fixed scale height $\rho_{\rm gas} \propto \Sigma_{\rm gas}$ and $\Sigma_{\rm SFR} \propto \Sigma_{\rm gas}^{1.5}$. The first star formation law that we consider is thus

$$\mathrm{SFE} \propto \Sigma_{\rm gas}^{0.5}\ , \tag{2}$$

which is approximately Equation 1.

2.1.2. *Disk Free-Fall Time With Variable Scale Height*

If the scale height is not fixed, but instead set by hydrostatic equilibrium in the disk, then

$$\tau_{\rm ff} \propto \frac{1}{\sqrt{\rho_{\rm mp,gas}}} \propto \frac{\sigma_{\rm g}}{\Sigma_{\rm gas}\ \sqrt{1 + \frac{\Sigma_*}{\Sigma_{\rm gas}}\frac{\sigma_{\rm g}}{\sigma_{*,z}}}} \tag{3}$$

where $\sigma_{\rm g}$ and $\sigma_{*,z}$ are the (vertical) velocity dispersions of gas and stars, $\Sigma_{\rm gas}$ and Σ_* are the surface densities of the same, and $\rho_{\rm mp,gas}$ is the midplane gas density. Equation 3 combines the expression for midplane density from Krumholz & McKee (2005, their Equation 34) and midplane gas pressure from Elmegreen (1989, his Equation 11, used to calculate ϕ_P). The second star formation law that we consider is

$$\mathrm{SFE} \propto \tau_{\rm ff}^{-1} \propto \frac{\Sigma_{\rm gas}}{\sigma_{\rm g}}\ \left(1 + \frac{\Sigma_*}{\Sigma_{\rm gas}}\frac{\sigma_{\rm g}}{\sigma_{*,z}}\right)^{0.5}\ , \tag{4}$$

which incorporates variations in the scale height and thus gas volume density with a changing potential well.

2.1.3. *Orbital Timescale*

It is also common to equate the timescale for star formation and the orbital timescale (e.g., Silk 1997; Elmegreen 1997). Kennicutt (1998a) and Wong & Blitz (2002) found that such a formulation performs as well as Equation 1. In this case

$$\mathrm{SFE} \propto \tau_{\rm orb}^{-1} = \frac{\Omega}{2\pi} = \frac{v(r_{\rm gal})}{2\pi r_{\rm gal}}\ . \tag{5}$$

where $v(r_{\rm gal})$ is the rotational velocity at a galactocentric radius $r_{\rm gal}$ and Ω is the corresponding angular velocity.

2.1.4. *Cloud–Cloud Collisions*

Tan (2000) suggested that the rate of collisions between gravitationally bound clouds sets the timescale for star formation so that

$$\mathrm{SFE} \propto \tau_{\rm orb}^{-1}\ Q_{\rm gas}^{-1}\ (1 - 0.7\beta)\ . \tag{6}$$

where $Q_{\rm gas}$, defined below, measures gravitational instability in the disk and $\beta = d\log\ v(r_{\rm gal})/d\log\ r_{\rm gal}$ is the logarithmic derivative of the rotation curve. The dependence on β reflects the importance of galactic shear in setting the frequency of cloud-cloud collisions. In the limit $\beta = 0$ (a flat rotation curve) this prescription reduces to essentially Equation 5; for $\beta = 1$ (solid body rotation) the SFE is depressed by the absence of shear.

2.1.5. *Fixed GMC Efficiency*

If the SFE of an individual GMC depends on its intrinsic properties and if these properties are not themselves strong functions of environment or cloud formation, then we expect a fixed SFR per unit molecular gas, SFE ($\mathrm{H_2}$). Krumholz & McKee (2005) posited such a case, arguing that the SFE of a GMC depends on the free–fall time in the cloud, itself only a weak function of cloud mass in the Milky Way (Solomon et al. 1987). Bigiel et al. (2008) found support for this idea. Studying the same data used here, they derived a linear relationship between $\Sigma_{\rm H2}$ and $\Sigma_{\rm SFR}$ on scales of 750 pc.

SFE ($\mathrm{H_2}$) is likely to appear constant if: the scaling relations and mass spectrum (i.e., the intrinsic properties) of GMCs are approximately universal, the gas pressure is low enough that GMCs are largely decoupled from the rest of the ISM, individual resolution elements contain at least a few GMCs, and the properties of a cloud regulate its ability to form stars (§5.1 and Bigiel et al. 2008). This is the fifth star formation law that we consider, that star formation in spiral galaxies occurs mostly in GMCs and that once such clouds are formed, they have approximately uniform properties so that

$$\text{SFE}\ (\text{H}_2) = \text{constant}\ , \tag{7}$$

which we can convert to the SFE of the total gas given $R_{\rm mol} = \Sigma_{\rm H2}/\Sigma_{\rm HI}$, the ratio of H_2 to H I gas. Then

$$\text{SFE} = \text{SFE}\ (\text{H}_2)\,\frac{R_{\rm mol}}{R_{\rm mol}+1} \tag{8}$$

or if we measure only $\Sigma_{\rm HI}$ (as is the case in dwarfs), then SFE (HI) = SFE (H_2) $R_{\rm mol}$.

The balance between GMC/H_2 formation and destruction will set $R_{\rm mol} = \Sigma_{\rm H2}/\Sigma_{\rm HI}$. If GMCs with fixed lifetime form over a free fall time or orbital time then $R_{\rm mol} \propto \tau_{\rm ff}^{-1}$ or $R_{\rm mol} \propto \tau_{\rm orb}^{-1}$ (§5.4), which we have noted in Table 1. Combined with Equation 8, an expression for $R_{\rm mol}$ predicts the SFE.

2.1.6. *Pressure and Phase of the ISM*

Wong & Blitz (2002), Blitz & Rosolowsky (2004), and Blitz & Rosolowsky (2006) explicitly consider $R_{\rm mol}$. Following Elmegreen (1989) and Elmegreen & Parravano (1994), they identify pressure as the critical quantity that sets the ability of the ISM to form H_2. They show that the midplane hydrostatic gas pressure, $P_{\rm h}$, correlates with this ratio in the inner parts of spiral galaxies.

Pressure, which is directly proportional to the gas volume density, should affect both the rate of H_2 formation/destruction and the likelihood of a gravitationally unstable overdensity condensing out of a turbulent ISM (Elmegreen 1989; Elmegreen & Parravano 1994). Elmegreen (1989) gives the following expression for $P_{\rm h}$,

$$P_{\rm h} \approx \frac{\pi}{2}\ G\ \Sigma_{\rm gas}\ \left(\Sigma_{\rm gas} + \frac{\sigma_{\rm g}}{\sigma_{*,z}}\Sigma_*\right)\ , \tag{9}$$

and Elmegreen (1993) predicted that the fraction of gas in the molecular phase depends on both $P_{\rm h}$ and the interstellar radiation field, j, via $R_{\rm mol} \propto P^{2.2}\ j^{-1}$. If $\Sigma_{\rm SFR} \propto \Sigma_{\rm H2}$ and we make the simple assumption that $j \propto \Sigma_{\rm SFR}$ then Elmegreen (1993) predicts

$$R_{\rm mol} \propto\ P_h^{1.2}\ \ \text{or}\ \Sigma_{\rm H2} = \Sigma_{\rm HI} P_h^{1.2}\ , \tag{10}$$

which combines with Equation 8 to predict the SFE.

Wong & Blitz (2002) and Blitz & Rosolowsky (2006) found observational support for Equation 10. Using a modified Equation 9 appropriate where $\Sigma_* \gtrsim \Sigma_{\rm gas}$, Blitz & Rosolowsky (2006) fit a power law of the form

$$R_{\rm mol} = \frac{\Sigma_{\rm H2}}{\Sigma_{\rm HI}} = \left(\frac{P_h}{P_0}\right)^{\alpha}\ , \tag{11}$$

finding $P_0 = 4.3 \times 10^4$ cm^{-3} K, the observed pressure where the ISM is equal parts H I and H_2, and a best–fit exponent $\alpha = 0.92$. Wong & Blitz (2002) found $\alpha = 0.8$. Robertson & Kravtsov (2008) recently found support from simulations for $\alpha \sim 0.9$.

2.2. *Star Formation Thresholds*

We have described suggestions for the efficiency with which gas form stars, but not *whether* gas forms stars. A "star formation threshold" is often invoked to accompany a star formation law. This is a criterion designed to address the question "which gas is actively forming stars?" or "where can the ISM form gravitationally bound, molecular clouds?" and proposed thresholds have mostly focused on the existence of gravitational or thermal instability in the gas disk.

A common way to treat the issue of thresholds is to formulate a critical gas surface density, $\Sigma_{\rm crit}$, that is a function of local conditions — kinematics, stellar surface density, or metallicity. If $\Sigma_{\rm gas}$ is below $\Sigma_{\rm crit}$, star formation is expected to be suppressed; we refer to such regions as "subcritical." Where the gas surface density is above the critical surface density, star formation is expected to be widespread. We refer to such regions as "supercritical."

In practice, we expect to observe a drop in the SFE associated with the transition from super- to subcritical. We do not necessarily expect SFE = 0 in subcritical regions. Even with excellent resolution, a line of sight through a galaxy probes a range of physical conditions. At our working resolution of 400 – 800 pc, each resolution element encompasses a wide range of local conditions. Within a subcritical resolution element, star formation may still occur in isolated pockets that locally meet the threshold criterion.

Expressions for star formation thresholds are collected in the lower part of Table 1.

2.2.1. *Gravitational Instability*

Kennicutt (1989), Kennicutt (1998a), and Martin & Kennicutt (2001) argued that star formation is only widespread where the gas disk is unstable against large scale collapse. Following Toomre (1964), the condition for instability in a thin gas disk is

$$Q_{\rm gas} = \frac{\sigma_g\ \kappa}{\pi\ G\ \Sigma_{\rm gas}}\ < 1\ . \tag{12}$$

where σ_g is the gas velocity dispersion, G is the gravitational constant, and κ is the epicyclic frequency, calculated via

$$\kappa = 1.41\ \frac{v(r_{\rm gal})}{r_{\rm gal}}\ \sqrt{1+\beta}\ , \tag{13}$$

where $\beta = d\log\ v(r_{\rm gal})/d\log\ r_{\rm gal}$.

Martin & Kennicutt (2001) found that H II regions are common where $\Sigma_{\rm gas}$ exceeds a critical surface density derived following Equation 12,

$$\Sigma_{{\rm crit},Q} = \alpha_Q\ \frac{\sigma_g\ \kappa}{\pi\ G}\ . \tag{14}$$

In regions where $\Sigma_{\rm gas}$ is above this threshold, gas is unstable against large scale collapse, which leads to star formation. Below the threshold, Coriolis forces counteract the self-gravity of the gas and suppress cloud/star formation. The factor α_Q is an empirical calibration, the observed average value of $1/Q_{\rm gas}$ at the star formation threshold. For an ideal thin gas disk, the condition for gas to be unstable to collapse is $\alpha_Q > 1$.

At the edge of star forming disks, Kennicutt (1989) found $\alpha_Q = 0.63$ and Martin & Kennicutt (2001) found $\alpha_Q = 0.69$ ($Q_{\rm gas} \sim 1.5$).

Kennicutt (1989) and Martin & Kennicutt (2001) mention the influence of stars as a possible cause for $Q_{\rm gas} > 1$ at the star formation threshold. Hunter et al. (1998a) present an in-depth discussion of how several factors influence α_Q, e.g., stars and viscosity lower it, while the thickness of the gas disk raises it. Kim & Ostriker (2001, 2007) argue based on simulations that the observed threshold corresponds to the onset of nonlinear, non-axisymmetric instabilities. Schaye (2004) and de Blok & Walter (2006) suggest a different explanation, that $\alpha_Q \neq 1$ because σ_g has been systematically mishandled; they point out that σ_g measured from 21-cm emission will overestimate the true velocity dispersion of gas in a cold phase.

The stellar potential well may substantially affect the stability of the gas disk. Rafikov (2001) extended work by Jog & Solomon (1984) to provide a straightforward way to calculate the instability of a gas disk in the presence of a collisionless stellar disk. Rafikov defined

$$Q_{\rm stars} = \frac{\sigma_{*,r}\ \kappa}{\pi\ G\ \Sigma_*} \qquad (15)$$

where $\sigma_{*,r}$ is the (radial) velocity dispersion of stars and Σ_* is the stellar mass surface density. The condition for instability in the gas disk is

$$\frac{1}{Q_{\rm stars+gas}} = \frac{2}{Q_{\rm stars}} \frac{q}{1+q^2} + \frac{2}{Q_{\rm gas}}\ R\ \frac{q}{1+q^2R^2} > 1\ , \qquad (16)$$

where $q = k\sigma_{*,r}/\kappa$, with k the wavenumber of the instability being considered, and $R = \sigma_{\rm g}/\sigma_{*,r}$. The minimum value of $Q_{\rm stars+gas}$ indicates whether the gas disk is unstable to large scale collapse. In our sample, typical values of q correspond to wavelengths $\lambda = 2\pi/k \approx$ 1–5 kpc.

Hunter et al. (1998a) and Blitz & Rosolowsky (2004) observed strong correlations between star and GMC formation and the distribution of stars, consistent with stellar gravity playing a key role in star formation. Yang et al. (2007) recently showed that $Q_{\rm stars+gas}$ does an excellent job of predicting the location of star formation in the Large Magellanic Cloud and Boissier et al. (2003) showed that including stars improves the correspondence between Q and star formation in disk galaxies. Li et al. (2005, 2006) found the same results from numerical simulations of disk galaxies, i.e., that stability against large scale collapse depends critically on the stellar potential well, with star formation where $Q_{\rm stars+gas} \lesssim 1.6$.

2.2.2. *Galactic Shear*

Motivated by the failure of the Toomre $Q_{\rm gas}$ threshold in dwarf irregular galaxies, Hunter et al. (1998a) suggested that collecting the material for cloud formation may be easier than implied by $Q_{\rm gas}$, e.g., through the aid of magnetic fields (see also Kim & Ostriker 2001). They hypothesize that the destructive influence of galactic shear may instead limit where GMCs can form and describe a threshold that depends on the ability of clouds to form in the time allowed by shear.

This threshold is based on the local shear rate, described by Oort's A constant

$$A = -0.5\ r_{\rm gal}\ \frac{d\Omega}{dr_{\rm gal}}\ . \qquad (17)$$

Substituting $\Omega = v(r_{\rm gal})/r_{\rm gal}$,

$$A = 0.5\ \left(\frac{v(r_{\rm gal})}{r_{\rm gal}} - \frac{dv(r_{\rm gal})}{dr_{\rm gal}}\right) = 0.5\ \frac{v(r_{\rm gal})}{r_{\rm gal}}\ (1-\beta) \qquad (18)$$

Then the threshold has the form

$$\Sigma_{\rm crit,A} = \frac{\alpha_A\ \sigma_g\ A}{\pi\ G}\ . \qquad (19)$$

Hunter et al. (1998a) suggest $\alpha_{\rm A} = 2.5$, but this normalization for $\Sigma_{\rm crit,A}$ is relatively uncertain. The value chosen by Hunter et al. (1998a) corresponds to perturbations growing by a factor of ~ 100 during the time allowed by shear, which roughly matches both the surface density contrast between $\Sigma_{\rm HI}$ and a GMC and the condition $Q_{\rm gas} \lesssim 1$ where $dv(r_{\rm gal})/dr_{\rm gal} = 0$.

The practical advantage of shear over $Q_{\rm gas}$ is that shear is low in dwarf galaxies and the inner disks of spiral galaxies ($\beta = 1$ for solid body rotation), both locales where widespread star formation is observed. In the outer disks of spiral galaxies — where star formation cutoffs are observed — rotation curves tend to be flat ($\beta = 0$) so that $\Sigma_{\rm crit,A}$ and $\Sigma_{\rm crit,Q}$ reduce to the same form.

2.2.3. *Formation of a Cold Phase*

The very long time needed to assemble a massive GMC from coagulation of smaller clouds suggests that most GMCs in galaxy disks form "top down" (e.g., McKee & Ostriker 2007). However this does not necessarily require that the whole gas disk to be unstable. Where cold H I is abundant, the lower velocity dispersion associated with this phase may render the ISM locally unstable (Schaye 2004), leading to the formation of GMCs and stars.

Therefore, instead of large-scale gravitational instability or cloud destruction by shear, the ability to form a cold neutral medium (McKee & Ostriker 1977; Wolfire et al. 2003) may regulate GMC formation. Schaye (2004) argues based on modeling that near the cutoffs observed by Martin & Kennicutt (2001) gas becomes mostly cold H I and H_2, σ_g drops accordingly, and Q becomes < 1 in the cold gas. In a similar vein, Elmegreen & Parravano (1994) suggest that the star formation efficiency in the outer parts of galaxies drops because the pressure becomes too low to allow a cold phase to form even given perturbations, e.g., from supernova shocks. Braun (1997) found support for this idea using 21–cm observations; he associated networks of high surface brightness filaments with cold H I and showed that these filaments are pervasive across the star forming disk, but become less common at large radii (though work on THINGS by Usero et al. 2008, calls this result into question).

Schaye (2004) modeled the ISM to estimate where the average temperature drops to ≈ 500 K, the molecular fraction reaches $\approx 10^{-3}$, and $Q_{\rm gas} \approx 1$; good indicators that cold H I is common and H_2 formation is efficient. These all occur where $\Sigma_{\rm gas}$ exceeds

$$\Sigma_{\rm S04} \approx \frac{6.1}{{\rm M_\odot\ pc^{-2}}}\ f_{\rm g}^{0.3}\ \left(\frac{Z}{0.1 Z_\odot}\right)^{-0.3}\ \left(\frac{I}{10^6\ {\rm cm^{-2}\ s^{-1}}}\right)^{0.23}, \qquad (20)$$

where $f_g \approx \Sigma_{gas}/(\Sigma_{gas}+\Sigma_*)$ is the fraction of mass in gas (we assume a two-component disk), Z is the metallicity of the ISM, and I is the flux of ionizing photons. Σ_{S04} also depends on the ratio of thermal to turbulent pressure and higher order terms not shown here. Schaye (2004) selects fiducial values to match those expected in outer galaxy disks, but concludes that the influence of Z, f_g, and the radiation field is relatively small. Most reasonable values yield $\Sigma_{S04} \approx 3 - 10$ M$_\odot$ pc^{-2}.

Schaye (2004) argues that a simple column density threshold may work as well as dynamical thresholds. This agrees with the observation by, e.g., Skillman (1987) and de Blok & Walter (2006) that a simple H I column density threshold does a good job of predicting the location of star formation in dwarf irregulars. This threshold, $\Sigma_{HI} \approx 10$ M$_\odot$ pc^{-2}, also corresponds to the surface density above which H I is observed to saturate (Martin & Kennicutt 2001; Wong & Blitz 2002; Bigiel et al. 2008); that is, gas in excess of this surface density in spiral galaxies is in the molecular phase.

3. DATA

The right hand column of Table 1 lists the observables required to evaluate each law or threshold. We require estimates of: the surface density of atomic gas (Σ_{HI}), molecular gas (Σ_{H2}), star formation rate (Σ_{SFR}), and stellar mass (Σ_*), the velocity dispersions of gas and stars (σ_{gas} and σ_*), and the rotation curve ($v(r_{gal})$). Estimates of the metallicity await future work.

3.1. *The Sample*

We assemble maps and radial profiles of the necessary quantities in 23 nearby, star–forming galaxies that we list in order of increasing stellar mass in Table 2. These are galaxies for which we could compile the necessary data, which means the overlap of THINGS, SINGS, the GALEX NGS, and (for spirals) either BIMA SONG or HERACLES.

We work with two subsamples: 11 H I-dominated, low-mass galaxies and 12 large spiral galaxies. In Table 2, the galaxies that we classify "dwarf galaxies" lie above the horizontal dividing line. These have rotation velocities $v_{rot} \lesssim 125$ km s^{-1}, stellar masses $M_* \lesssim 10^{10}$ M$_\odot$, and $M_B \gtrsim -20$ mag. The galaxies that we label "spirals" lie below the dividing line and have $v_{rot} \gtrsim 125$ km s^{-1}, $M_* \gtrsim 10^{10}$ M$_\odot$, and $M_B \lesssim -20$ mag.

This division allows us to explore two distinct regimes in parallel. Compared to their larger cousins, dwarf galaxies have low metallicities, intense radiation fields, lower galactic shear, and weak or absent spiral structure. Metallicity, in particular, should have a strong effect on the thermal balance of the ISM. In lieu of direct measurements, separating the sample in this way allows us to assess its impact.

We treat the two subsamples slightly differently in two ways. First, we place data for spirals at a common spatial resolution of 800 pc and data for dwarf galaxies at 400 pc. The spirals in our sample are farther away than the dwarf galaxies with larger physical radii, and this approach ensures a good number of resolution elements across each galaxy and a fairly uniform angular resolution of $\sim 20''$ (see Table 2).

Second, we use CO maps combined with a constant CO-to-H_2 conversion factor, X_{CO}, to derive Σ_{H2} in spirals, while we treat the molecular gas content of dwarf galaxies as unknown (see Appendix A.3). CO emission in very low mass galaxies is usually weak or not detected (e.g., Taylor et al. 1998; Leroy et al. 2005, and see Table 4) and its interpretation is confused by potential variations in X_{CO}. Because dwarf galaxies lack H_2-filled H I depressions like those observed in the centers of spirals, we expect Σ_{HI} to at least capture the basic morphology of the total gas. Although we do not measure Σ_{H2} in dwarf galaxies, we consider our results in light of the possibility of an unseen reservoir of molecular gas (§5.3).

TABLE 2
SAMPLE GALAXIES

Galaxy[a]	Res.[b] ($''$)	CO	Rotation Curve[c]	Also in sample of[d]
DDO 154	19	...	dB	...
Ho I	21	...	T	...
Ho II	24	...	T	...
IC 2574	21	...	dB	...
NGC 4214[e]	28	...	T	...
NGC 2976	23	...	dB	...
NGC 4449[e]	20	...	...	...
NGC 3077[e]	22	...	...	...
NGC 7793	21	...	dB	...
NGC 925	9	...	dB	1, 2, 4
NGC 2403	26	...	dB	1, 2, 4
NGC 628	23	HERACLES	T	1, 2
NGC 3198	12	HERACLES	dB	...
NGC 3184	15	HERACLES	T	...
NGC 4736	35	HERACLES	dB	1, 2, 3, 5
NGC 3351	16	HERACLES	T	...
NGC 6946	28	HERACLES	dB	2
NGC 3627	18	BIMA SONG	dB	5
NGC 5194	21	BIMA SONG	T	2, 4, 5
NGC 3521	15	HERACLES	dB	5
NGC 2841	12	HERACLES	dB	1, 2
NGC 5055	16	HERACLES	dB	2, 3, 5
NGC 7331	11	HERACLES	dB	2, 5

[a]In order of increasing stellar mass.
[b]Angular resolution to match working spatial resolution in the subsample, 400 pc for dwarf galaxies and and 800 pc for spirals.
[c]Rotation curve data: dB = de Blok et al. (2008); T = only THINGS first moment (Walter et al. 2008)
[d]1: Kennicutt (1989); 2: Martin & Kennicutt (2001); 3: Wong & Blitz (2002); 4: Boissier et al. (2003); 5: Blitz & Rosolowsky (2006)
[e]IR data from *Spitzer* archive (not SINGS).

3.2. *Data to Physical Quantities*

Appendices A – D explain in detail how we translate observables into physical quantities. Here and in Table 3 we summarize this mapping.

Atomic Hydrogen Surface Density (Appendix A): We derive atomic gas mass surface density, Σ_{HI}, from 21-cm line integrated intensity maps obtained by Walter et al. (2008) as part of the THINGS survey using the Very Large Array[7]. Σ_{HI} is corrected for inclination and includes a factor of 1.36 to account for helium.

Molecular Hydrogen Surface Density (Appendix A): In spirals, we estimate the molecular gas mass surface density, Σ_{H2}, from CO line emission. For 10 galaxies

[7] The VLA is operated by the National Radio Astronomy Observatory, which is a facility of the National Science Foundation operated under cooperative agreement by Associated Universities, Inc.

TABLE 3
DATA TO PHYSICAL QUANTITIES

Quantity	Observation	Survey	Reference	Key Assumptions
$\Sigma_{\rm HI}$	21-cm line	THINGS	Walter et al. (2008)	
$\Sigma_{\rm H2}$ (spirals only)	CO $2 \rightarrow 1$	HERACLES	Leroy et al. (2008)	fixed line ratio, CO-to-H_2 conversion
	CO $1 \rightarrow 0$	BIMA SONG	Helfer et al. (2003)	fixed CO-to-H_2 conversion
Unobscured $\Sigma_{\rm SFR}$	FUV	GALEX NGS	Gil de Paz et al. (2007)	
Embedded $\Sigma_{\rm SFR}$	24μm	SINGS	Kennicutt et al. (2003)	
Σ_*	3.6μm	SINGS	Kennicutt et al. (2003)	$\Upsilon_\star^K = 0.5\ M_\odot/L_{\odot,K}$
Kinematics	21-cm line	THINGS	de Blok et al. (2008)	simple functional fit; fixed $\sigma_{\rm gas}$

we use data from HERACLES, a large program at the IRAM[8] 30–m telescope (Leroy et al. 2008) that used the HERA focal plane array (Schuster et al. 2004) to map a subsample of THINGS in the CO $J = 2 \rightarrow 1$ line. For NGC 3627 and NGC 5194, we use $J = 1 \rightarrow 0$ line maps from the BIMA SONG survey (Helfer et al. 2003).

We convert from CO line intensity to $\Sigma_{\rm H2}$ assuming a constant CO-to-H_2 conversion factor appropriate for the solar neighborhood, $X_{\rm CO} = 2 \times 10^{20}$ cm^{-2} (K km s^{-1})$^{-1}$, and a fixed line ratio $I_{\rm CO}(2 \rightarrow 1) = 0.8\ I_{\rm CO}(1 \rightarrow 0)$, typical of the disks of spiral galaxies. We correct for the effects of inclination and include a factor of 1.36 to reflect the presence of helium .

Galactic Rotation (Appendix B): We fit a simple functional form to the high quality rotation curves derived from THINGS by de Blok et al. (2008) and the THINGS first moment maps (Walter et al. 2008). These fits yield smooth, well–behaved (analytic) derivatives and match the observations well. Two galaxies (NGC 3077 and NGC 4449) have complex velocity fields that require substantial effort to interpret and we omit them from analyses requiring kinematics.

Gas Velocity Dispersion (Appendix B): We assume a fixed gas velocity dispersion, $\sigma_{\rm gas} = 11$ km s^{-1}, a value motivated by the THINGS second moment maps.

Stellar Velocity Dispersion (Appendix B): We estimate the vertical stellar velocity dispersion, $\sigma_{*,z}$, from hydrostatic equilibrium, the assumption of an isothermal disk, and an estimated (radially invariant) stellar scale height. We derive this scale height for each galaxy from our measured stellar scale length and an average flattening ratio for disk galaxies. We take the vertical and radial velocity dispersions to be related by $\sigma_{*,z} = 0.6\ \sigma_{*,r}$.

Stellar Surface Density (Appendix C): We estimate the stellar surface density, Σ_*, from *Spitzer* 3.6μm maps, mostly from SINGS (Kennicutt et al. 2003). To avoid contamination by hot dust and foreground stars, we construct radial profiles only, using the median 3.6μm intensity in each tilted ring. We convert from 3.6μm intensity to Σ_* via an empirical K-to-3.6μm calibration and adopt a fixed K-band mass-to-light ratio, $\Upsilon_\star^K = 0.5\ M_\odot/L_{\odot,K}$.

Star Formation Rate Surface Density (Appendix D): We combine FUV and 24μm maps to derive maps of $\Sigma_{\rm SFR}$; giving us a tracer sensitive to both exposed and dust-embedded star formation. The FUV data come from the GALEX Nearby Galaxies Survey (Gil de Paz et al. 2007) and the 24μm maps are part of SINGS. Because this precise combination of data is new, Appendix D includes an extended motivation for how we convert intensity to $\Sigma_{\rm SFR}$.

[8] IRAM is supported by CNRS/INSU (France), the MPG (Germany) and the IGN (Spain)

3.3. *Properties of the Sample*

Table 4 compiles the integrated properties of each galaxy in our sample. Columns (1) – (7) give basic parameters adopted from other sources: the name of the galaxy; the distance, inclination, and position angle (Walter et al. 2008, except that we adopt $i = 20°$ in M 51); and the morphology, B-band isophotal radius at 25 mag arcsec^{-2} (r_{25}), and B-band absolute magnitude from LEDA (Prugniel & Heraudeau 1998). Columns (8) and (9) give $v_{\rm flat}$ and $l_{\rm flat}$, the free parameters for our rotation curve fit (Appendix B); from these two parameters one can calculate $v\ (r_{\rm gal})$ and β. Columns (10) – (13) give the total stellar mass, H I mass, H_2 mass and SFR from integrating our data within 1.5 r_{25}.

Columns (14) – (17) give scale lengths derived from exponential fits to the Σ_*, $\Sigma_{\rm SFR}$, and $\Sigma_{\rm H2}$ (CO) radial profiles. The stellar scale lengths match those found by Tamburro et al. (2008) with 15% scatter; they are $\sim 10\%$ shorter than those found by Regan et al. (2001), with RMS scatter of 20%. Our CO scale lengths are taken from Leroy et al. (2008); these are $\sim 30\%$ shorter than those of Regan et al. (2001) on average.

3.4. *Methodology*

We work with maps of $\Sigma_{\rm HI}$, $\Sigma_{\rm H2}$ and $\Sigma_{\rm SFR}$ on the THINGS astrometric grid. All data are placed at a common spatial resolution, 400 pc for dwarf galaxies and 800 pc for spirals; when necessary, we use a Gaussian kernel to degrade our data to this resolution. The convolution occurs before any deprojection and may be thought of as placing each subsample at a single distance. Radial profiles of these maps and Σ_* appear in Appendix E.

Using these data, we compute each quantity in Table 1 for each pixel inside 1.2 r_{25} and derive radial profiles over the same range following the methodology in Appendix E. Because we measure Σ_* and $v(r_{\rm gal})$ only in radial profile, these maps are often a hybrid between radial profiles and pixel–by–pixel measurements.

In §4 – 6, we analyze the combined data set for the two subsamples and avoid discussing results for individual galaxies. We refer readers interested in individual galaxies to the Appendices. Appendix E gives our radial profile data and the atlas in Appendix F shows maps of $\Sigma_{\rm HI}$, $\Sigma_{\rm H2}$, total gas, unobscured $\Sigma_{\rm SFR}$, dust-embedded $\Sigma_{\rm SFR}$, and total $\Sigma_{\rm SFR}$, as well as profiles of the quantities in Table 1.

In keeping with our emphasis on the combined dataset, we default to quoting the mean and 1σ scatter when we give uncertainties in parameters derived from the ensemble of galaxies (we usually estimate the scatter using the median absolute deviation to reduce sensitivity to outliers). We prefer this approach to giving the uncertainty

TABLE 4
Properties of Sample Galaxies

Galaxy	Dist. (Mpc)	i (°)	PA (°)	Morph.	M_B (mag)	r_{25} (kpc)	$v_{\rm flat}$ (km s^{-1})	$l_{\rm flat}$ (kpc)	$\log M_*$ (M$_\odot$)	$\log M_{\rm HI}$ (M$_\odot$)	$\log M_{\rm H2}$ (M$_\odot$)	SFR (M$_\odot$ yr^{-1})	l_* (kpc)	$l_{\rm SFR}$ (kpc)	$l_{\rm CO}$ (kpc)
DDO 154	4.3	66	230	Irr	-14.4	1.2	50	2.0	7.1	8.7	$\lesssim$ 6.8	0.005	0.8	1.0	···
Ho I	3.8	12	50	Irr	-14.9	1.8	53	0.4	7.4	8.3	$\lesssim$ 7.2	0.009	0.8	1.2	···
Ho II	3.4	41	177	Irr	-16.9	3.7	36	0.6	8.3	8.9	$\lesssim$ 7.6	0.048	1.2	1.3	···
IC 2574	4.0	53	56	Irr	-18.0	7.5	134	12.9	8.7	9.3	$\lesssim$ 7.9	0.070	2.1	4.8	···
NGC 4214	2.9	44	65	Irr	-17.4	2.9	57	0.9	8.8	8.7	7.0	0.107	0.7	0.5	···
NGC 2976	3.6	65	335	Sc	-17.8	3.8	92	1.2	9.1	8.3	7.8	0.087	0.9	0.8	1.2
NGC 4449	4.2	60	230	Irr	-19.1	2.8	···	···	9.3	9.2	6.9[a]	0.371	0.9	0.8	···
NGC 3077	3.8	46	45	Sd	-17.7	3.0	···	···	9.3	9.1	6.5[a]	0.086	0.7	0.3	···
NGC 7793	3.9	50	290	Scd	-18.7	6.0	115	1.5	9.5	9.1	···	0.235	1.3	1.3	···
NGC 2403	3.2	63	124	SBc	-19.4	7.3	134	1.7	9.7	9.5	7.3	0.382	1.6	2.0	1.9
NGC 0925	9.2	66	287	SBcd	-20.0	14.2	136	6.5	9.9	9.8	8.4	0.561	4.1	4.1	···
NGC 0628	7.3	7	20	Sc	-20.0	10.4	217	0.8	10.1	9.7	9.0	0.807	2.3	2.4	2.4
NGC 3198	13.8	72	215	SBc	-20.7	13.0	150	2.8	10.1	10.1	8.8	0.931	3.2	3.4	2.7
NGC 3184	11.1	16	179	SBc	-19.9	11.9	210	2.8	10.3	9.6	9.2	0.901	2.4	2.8	2.9
NGC 4736	4.7	41	296	Sab	-20.0	5.3	156	0.2	10.3	8.7	8.6	0.481	1.1	0.9	0.8
NGC 3351	10.1	41	192	SBb	-19.7	10.6	196	0.7	10.4	9.2	9.0	0.940	2.2	1.8	2.5
NGC 6946	5.9	33	243	SBc	-20.9	9.8	186	1.4	10.5	9.8	9.6	3.239	2.5	2.7	1.9
NGC 3627	9.3	62	173	SBb	-20.8	13.9	192	1.2	10.6	9.0	9.1	2.217	2.8	1.9	2.2
NGC 5194	8.0	20	172	SBc	-21.1	9.0	219	0.8	10.6	9.5	9.4	3.125	2.8	2.4	2.3
NGC 3521	10.7	73	340	SBbc	-20.9	12.9	227	1.4	10.7	10.0	9.6	2.104	2.9	3.1	2.2
NGC 2841	14.1	74	153	Sb	-21.2	14.2	302	0.6	10.8	10.1	8.5	0.741	4.0	5.3	···
NGC 5055	10.1	59	102	Sbc	-20.6	17.4	192	0.7	10.8	10.1	9.7	2.123	3.2	3.1	3.1
NGC 7331	14.7	76	168	SAb	-21.7	19.6	244	1.3	10.9	10.1	9.7	2.987	3.3	4.5	3.1

[a]Unless noted $\log M_{\rm H2}$ comes from HERACLES Leroy et al. (2008) or BIMA SONG (Helfer et al. 2003). NGC 3077 is from Walter et al. (2001), NGC 4449 is from Bolatto et al. (2008). Upper limits are at 5σ significance.

in the mean because we are usually interested in how well a given number describes our whole sample, not how precisely we have measured the mean.

4. RESULTS

Here we present our main observational results, how the star formation efficiency varies as a function of other quantities. We begin in §4.1 by showing the SFE as a function of three basic parameters: galactocentric radius, stellar surface density, and gas surface density. Then in §4.2, we look at SFE as a function of the laws described in §2.1. Finally, in §4.3 we show the SFE as a function of the thresholds described in §2.2.

We present these results as a series of plots that each show SFE as a function of another quantity. These all follow the format seen in Figure 1, where we show SFE (y-axis) versus galactocentric radius (x-axis), normalized to the optical radius, r_{25}. We plot the subsamples of spiral (top row) and dwarf galaxies (bottom row) separately.

On the left, we show results for radial profiles. Each point shows the average SFE over one $10''$-wide tilted ring in one galaxy. The color indicates whether the ISM averaged over the ring is mostly (> 50%) H I (blue) or H_2 (magenta). Thick black crosses show all data binned into a single trend. For each bin, we plot the median, 50% range (y-error bar), and bin width (x-error bar, here 0.1 r_{25}).

On the right, we again show SFE as a function of radius, this time calculated for each line of sight. We coadd all galaxies, giving equal weight to each, and pick contours that contain 90% (green), 75% (yellow), 50% (red), and 25% (purple) of the resulting data. Most numerical results use the annuli, which are easier to work with; these pixel-by-pixel plots verify that conclusions based on rings hold pixel-by-pixel down to kiloparsec scales.

We do not analyze data with $\Sigma_{\rm gas} < 1$ M$_\odot$ pc^{-2} because the SFE is not well-determined for low gas surface densities; that is, we only address the question "where there is gas, is it good at forming stars?" Data with $\Sigma_{\rm SFR} < 10^{-4}$ M$_\odot$ yr^{-1} kpc^{-2} are treated as upper limits. These are red arrows in the radial profiles plots. In the pixel-by-pixel plots, hatched regions show the area inhabited by 95% of data with $\Sigma_{\rm SFR} \leq 10^{-4}$ M$_\odot$ yr^{-1} kpc^{-2}, i.e., the hatched regions indicate the area where we are incomplete. In the pixel–by–pixel plots, we include data out to r_{25}, while we plot radial profile data out to 1.2 r_{25}.

4.1. *SFE and Other Basic Quantities*

4.1.1. *SFE and Radius*

We argued in §1 that a critical observation for theories of galactic–scale star formation is that the SFE declines in the outer parts of spiral galaxies. Figure 1 shows this via plots of SFE against galactocentric radius (normalized to r_{25}) in our two subsamples.

In spiral galaxies (top row), the SFE is nearly constant where the ISM is mostly H_2 (magenta), which agrees with our observation of a linear relationship between $\Sigma_{\rm H2}$ and $\Sigma_{\rm SFR}$ in Bigiel et al. (2008). Typically, the ISM is equal parts H I and H_2 at $r_{\rm gal} = 0.43 \pm 0.18\ r_{25}$ (§5.2). Outside this transition, the SFE decreases steadily with increasing radius. This decline continues to $r_{\rm gal} \gtrsim r_{25}$, the limit of our data. This is similar, though not identical, to the observation by Kennicutt (1989) and Martin & Kennicutt (2001) that star formation is not widespread beyond a certain radius.

The SFE in spirals can be reasonably described in two ways. First, a constant SFE in the inner parts of galaxies followed by a break at 0.4 r_{25} (slightly inside the transition to a mostly-H I ISM):

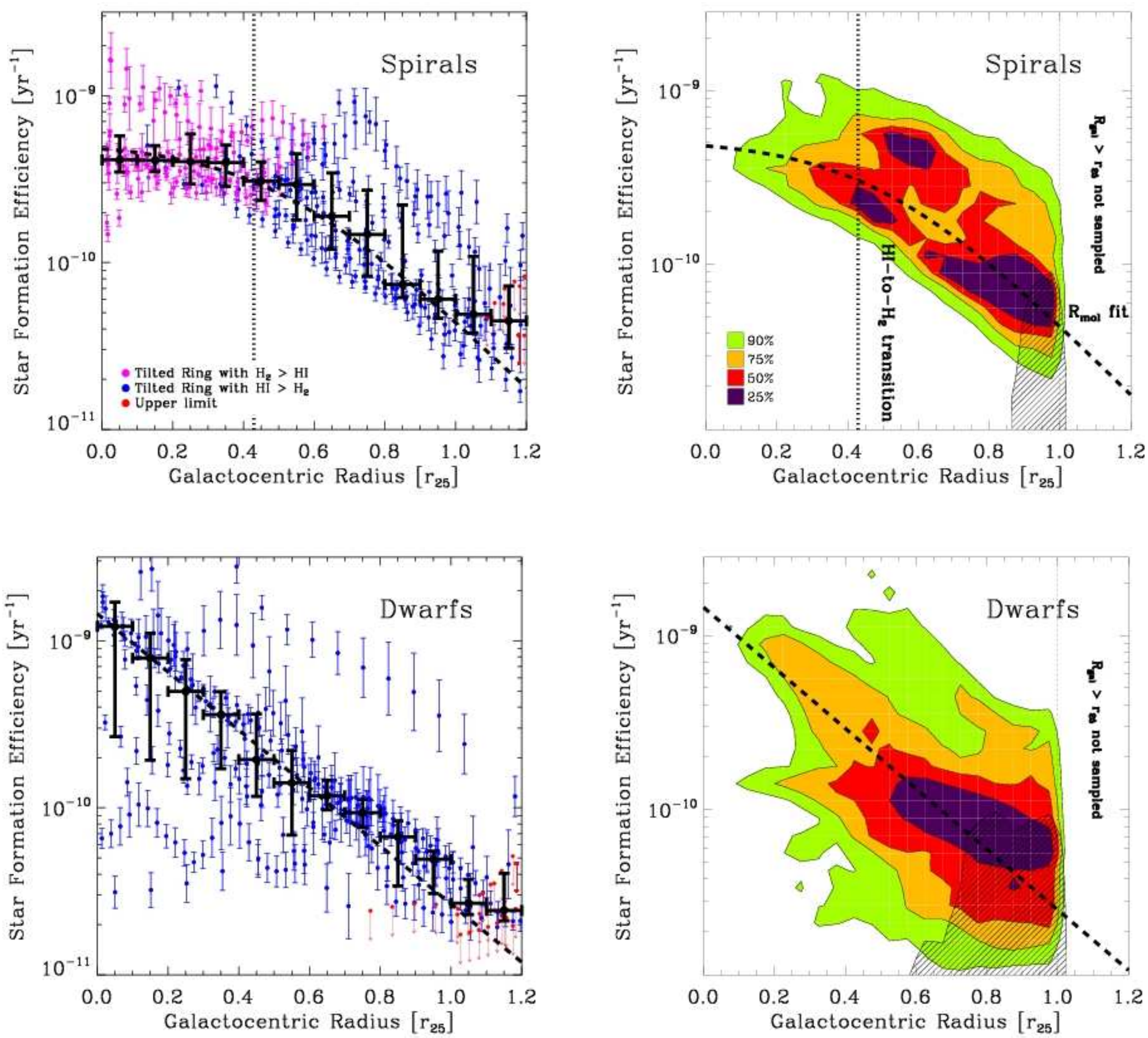

FIG. 1.— Star formation efficiency as a function of galactocentric radius in spiral (top row) and dwarf (bottom row) galaxies. The left panels show results for radial profiles; each point shows the average SFE over a 10″-wide tilted ring; magenta points are H_2-dominated ($\Sigma_{H2} > \Sigma_{HI}$), blue points are H I-dominated ($\Sigma_{H2} < \Sigma_{HI}$), and red arrows indicate upper limits. The right panels show data for individual lines of sight. We give each galaxy equal weight and choose contours that include 90%, 75%, 50%, and 25% of the data. The hatched regions indicate where we are incomplete. The top panels show a nearly fixed SFE in H_2-dominated galaxy centers (magenta). Where H I dominates the ISM (blue), we observe the SFE to decline exponentially with radius; the thick dashed lines show fits of SFE to $r_{\rm gal}$ (Equations 22 and 23). The vertical dotted line in the upper panels shows $r_{\rm gal}$ at the H I-to-H_2 transition in spirals, $0.43 \pm 0.18\ r_{25}$ (§5.2).

$$\mathrm{SFE} = \left\{ \begin{array}{cc} 4.3 \times 10^{-10} & r_{\rm gal} < 0.4 r_{25} \\ 2.2 \times 10^{-9}\ \exp\left(\frac{-r_{\rm gal}}{0.25\ r_{25}}\right) & r_{\rm gal} > 0.4 r_{25} \end{array} \right. \mathrm{yr}^{-1}\,. \tag{21}$$

Alternatively, we can adopt Equation 8, appropriate for a fixed SFE (H_2), and derive the best-fit exponential relating $R_{\rm mol}$ to $r_{\rm gal}$,

$$\mathrm{SFE} = 5.25 \times 10^{-10}\ \frac{R_{\rm mol}}{R_{\rm mol}+1}\ \mathrm{yr}^{-1} \tag{22}$$
$$R_{\rm mol} = 10.6\ \exp\left(-r_{\rm gal}/0.21\ r_{25}\right)\ ,$$

which appears as a thick dashed line in the upper panels of Figure 1. The two fits reproduce the observed SFE with similar accuracy; the scatter about each is ≈ 0.26 dex, slightly better than a factor of 2.

In dwarf galaxies (lower panels), we observe a steady decline in the SFE with increasing radius for all $r_{\rm gal}$, approximately described by

$$\mathrm{SFE} = 1.45 \times 10^{-9}\ \exp\left(-r_{\rm gal}/0.25\ r_{25}\right)\ \mathrm{yr}^{-1} \tag{23}$$

with ~ 0.4 dex scatter about the fit, i.e., a factor of 2–3.

In dwarfs, we take $\Sigma_{\rm gas} \approx \Sigma_{\rm HI}$, so that SFE= $\Sigma_{\rm SFR}/\Sigma_{\rm HI}$. For comparison with Equation 22, however, we rewrite Equation 23 *assuming* that SFE (H_2)= $5.25 \times 10^{-10}\ \mathrm{yr}^{-1}$, the value measured in spirals. In terms of $R_{\rm mol}$, Equation 23 becomes

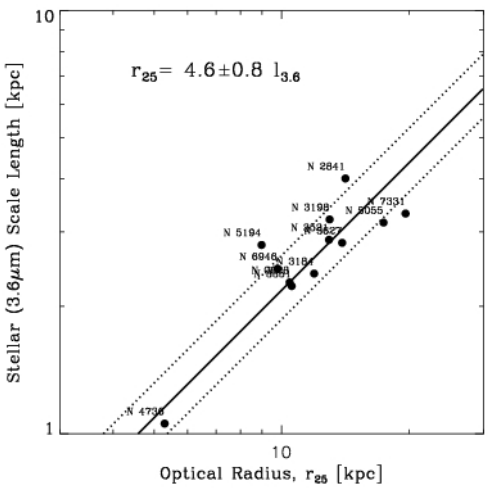

FIG. 2.— Stellar scale length, l_*, as a function of isophotal radius, r_{25}. Solid and dashed lines show $r_{25} = (4.6 \pm 0.8)\ l_*$.

$$\mathrm{SFE} = \frac{\Sigma_{\rm SFR}}{\Sigma_{\rm HI}} = 5.25 \times 10^{-10}\ R_{\rm mol}\ {\rm yr}^{-1} \qquad (24)$$
$$R_{\rm mol} = 2.76\ \exp\left(-r_{\rm gal}/0.25\ r_{25}\right)\ .$$

The outer parts of dwarfs, $r_{\rm gal} \gtrsim 0.4\ r_{25}$, appear similar to the outer disks of spiral galaxies in Figure 1. Surprisingly, however, we find the SFE to be *higher* in the central parts of dwarf galaxies than in the molecular gas of spirals. A higher SFE in dwarf galaxies is quite unexpected. Their lower metallicities, more intense radiation fields, and weaker potential wells should make gas *less* efficient at forming stars. A simple explanation for the high observed SFE is the presence of a significant amount of H_2. Figure 1 assumes that $\Sigma_{\rm gas} \approx \Sigma_{\rm HI}$ in dwarfs. If we miss a significant amount of H_2 along a line of sight, we will overestimate the SFE because we underestimate $\Sigma_{\rm gas}$. We quantify the possibility of substantial H_2 in dwarfs in §5.3, but the magnitude of the effect can be read directly from Equation 24. At $r_{\rm gal} = 0$, if dwarf galaxies have the same SFE (H_2) as spirals, $R_{\rm mol} \approx 2.76$, i.e., $\Sigma_{\rm H2} \approx 2.76\ \Sigma_{\rm HI}$.

4.1.2. *SFE and Stellar Surface Density*

Galactocentric radius is probably not intrinsically important to a local process like star formation, but Figure 1 suggests that local conditions covariant with radius have a large effect on the ability of gas to form stars. The radius, r_{25}, that we use to normalize the x-axis is defined by an optical isophote and thus measures stellar light. Therefore r_{25} is closely linked to the stellar distribution.

Figure 2 shows this link directly. We plot stellar scale length, l_*, measured via an exponential fit to the 3.6μm profile as a function of r_{25} for our spiral subsample. We see that $r_{25} = (4.6 \pm 0.8)\ l_*$ and that we could have equivalently normalized the x-axis in Figure 1 by l_*. We may suspect, then, that the stellar surface density, Σ_*, underlies the well-defined relation between SFE and $r_{\rm gal}$ observed in Figure 1.

In Figure 3, we explore this connection by plotting SFE as a function of Σ_*. In both spiral and dwarf galaxies, we see a nearly linear relationship between SFE and Σ_* where the ISM is H I-dominated (blue points).

A basic result of THINGS is that over the optical disk of most star forming galaxies, the H I surface density varies remarkably little (Appendices E and F and Walter et al. 2008). Inspecting our atlas, one sees that $\Sigma_{\rm HI} \approx 6\ {\rm M}_\odot\ {\rm pc}^{-2}$ (within a factor of 2) over a huge range of local conditions, including most of the optical disk in most galaxies. Because $\Sigma_{\rm gas}$ is nearly constant in the H I-dominated (blue) regime, SFE $\propto \Sigma_*$ approximately defines a line of fixed specific star formation rate (SSFR), i.e., star formation rate per unit stellar mass.

The inverse of the SSFR is the stellar assembly time, $\tau_* = \Sigma_*/\Sigma_{SFR}$. This is the time required for the present star formation rate to build up the observed stellar disk. In our spiral subsample, the mean $\log_{10} \tau_* \approx 10.5 \pm 0.3$, i.e., 3.2×10^{10} years or slightly more than 2 Hubble times. Dwarf galaxies have shorter assembly times, $\log_{10} \tau_* \approx 10.2 \pm 0.3$ years, about a Hubble time (dashed lines in Figure 3 show these values using average values of $\Sigma_{\rm gas}$ for each subsample). Taking these numbers at face value, dwarfs are forming stars at about their time-average rate, while spirals are presently forming stars at just under half of their average rate.

We *only* observe SFE $\propto \Sigma_*$ where the ISM is mostly H I. Where the ISM is mostly H_2 in spirals galaxies, we observe a constant SFE at a range of Σ_*; similar to the constancy as a function of $r_{\rm gal}$ observed in the inner parts of spirals (Figure 1). The transition between these two regimes occurs at $\Sigma_* = 81 \pm 25\ {\rm M}_\odot\ {\rm pc}^{-2}$ (§5.2) in spirals. In dwarfs, lines of sight with Σ_* above this transition value exhibit systematically high SFE, lending further, albeit indirect, support to the idea that these points correspond to unmeasured H_2.

Figures 1 and 3 show that where the ISM is mostly H_2, the star formation rate per unit *gas* (SFE) is nearly constant and that where the ISM is mostly H I, the star formation rate per unit *stellar mass* (SSFR) is nearly constant. Together these observations suggest that H_2, stars, and star formation have similar structure with all three embedded in a relatively flat distribution of H I. Figure 4 shows that the scale lengths of these three distributions are, in fact, comparable. The star formation rate (black) and CO (gray) scale lengths of spiral galaxies are both roughly equal to the stellar scale length:

$$l_{\rm CO} = (0.9 \pm 0.2)\ l_* \text{ and } l_{\rm SFR} = (1 \pm 0.2)\ l_*\ . \qquad (25)$$

Regan et al. (2001) also found that $l_{\rm CO} \approx l_*$ comparing K-band maps to BIMA SONG and Young et al. (1995) found $l_{\rm CO} \approx 0.2\ r_{25}$, which is almost identical to our $l_{\rm CO} \sim 0.9\ l_*$ and $(4.6 \pm 0.8)\ l_* = r_{25}$.

4.1.3. *SFE and Gas Surface Density*

This link between Σ_* and the SFE is somewhat surprising because it is common to view $\Sigma_{\rm SFR}$, and thus the SFE, as set largely by $\Sigma_{\rm gas}$ alone over much of the disk of a galaxy (following, e.g., Kennicutt 1998a). In Figure 5 we show this last slice through SFR-stars-gas parameter space, plotting SFE as a function of $\Sigma_{\rm gas}$.

As in Figures 1 and 3, we observe two distinct regimes. In spirals, where $\Sigma_{\rm gas} > 14 \pm 6\ {\rm M}_\odot\ {\rm pc}^{-2}$ (§5.2) the ISM is mostly H_2 and we observe a fixed SFE. This

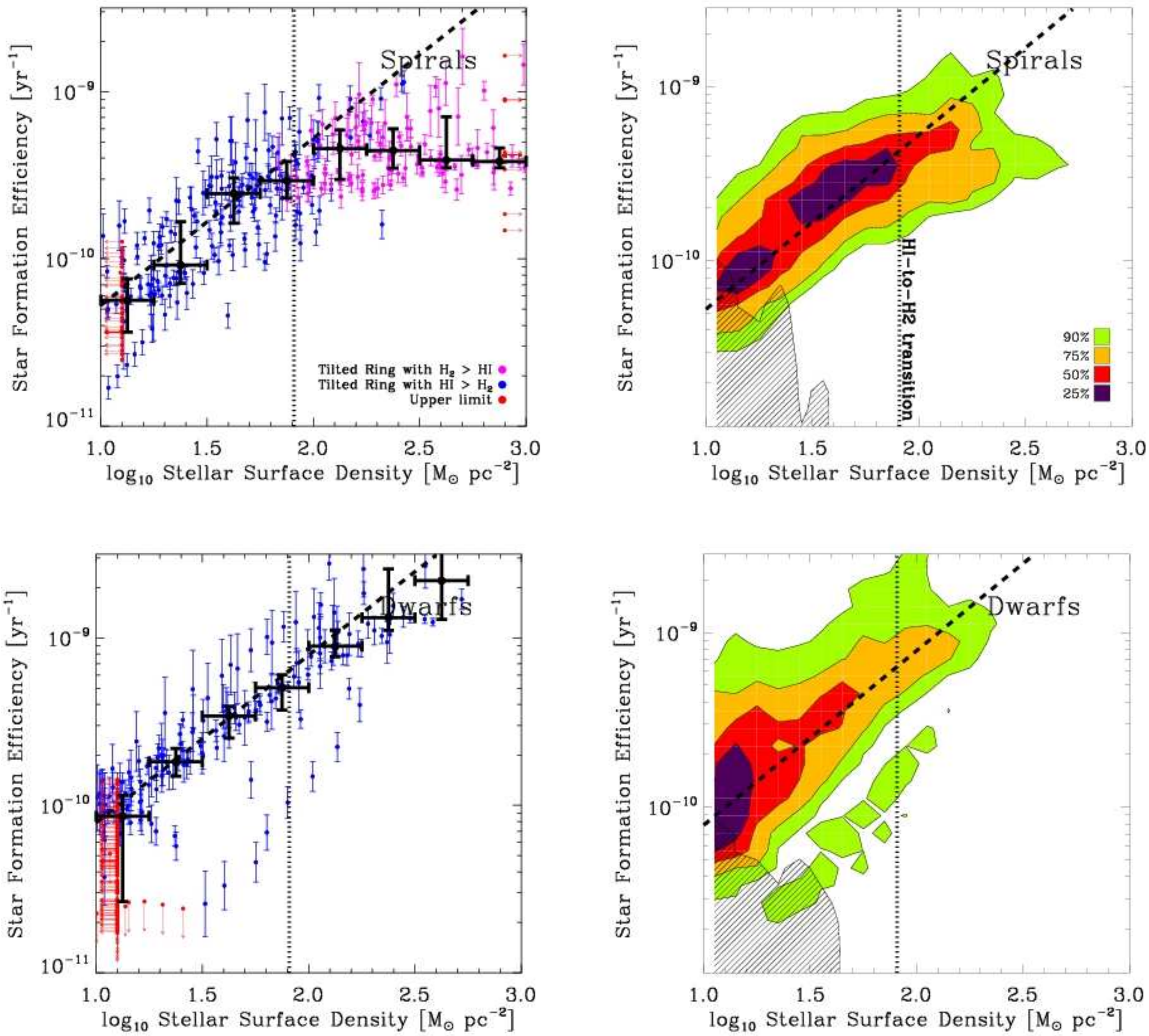

Fig. 3.— SFE as a function of stellar surface density, Σ_*, in spiral (top row) and dwarf (bottom row) galaxies. Conventions and symbols are as in Figure 1. Dashed diagonal lines show the linear relationship between SFE and Σ_* expected for the mean stellar assembly time and $\Sigma_{\rm gas}$ for each subsample. Vertical dotted lines show Σ_* where the ISM is equal parts H I and H_2 in spirals (§5.2), $\Sigma_* = 81 \pm 25$ M$_\odot$ pc^{-2}.

$\Sigma_{\rm gas}$, shown by a vertical dotted line, corresponds approximately to both $N(H) \sim 10^{21}$ cm^{-2} star formation threshold noted by Skillman (1987) and the saturation value for H I observed by, e.g., Martin & Kennicutt (2001) and Wong & Blitz (2002) (and seen strikingly in THINGS at $\Sigma_{\rm gas} = 12$ M$_\odot$ pc^{-2} by Bigiel et al. 2008, who quote $\Sigma_{\rm gas} = 9$ M$_\odot$ pc^{-2} but do not include helium).

In contrast to $r_{\rm gal}$ and Σ_*, $\Sigma_{\rm gas}$ does not exhibit a clear correlation with the SFE where the ISM is mostly H I. Instead, over the narrow range $\Sigma_{\rm gas} \approx 5$–$10$ M$_\odot$ pc^{-2}, the SFE varies from $\sim 3 \times 10^{-11}$ to 10^{-9} yr^{-1}. We see little evidence that $\Sigma_{\rm HI}$ plays a central role regulating the SFE in either spirals or dwarfs. Rather, the most striking observation in Figure 5 is that $\Sigma_{\rm HI}$ exhibits a narrow range of values over the optical disk and is therefore itself likely subject to some kind of regulation.

The possibility of a missed reservoir of molecular gas in dwarfs is again evident from the lower panels in Figure 5. A subset of data has SFE higher than that observed for H_2 in spirals and just to the left of the H I saturation value. If H_2 were added to these points, they would move down (as the SFE decreases) and to the right (as $\Sigma_{\rm gas}$ increases), potentially yielding a data distribution similar to that we observe in spirals.

4.2. *SFE and Star Formation Laws*

We now ask whether the star formation laws proposed in §2.1 can explain the radial decline in SFE and whether SFE (H_2), already observed to be constant as a function of $r_{\rm gal}$, Σ_*, and $\Sigma_{\rm gas}$ (but with some scatter), exhibits *any* kind of systematic behavior. We compare the SFE to four quantities that drive the predictions in Table 1: gas surface density (already seen in Figure 5), gas pressure (density), the orbital timescale, and the derivative of the rotation curve, β.

4.2.1. *Free–Fall Time in a Fixed Scale Height Disk*

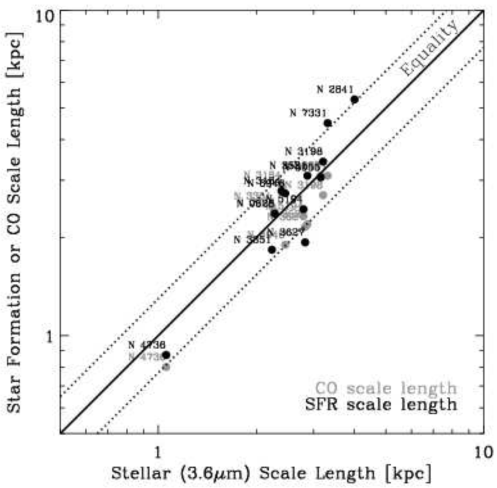

FIG. 4.— The scale lengths of star formation (black) and CO (gray) as a function of the stellar scale length (x-axis). All three scale lengths are similar, the dashed lines show slope unity and $\pm 30\%$ (the approximate scatter in the data).

A dashed line in Figure 5 illustrates SFE $\propto \Sigma_{\rm gas}^{0.5}$, expected if the SFE is proportional to the free-fall time in a fixed scale height gas disk (similar to the Kennicutt–Schmidt law, Kennicutt 1998a). The normalization matches the H_2–dominated parts of spirals and roughly bisects the range of SFE observed for dwarfs, but large areas of the disk have much lower SFE than one would predict from this relation. Adjusting the normalization can move the line up or down but cannot reproduce the distribution of data observed in Figure 5.

The culprit here is the small dynamic range in $\Sigma_{\rm HI}$. Because $\Sigma_{\rm HI}$ does not vary much across the disk, while the SFE does, the free–fall time in a fixed scale height disk, or any other weak dependence of SFE on $\Sigma_{\rm gas}$ alone, cannot reproduce variations in the SFE where the ISM is mostly H I. A quantity other than $\Sigma_{\rm gas}$ must play an important role at radii as low as $\sim 0.5\ r_{25}$ (a fact already recognized by Kennicutt 1989, among others).

4.2.2. *Free–Fall Time in a Variable Scale Height Gas Disk; Pressure and ISM Phase*

We saw in §4.1 that where the ISM is mostly H I, the SFE correlates better with Σ_* than with $\Sigma_{\rm gas}$. This might be expected if the stellar potential well plays a central role in setting the *volume* density of the gas, $\rho_{\rm gas}$, because Σ_* varies much more strongly with radius than $\Sigma_{\rm HI}$. In §2 we present two predictions relating SFE to $\rho_{\rm gas}$: that the timescale over which GMCs form depends on the $\tau_{\rm ff}$, the free–fall time in a gas disk with a scale height set by hydrostatic equilibrium[9], and that the ratio $R_{\rm mol} = \Sigma_{\rm H2}/\Sigma_{\rm HI}$ depends primarily on midplane gas pressure, $P_{\rm h}$.

Under our assumption of a fixed $\sigma_{\rm gas}$, $P_{\rm h} \propto \rho_{\rm gas}$ and both predictions can be written as a power law relating SFE or $R_{\rm mol}$ to $P_{\rm h}$. In Figure 6 we plot SFE as a function of $\rho_{\rm gas}$ and $P_{\rm h}$ (top and bottom x-axis), estimated from hydrostatic equilibrium (Equation 9).

[9] Hereafter $\tau_{\rm ff}$ refers only to the free fall time in a gas disk with a scale height set by hydrostatic equilibrium.

Where the ISM is mostly H_2 (magenta points) in spirals (top row), we observe no clear relationship between $P_{\rm h}$ and SFE, further evidence that SFE (H_2) is largely decoupled from global conditions of the ISM in our data.

Where the ISM is mostly H I (blue points) in dwarf galaxies and the outer parts of spirals, the SFE correlates with $P_{\rm h}$. $P_{\rm h}$ predicts the SFE notably better than $\Sigma_{\rm gas}$ in this regime, supporting the idea that the volume density of gas (at least H I) is more relevant to star formation than surface density. Wong & Blitz (2002) and Blitz & Rosolowsky (2006) observed a continuous relationship between $R_{\rm mol}$ and $P_{\rm h}$, mostly where $\Sigma_{\rm H2} \gtrsim \Sigma_{\rm HI}$. Figure 6 suggests that such a relationship extends well into the regime where H I dominates the ISM.

The solid line in Figure 6 illustrates the case of 1% of the gas formed into stars per $\tau_{\rm ff}$ (SFE $\propto \rho_{\rm gas}^{0.5}$), a typical value at the H I–to–H_2 transition in spirals (§5.2). Adjusting the normalization slightly, such a line can intersect both the high and low end of the observed SFE in spirals, but predicts variations in SFE (H_2) that we do not observe and is too shallow to describe dwarf galaxies.

The dash–dotted line shows $R_{\rm mol} \propto \tau_{\rm ff}^{-1} \propto P_{\rm h}^{0.5}$, expected for GMC formation over a free fall time. In dwarf galaxies, where we take $\Sigma_{\rm gas} = \Sigma_{\rm HI}$, this is equivalent too SFE$\propto \tau_{\rm ff}^{-1}$. This description can describe spirals at high and intermediate $P_{\rm h}$, but is too shallow to capture the drop in SFE at large radii in spirals and across dwarf galaxies. If $\tau_{\rm ff}$ is the characteristic timescale for GMC formation, effects other than just an increasing timescale must suppress cloud formation in these regimes.

A dashed line shows the steeper dependence, $R_{\rm mol} \propto P_{\rm h}^{1.2}$, expected for low $R_{\rm mol}$ based on modeling by Elmegreen (1993). This may be a reasonable description of both spiral and dwarf galaxies (note that at high SFE, $P_{\rm h}$ may be underestimated in dwarf galaxies because we fail to account for H_2). We explore how $P_{\rm h}$ relates to $R_{\rm mol}$ more in §5.

4.2.3. *Orbital Timescale*

The orbital timescale, $\tau_{\rm orb}$, varies strongly with radius and Kennicutt (1998a) found $\tau_{\rm orb}$ to be a good predictor of disk–averaged SFE. In Figure 7, we plot SFE as a function of $\tau_{\rm orb}$ in our sample.

The solid line shows 6% of the gas converted to stars per $\tau_{\rm orb}$ and is a reasonable match to spirals near the H I–to–H_2 transition (vertical dotted line). This value agrees with the range of efficiencies found by Wong & Blitz (2002) and with Kennicutt (1998a), who found $\approx$ 7% of gas converted to stars per $\tau_{\rm orb}$ averaged over galaxy disks (converted to our adopted IMF). Like Wong & Blitz (2002), we do not observe a clear correlation between SFE and $\tau_{\rm orb}$ where the ISM is mostly H_2.

Where the ISM is mostly H I (blue points), the SFE clearly anti-correlates with $\tau_{\rm orb}$ in both spiral and dwarf galaxies. However, we do not observe a constant efficiency per $\tau_{\rm orb}$. In both subsamples, SFE drops faster than $\tau_{\rm orb}$ increases, so that data at large radii (longer $\tau_{\rm orb}$, lower SFE) show lower efficiency per $\tau_{\rm orb}$ than those from inner galaxies. Although $\tau_{\rm orb}$ correlates with the SFE, the drop in $\tau_{\rm orb}$ is not enough on its own to explain the drop in SFE.

We reach the same conclusion if we posit that $\tau_{\rm orb}$ is the relevant timescale for GMC formation, so that

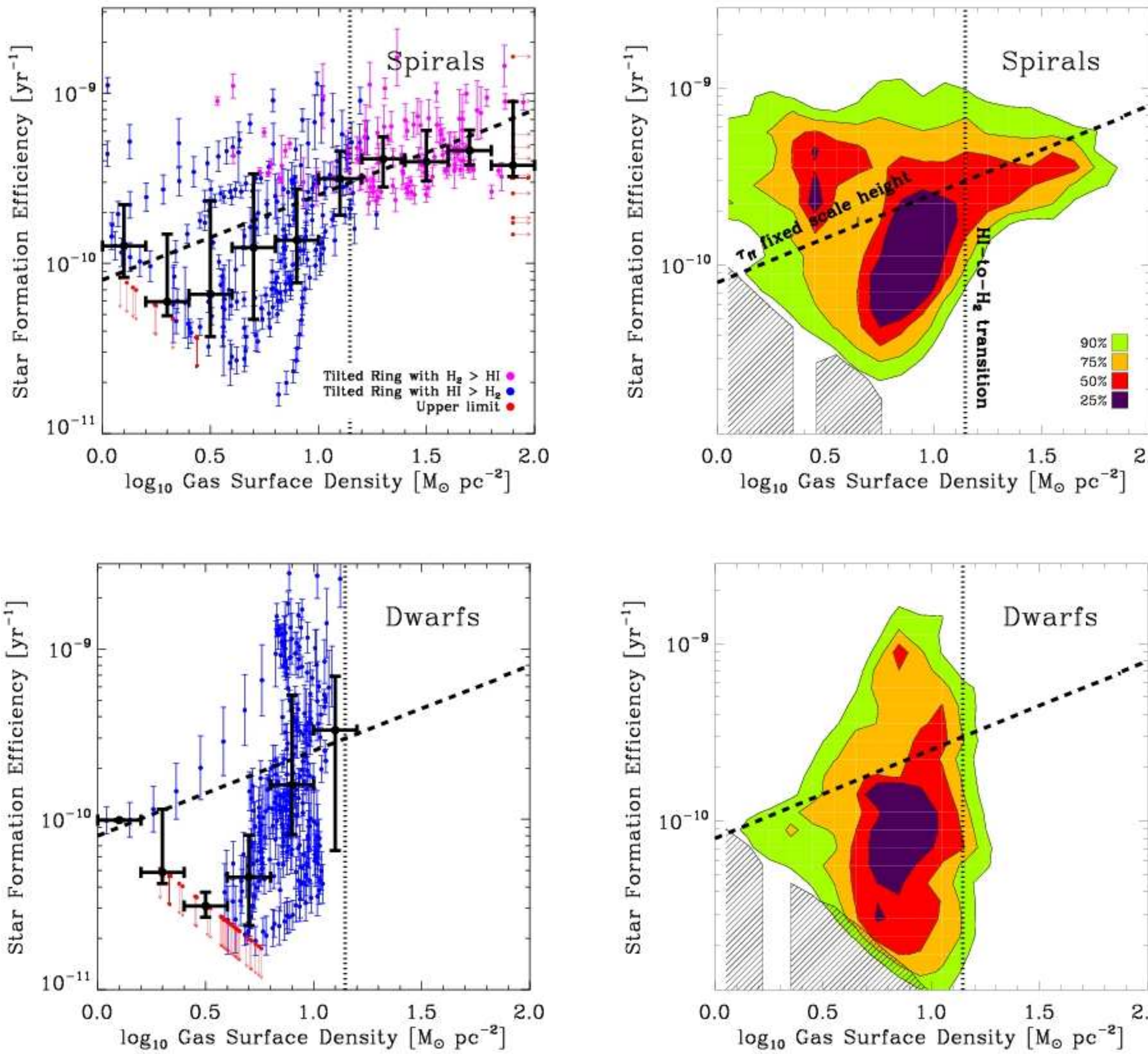

FIG. 5.— SFE as a function of $\Sigma_{\rm gas}$ in spiral (top row) and dwarf (bottom row) galaxies. Conventions and symbols are the same as in Figure 1. The vertical dotted line shows $\Sigma_{\rm gas}$ at the H I-to-H_2 transition in spirals (§5.2), $\Sigma_{\rm gas} = 14 \pm 6$ M$_\odot$ pc^{-2}. The dashed line shows the SFE proportional to the free–fall time in a fixed scale height disk. Clearly the line cannot describe both high and low SFE data, even if the normalization is adjusted, and so changes in this timescale cannot drive the radial decline that we observe in the SFE.

$R_{\rm mol} \propto \tau_{\rm orb}^{-1}$. The dashed lines in Figure 7 show this relation combined with a fixed SFE (H_2) and normalized to $R_{\rm mol} = 1$ at $\tau_{\rm orb} = (1.8 \pm 0.4) \times 10^8$ years, which we observe at the H I–to–H_2 transition in spirals (§5.2). This dependence is even shallower than SFE $\propto \tau_{\rm orb}^{-1}$ and cannot reproduce the SFE in both inner and outer disks by itself. If $\tau_{\rm orb}$ is the relevant timescale for cloud formation, then the fraction of gas that is actively forming stars must vary substantially between the middle and the edge of the optical disk.

4.2.4. *Derivative of the Rotation Curve, β*

Tan (2000) suggests that cloud-cloud collisions regulate the SFE. The characteristic timescale for such collisions is $\tau_{\rm orb}$ modified by the effects of galactic shear. We saw in Figure 7 that the SFE of molecular gas is not a strong function of $\tau_{\rm orb}$. Therefore, in Figure 8, we plot the SFE as a function of β, the logarithmic derivative of the rotation curve (we plot SFE against $Q_{\rm gas}$, the other component of this timescale in §4.3.1). This isolates the effect of differential rotation; $\beta = 0$ for a flat rotation curve and $\beta = 1$ for solid body rotation (no shear).

Figure 8 shows a simple relationship between β and SFE in spirals: $\beta > 0$ is associated with high SFE. High β occurs almost exclusively at low radius (where the rotation curve rises steeply) and in these regions the ISM is mostly H_2 with accordingly high SFE. On the other hand, the outer disks of spirals have $\beta \sim 0$ and a wide range of SFE. Beyond basic relationship, it is unclear that β has utility predicting the SFE. In particular, we see no clear relationship between SFE and β where the ISM is mostly H_2 (magenta points). If collisions between bound clouds regulate the SFE, we would expect an anti-correlation between β and SFE because cloud collisions are more frequent in the presence of greater shear.

In dwarf galaxies increasing β corresponds mostly to

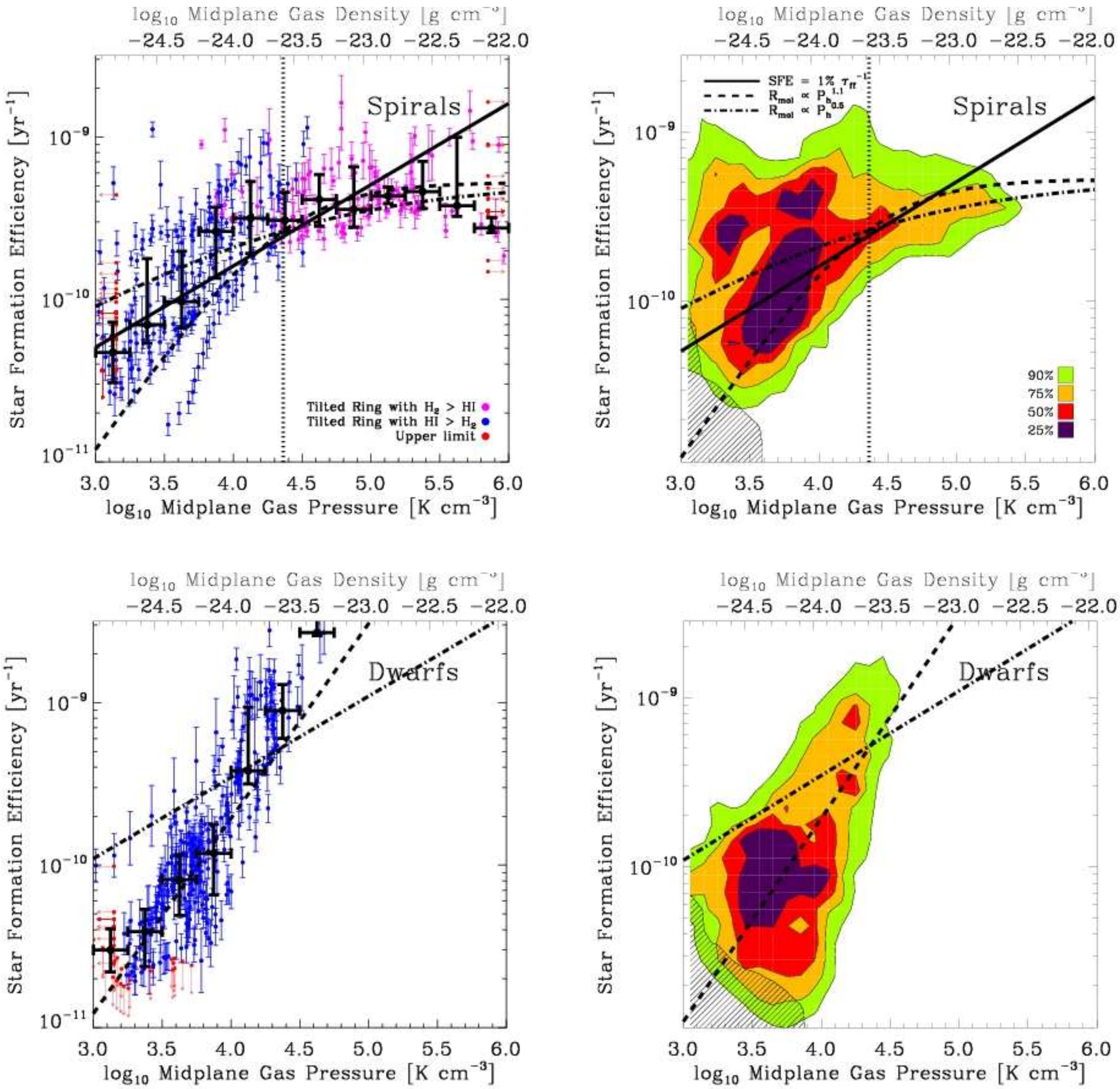

FIG. 6.— SFE as a function of midplane hydrostatic gas pressure, $P_{\rm h}$ (bottom x-axis) and equivalent volume density (top x-axis) in spiral (top row) and dwarf (bottom row) galaxies. Conventions follow Figure 1. The vertical line shows $P_{\rm h}$ at the H I-to-H_2 transition in spirals, $\log_{10} P_{\rm h}/k_{\rm B}$ [K cm^{-3}] ≈ 4.36. The solid line illustrates 1% of gas converted to stars per disk free–fall time. Dash-dotted and dashed lines show $R_{\rm mol} \propto P_{\rm h}^{0.5}$ ($\tau_{\rm ff}^{-1}$) and $R_{\rm mol} \propto P_{\rm h}^{1.2}$ (Elmegreen 1993). For our adopted $\sigma_{\rm gas} = 11$ km s^{-1} and including helium: $\rho\,[\mathrm{g\ cm^{-3}}] = 1.14 \times 10^{-28}\ (P_{\rm h}/k_{\rm B})\,[\mathrm{K\ cm^{-3}}]$ and $n\,[\mathrm{cm^{-3}}] = 4.4 \times 10^{23}\ \rho\,[\mathrm{g\ cm^{-3}}]$.

increasing SFE. This relationship has the sense of the shear threshold proposed by Hunter et al. (1998a), that where rotation curves are nearly solid body low shear allows clouds to form via instabilities aided by magnetic fields (see also Kim & Ostriker 2001). The rotation curves in dwarf galaxies rise more slowly than those in spirals, leading to $\beta > 0$ over a larger range of radii in dwarf galaxies and limiting $\beta = 0$ to the relative outskirts of the galaxy. A positive correlation between β and SFE is opposite the sense expected if cloud collisions are important: at high β collisions should be less frequent.

4.3. *SFE and Thresholds*

The decline in the SFE where the ISM is mostly H I is too dramatic to be reproduced across our whole sample by changes in $\tau_{\rm orb}$ or $\tau_{\rm ff}$ alone. This may be because at large radii a significant amount of gas is simply unrelated to star formation. If the fraction of gas that is unable to form GMCs increases with radius, the SFE will decline independent of any change in GMC formation time. Here we consider the SFE as a function of proposed star formation thresholds: gravitational instability in the gas alone ($Q_{\rm gas}$), in a disk of gas and stars ($Q_{\rm stars+gas}$), the ability of instabilities to develop before shear destroys them, and the ability of a cold gas phase to form.

First we plot each threshold as a function of galactocentric radius in spiral (Figure 9) and dwarf galaxies (Figure 10). Individual points correspond to aver-

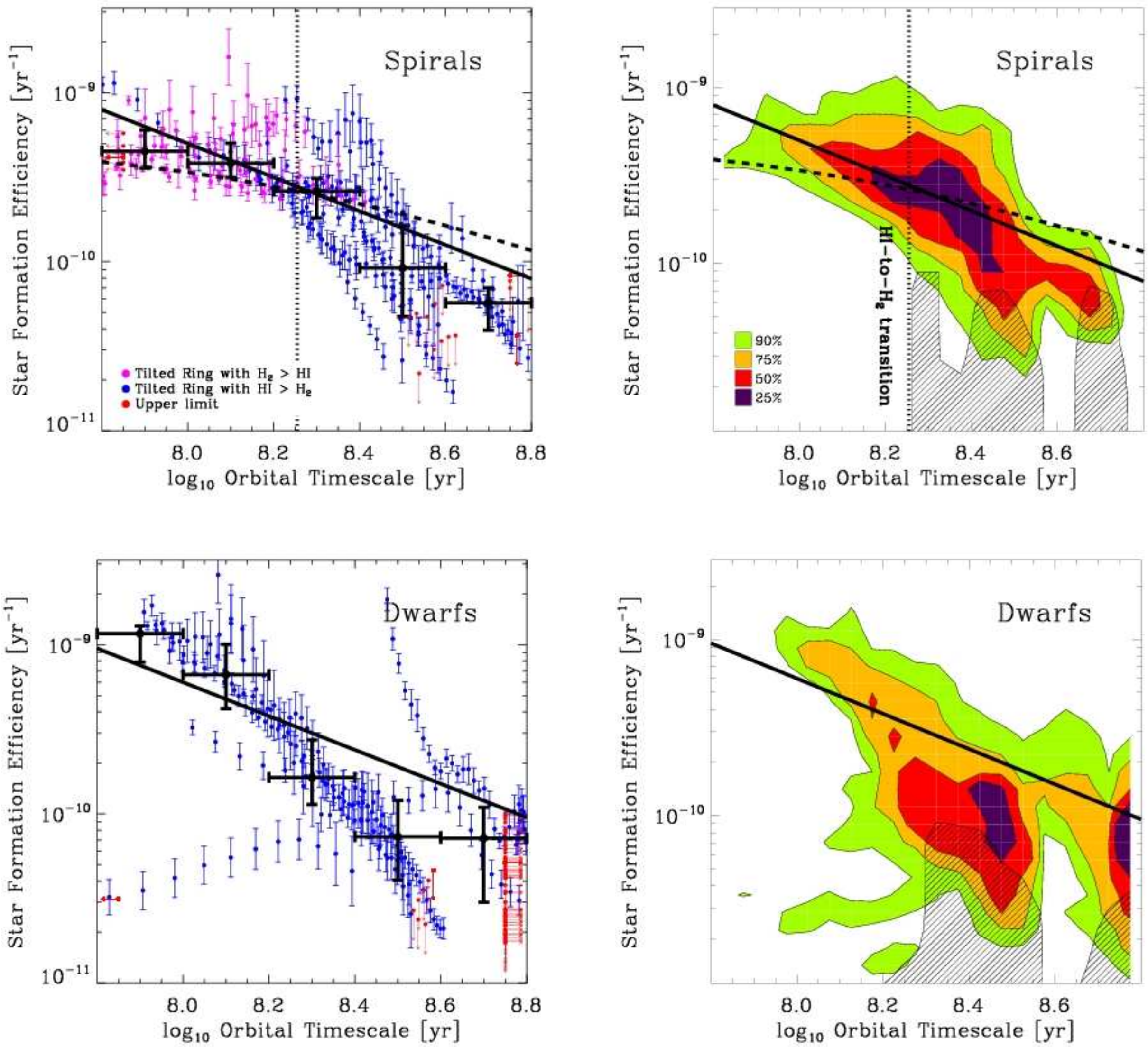

FIG. 7.— SFE as a function of the orbital timescale, $\tau_{\rm orb}$, in spiral (top row) and dwarf (bottom row) galaxies, following the conventions from Figure 1. The solid line shows 6% of gas converted into stars per $\tau_{\rm orb}$. The dashed line shows the expected SFE if $R_{\rm mol} = \Sigma_{\rm H2}/\Sigma_{\rm HI} \propto \tau_{\rm orb}^{-1}$. The SFE is a well-defined function of $\tau_{\rm orb}$, but the decline in $\tau_{\rm orb}$ alone cannot reproduce the radial decline in SFE or $R_{\rm mol}$.

ages over 10″–wide tilted rings. For magenta points $\Sigma_{\rm H2} > \Sigma_{\rm HI}$ and for blue points $\Sigma_{\rm H2} < \Sigma_{\rm HI}$. The gray region in each plot shows the nominal condition for instability, i.e., where we expect star formation to occur. Red arrows indicate data outside the range of the plot.

We proceed creating plots like Figure 1 for each threshold and comparing them to Figure 9. We expect supercritical gas to exhibit a (dramatically) higher SFE than subcritical gas, where star formation proceeds only in isolated pockets or not at all.

4.3.1. *Gravitational Instability in the Gas Disk*

Figure 11 shows SFE as a function of $Q_{\rm gas}$, Toomre's Q parameter for a thin gas disk; the top left panels in Figures 9 and 10 show $Q_{\rm gas}$ as a function of radius.

In each plot, a gray area indicates the theoretical condition for instability. We see immediately that almost no area in our sample is formally unstable. Rather, most lines of sight are strikingly stable, $Q_{\rm gas} \sim 4$ is typical inside $\sim 0.8\ r_{25}$ and $Q_{\rm gas} > 10$ is common.

We find no clear evidence for a $Q_{\rm gas}$ threshold (at any value) that can unambiguously distinguish regions with high SFE from those with low SFE. In spirals, $Q_{\rm gas} \lesssim 2.5$ appears to be a sufficient, but by no means necessary condition for high SFE; there are also areas where the ISM is mostly H_2, SFE is quite high and $Q_{\rm gas} \gtrsim 10$. In dwarfs $Q_{\rm gas}$ appears, if anything, anti-correlated with SFE, though this may partially result from incomplete estimates of $\Sigma_{\rm gas}$.

These conclusions appear to contradict the findings by Kennicutt (1989) and Martin & Kennicutt (2001), who found marginally stable gas ($Q_{\rm gas} \sim 1.5$) across the optical disk with a rise in $Q_{\rm gas}$ corresponding to dropping SFE at large radii. In fact, after correcting for different assumptions, our median $Q_{\rm gas}$ matches theirs quite well. Both Kennicutt (1989) and Martin & Kennicutt (2001) assumed $X_{\rm CO} = 2.8 \times 10^{20}$ cm^{-2} (K km s^{-1})$^{-1}$ and $\sigma_{\rm gas} = 6$ km s^{-1}, while we take $X_{\rm CO} = 2.0 \times$

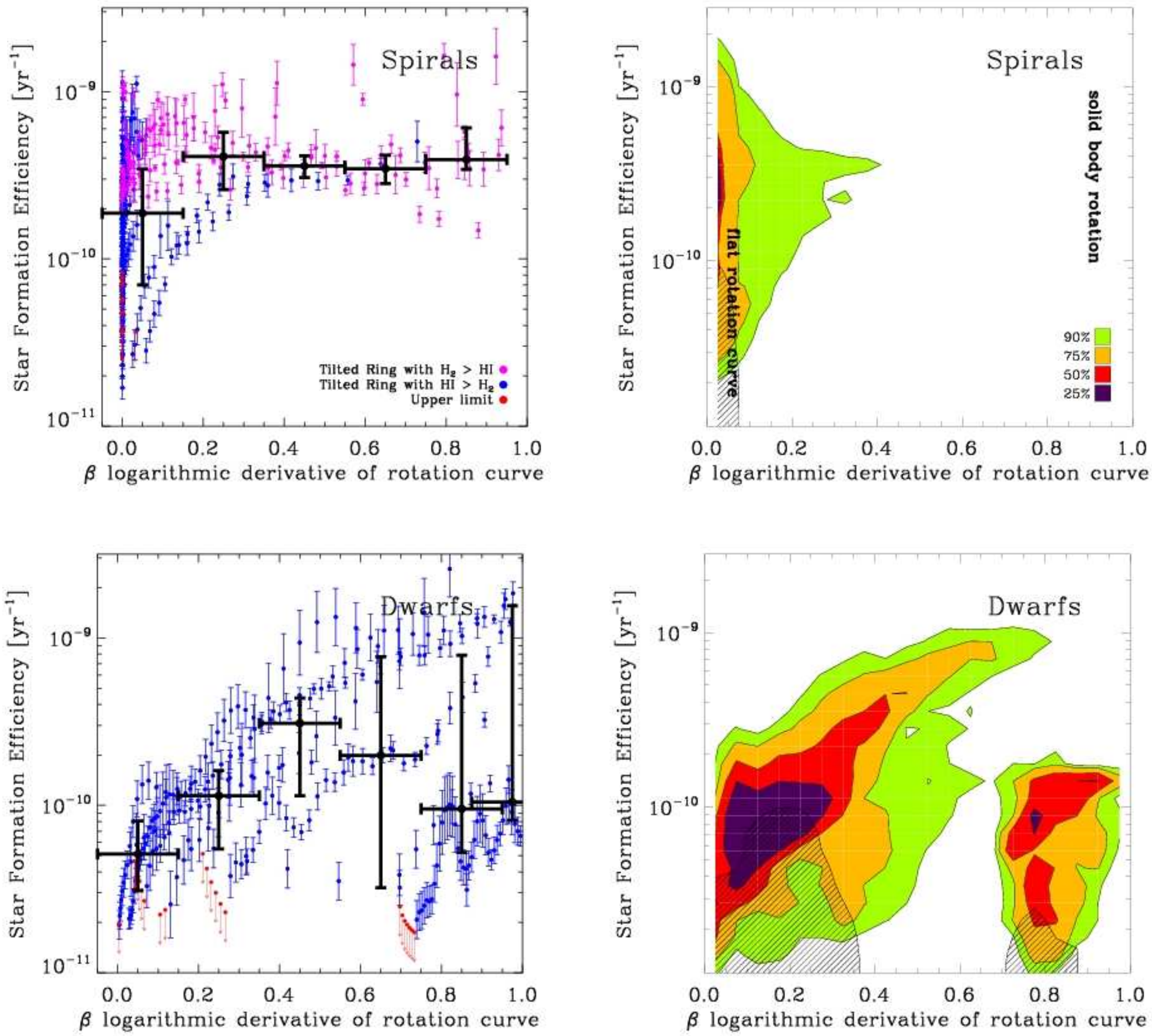

FIG. 8.— SFE as a function of β, the logarithmic derivative of the rotation curve in spiral (top row) and dwarf (bottom row) galaxies. $\beta = 1$ for solid body rotation and $\beta = 0$ for a flat rotation curve. If collisions between GMCs were important to triggering star formation, we would expect the SFE in the H_2 dominated (magenta) parts of spirals to be higher for low β (high shear), which is not apparent from the data.

10^{20} cm^{-2} (K km s^{-1})$^{-1}$ and $\sigma_{\rm gas} = 11$ km s^{-1}. As a result, we estimate less H_2 and more kinetic support than they do for the same observations. If we match their assumptions, our median $Q_{\rm gas}$ in spirals and the outer parts of dwarfs agrees quite well with their threshold value, though we find the central regions of dwarfs systematically above this value (as did Hunter et al. 1998a). We show this in Figures 9, 10, and 11 by plotting the Martin & Kennicutt threshold converted to our assumptions ($Q_{\rm gas} \sim 3.9$) as a a dashed line.

The main observational difference between our result and Martin & Kennicutt (2001) is that $Q_{\rm gas}$ shows much more scatter in our analysis. As a result, a systematic transition from low to high $Q_{\rm gas}$ near the edge of the optical disk is not a universal feature of our data, though a subset of spiral galaxies do show increasing $Q_{\rm gas}$ at large radii (Figure 9).

This discrepancy in $Q_{\rm gas}$ derived from similar data highlights the importance of assumptions. The largest effect comes from $\sigma_{\rm gas}$, which we measure to be $\approx$ 11 km s^{-1} and roughly constant in H I–dominated outer disks (Appendix B). We assume $\sigma_{\rm gas}$ to be constant everywhere, an assumption that may break down on small scales and in the molecular ISM. In this case we expect $\sigma_{\rm gas}$ to be locally lower than the average value, lowering $Q_{\rm gas}$ and making gas less stable. Black dots in the upper right panel of Figure 11 show the effect of changing $\sigma_{\rm gas}$ from 11 km s^{-1} (our value) to 6 km s^{-1} (the Martin & Kennicutt value) and then to 3 km s^{-1}, the value expected and observed for a cold H I component (e.g. Young et al. 2003; Schaye 2004; de Blok & Walter 2006). If most gas is cold then $Q_{\rm gas}$ may easily be $\lesssim 1$ for this component (if only a small fraction of gas is cold, the situation is less clear).

4.3.2. *Gravitational Instability Including Stars*

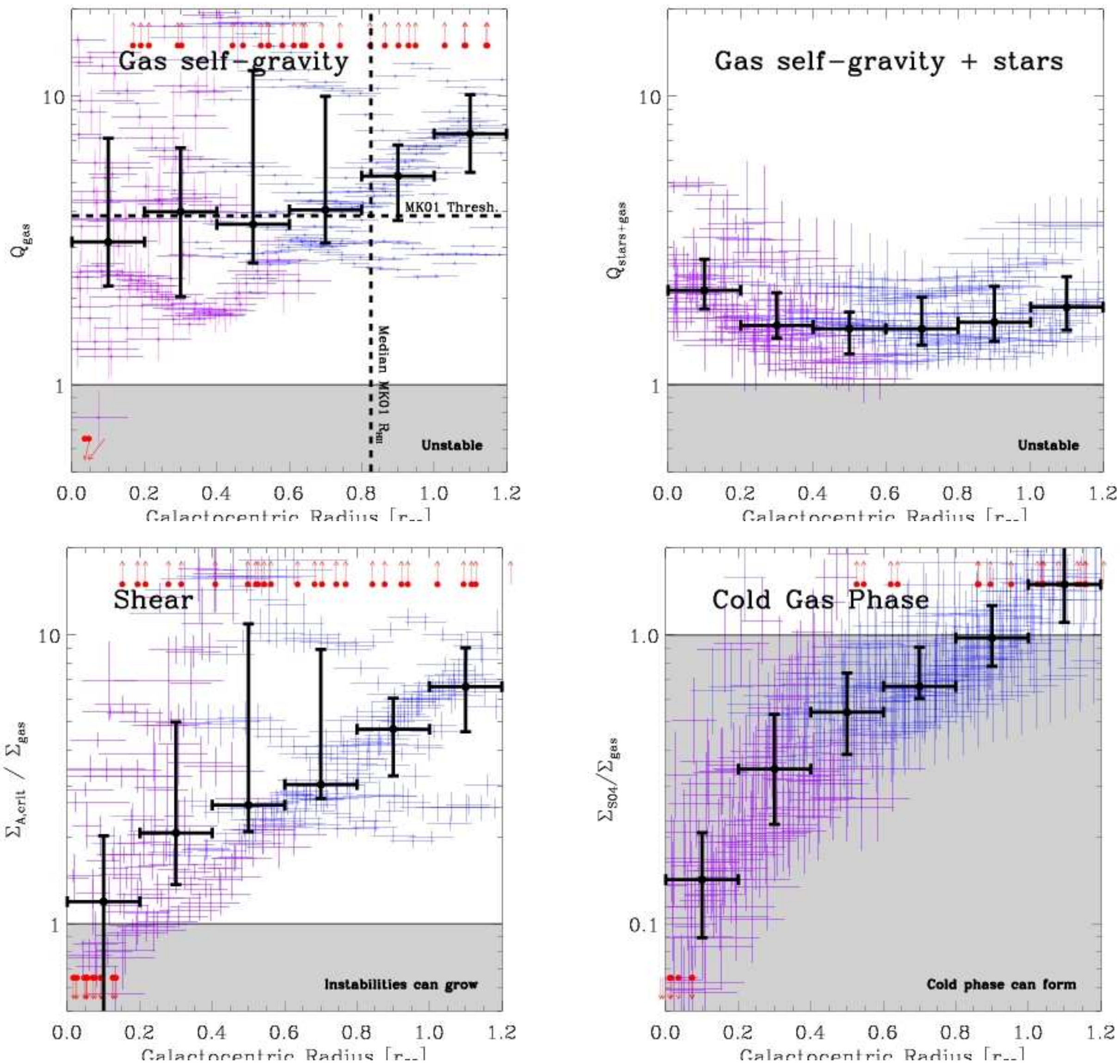

FIG. 9.— Radial behavior of thresholds in spiral galaxies: (*top left*) gravitational instability due to gas self gravity; (*top right*) gravitational instability due to the combination of self–gravity and stellar gravity; (*bottom left*) competition between cloud formation and destruction by shear; (*bottom right*) formation of a cold phase. Each point shows average $\Sigma_{\rm crit}/\Sigma_{\rm gas}$ over one $10''$ tilted ring in one galaxy. In magenta rings, the ISM is mostly H_2, in blue rings the ISM is mostly H I. Gray regions show the condition required for star formation.

Stars dominate the baryon mass budget over most of the areas we study and stellar gravity may be expected to affect the stability of the gas disk. In §2 we described a straightforward extension of $Q_{\rm gas}$ to the case of a disk containing gas and stars (Rafikov 2001). In Figure 12 we plot SFE as a function of this parameter, $Q_{\rm stars+gas}$, which we plot as a function of radius in the top right panels of Figures 9 and 10.

The gray region indicates where gas is unstable to axisymmetric collapse. Including stars does not render large areas of our sample unstable, but it does imply that most regions are only marginally stable, $Q_{\rm stars+gas} \sim 1.6$. This in turn suggests that it is not so daunting to induce collapse as one would infer from only $Q_{\rm gas}$.

In addition to lower values, $Q_{\rm stars+gas}$ exhibits a much narrower range of values than $Q_{\rm gas}$, mostly areas in both spiral and dwarf galaxies show $Q_{\rm stars+gas} = 1.3 - 2.5$. This may offer support to the idea of self–regulated star formation, but it also means that $Q_{\rm stars+gas}$ offers little leverage to predict the SFE. High SFE, mostly molecular regions show the same $Q_{\rm stars+gas}$ as low SFE regions from outer disks (indeed, the highest values we observe come from the central parts of spiral galaxies).

As with $Q_{\rm gas}$, our assumptions have a large impact on $Q_{\rm stars+gas}$. In addition to $\sigma_{\rm gas}$ and $X_{\rm CO}$(which affect the calculation via $Q_{\rm gas}$), the stellar velocity dispersion, σ_*, and mass–to–light ratio, $\Upsilon_\star^K$, strongly affect our stability estimate. We assume that $\sigma_* \propto \Sigma_*^{0.5}$ in order to yield a constant stellar scale height. If we instead fixed σ_*, we would derive $Q_{\rm stars+gas}$ increasing steadily with radius. Radial variations in $\Upsilon_\star^K$ may create a similar effect.

Boissier et al. (2003) find similar results to our own when they incorporate stars in their stability analysis; they adopt a lower $\sigma_{\rm gas}$ than we do, but also lower $X_{\rm CO}$ and the effects roughly offset. Yang et al. (2007) recently derived $Q_{\rm stars+gas}$ across the LMC and found widespread

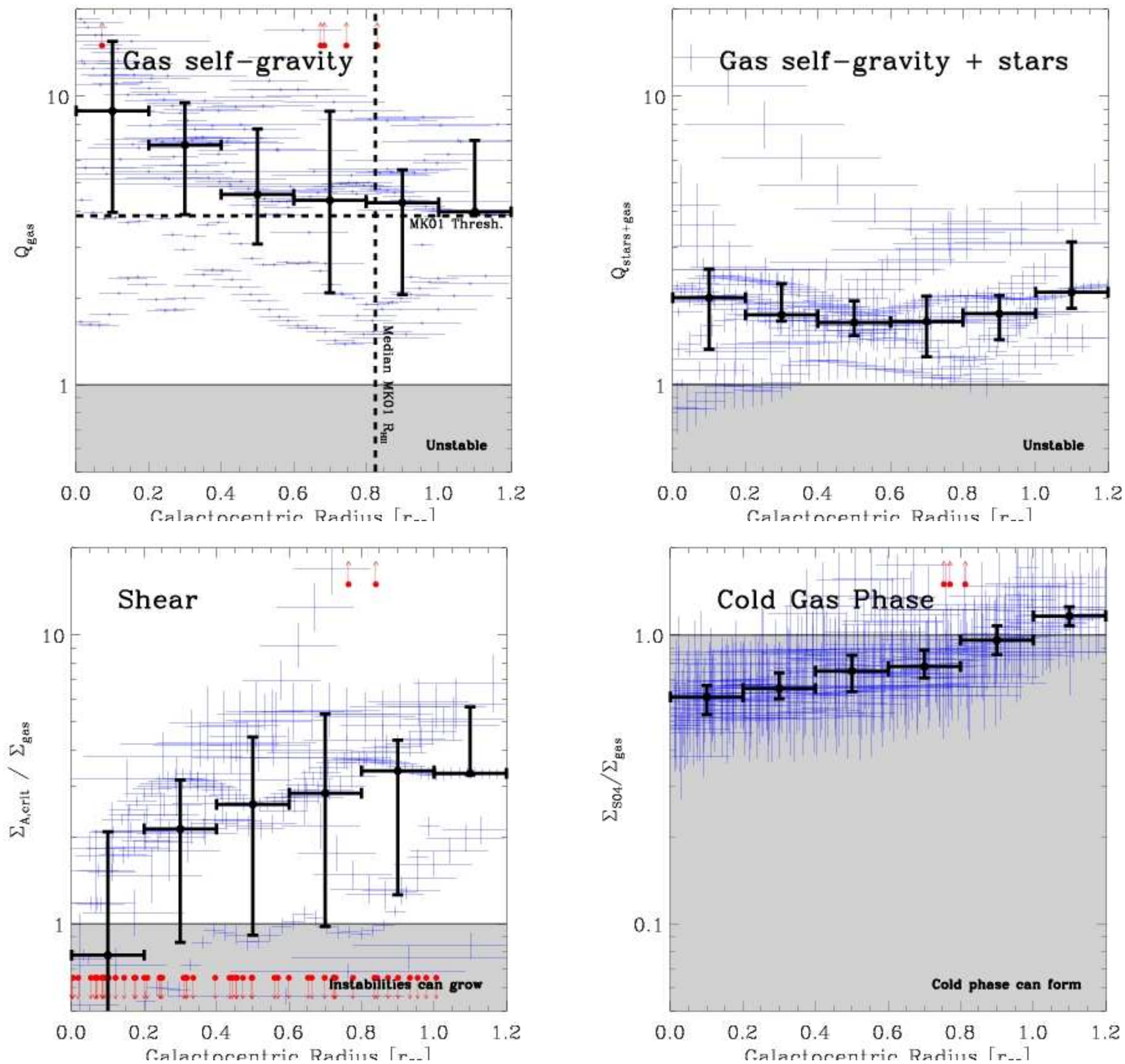

FIG. 10.— Radial behavior of thresholds in dwarf galaxies: (*top left*) gravitational instability due to gas self gravity; (*top right*) gravitational instability due to the combination of self–gravity and stellar gravity; (*bottom left*) competition between cloud formation and destruction by shear; (*bottom right*) formation of a cold phase. Each point shows average $\Sigma_{crit}/\Sigma_{gas}$ over one 10″ tilted ring in one galaxy. Gray regions show the condition required for star formation.

instability that corresponded well with the distribution of star formation. If we match their adopted σ_{gas} (5 km s^{-1}) and assumptions regarding σ_* (constant at 15 km s^{-1}) we also find widespread instability throughout our dwarf subsample, $Q_{stars+gas}$ decreasing with radius; we find a similar result for spirals if we fix a typical outer–disk σ_*.

Our approach is motivated by observations of disk galaxies (see Appendix B), but direct observations of σ_* at large radii are still sorely needed.

4.3.3. *Shear Threshold*

If clouds form efficiently, e.g., through the aid of magnetic fields to dissipate angular momentum, then Hunter et al. (1998a) suggest that the time available for a perturbation to grow in the presence of destructive shear may limit where star formation is widespread. Kim & Ostriker (2001) describe a similar scenario where magneto-Jeans instabilities can grow in regions with weak shear or strong magnetic fields. In the bottom left panels of Figures 9 and 10, we plot this shear threshold as a function of radius and in Figure 13 we compare it to the SFE.

The gray region shows the condition for instabilities to grow into GMCs, $\Sigma_{crit,A}/\Sigma_{gas} < 1$. This matches the condition $Q_{gas} < 1$ where $\beta = 0$, e.g., in outer disks of spirals. In the inner parts of spirals and in dwarf galaxies, however, $\Sigma_{crit,A}/\Sigma_{gas}$ is lower than Q_{gas}, i.e., the conditions for star formation are more nearly supercritical (because shear is low in these regions). These areas harbor H_2 or widespread star formation, so supercritical values are expected.

This trend of more supercritical data at lower radii agrees with the steady increase of SFE with decreasing radius that we saw in Figure 1. However, the scatter in $\Sigma_{crit,A}/\Sigma_{gas} < 1$ is as large as that in Q_{gas} (as one would expect from their forms, see Table 1). As a result, a direct plot of SFE against $\Sigma_{crit,A}/\Sigma_{gas}$ does not yield

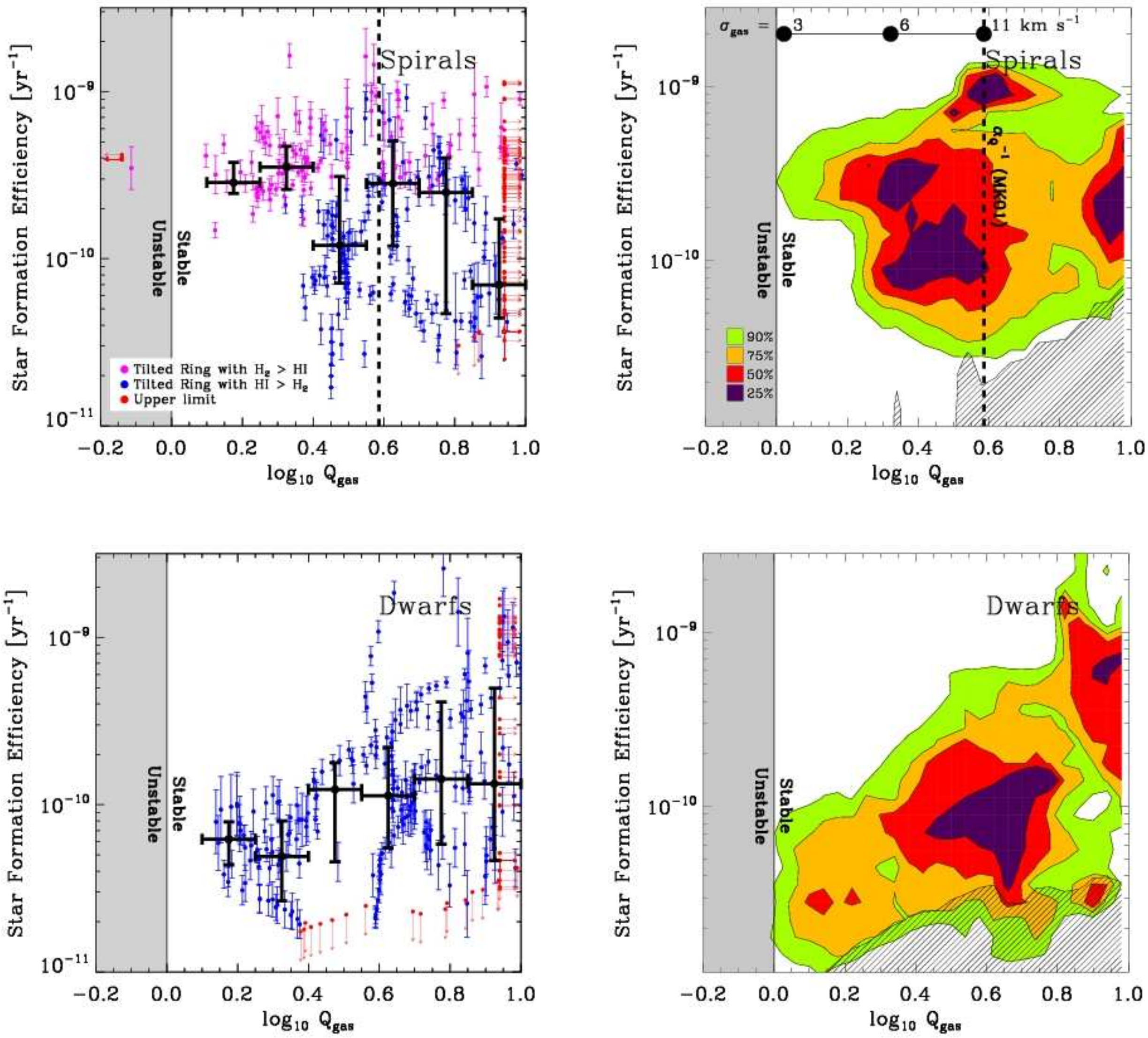

FIG. 11.— SFE as a function of $Q_{\rm gas}$, the Toomre Q parameter, which measures instability to axisymmetric collapse in a gas disk. Symbols and conventions follow Figure 1. The gray region shows where instability is expected. A dashed line in the top right panel shows the $Q_{\rm gas}$ threshold derived from Hα emission by Martin & Kennicutt (2001) converted to our assumptions. In the same panel, we show the effect on $Q_{\rm gas}$ of changing σ_g from our adopted 11 km s^{-1} to 6 km s^{-1} and then 3 km s^{-1}, expected for a cold phase.

clear threshold behavior or a strong correlation between $\Sigma_{\rm crit,A}/\Sigma_{\rm gas}$ and SFE. The strongest conclusion we can draw is that the inner parts of both spiral and dwarf galaxies are marginally stable for the shear threshold (an improvement over $Q_{\rm gas}$ and $Q_{\rm stars+gas}$ in these regions).

4.3.4. *Cold Phase Formation*

Even where the ISM is stable against gravitational collapse on large scales, star formation may still proceed if a cold (narrow-line width) phase can form locally and thus induce gravitational instability in a fraction of the gas (recall the effect of lower $\sigma_{\rm gas}$ in Figure 11). Schaye (2004) argued that this is the usual path to star formation in the outer parts of galaxies and modeled the critical gas surface density for such a phase to form, $\Sigma_{\rm S04}$. The bottom right panels in Figures 9 and 10 show $\Sigma_{\rm S04}/\Sigma_{\rm gas}$ as a function of radius and Figure 14 shows the SFE as a function of this ratio. The gray area in both figures shows where a cold phase can form.

We calculate $\Sigma_{\rm S04}$ from Equation 20, which depends on $I/[10^6~{\rm cm}^{-2}~{\rm s}^{-1}]$, the flux of ionizing photons. In outer disks, we assume $I = 10^6~{\rm cm}^{-2}~{\rm s}^{-1}$, Schaye's fiducial value, and in inner disks we take $I \propto \Sigma_{\rm SFR}$,

$$I \approx 10^6~{\rm cm}^{-2}~{\rm s}^{-1}~\left(\frac{\Sigma_{\rm SFR}}{5\times10^4~{\rm M}_\odot~{\rm yr}^{-1}~{\rm kpc}^{-2}}\right)~. \quad (26)$$

The normalization is the average $\Sigma_{\rm SFR}$ between 0.8–1.0 r_{25} in our spiral subsample.

Equation 20 also accounts for variations about Schaye's fiducial metallicity $Z = 0.1~Z_\odot$, typical for the outer disk of a spiral. We lack estimates of Z and so neglect this term but note the sense of the uncertainty. Inner galaxy disks will tend to have higher metallicities, which will lower $\Sigma_{\rm S04}$. We already find $\Sigma_{\rm gas} > \Sigma_{\rm S04}$ over most inner disks; therefore missing Z seems unlikely to seriously bias our results.

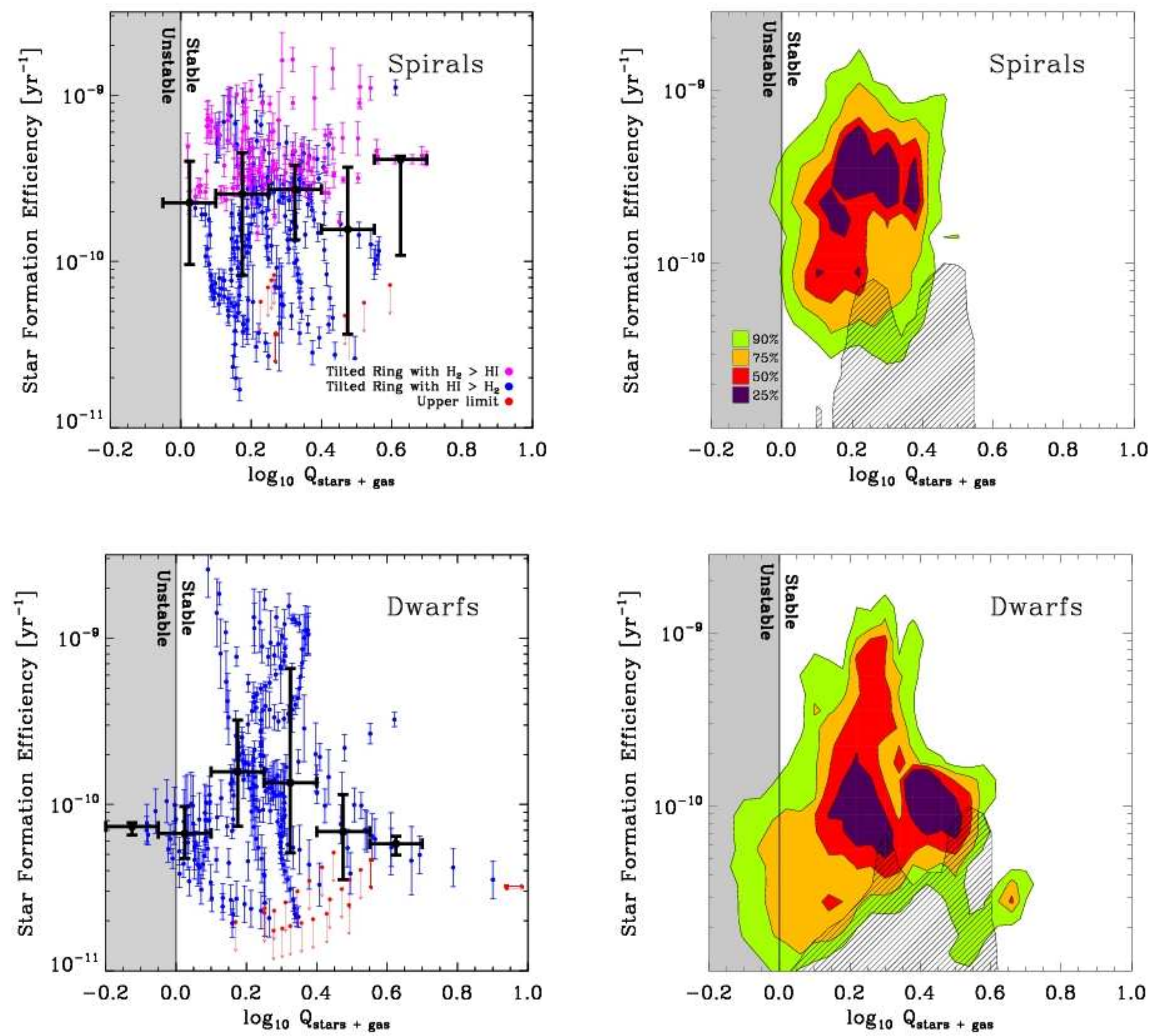

FIG. 12.— SFE as a function of $Q_{\rm stars+gas}$ (Rafikov 2001), which measures instability in a gas disk in the presence of a collisionless stellar disk. Symbols and conventions follow Figure 1. The gray region indicates where gas is unstable. Compared to $Q_{\rm gas}$, including stars renders the disk more nearly unstable and yields a much lower range of values.

Figures 9, 10, and 14 show that we expect a cold phase over most of the disk in both spiral and dwarf galaxies. In our spiral subsample, most data inside $r_{\rm gal} \sim 0.9\ r_{25}$ meet this criterion. Because most subcritical data come from large radii, we also find that most lines of sight with $\Sigma_{\rm gas} < \Sigma_{\rm S04}$ exhibit low SFEs or upper limits.

Because most data are supercritical, the Schaye (2004) threshold is of limited utility for predicting the SFE *within* a galaxy disk. Schaye (2004) does not predict the ratio of H$_2$–to–H I where cold gas forms; he is primarily concerned with the edges of galaxies. Figures 9 and 14 broadly confirm that his proposed threshold matches both the edge of the optical disk and the typical threshold found by Martin & Kennicutt (2001).

This relevance of this comparison to the SFE within the optical disk is that based on the Schaye (2004) model, we expect a widespread narrow–line phase throughout most of our galaxies (Wolfire et al. 2003, obtain a similar result for the Milky Way). This suggests that cold phase formation followed by collapse may be a common path to star formation and offers a way to form stars in our otherwise stable disks.

5. DISCUSSION

In §4.1, 4.2 and 4.3 we examined the SFE as a function of basic physical parameters, laws, and thresholds. Here we collect these results into general conclusions regarding the SFE in galaxies and identify key elements of a successful theory of star formation in galaxies.

5.1. *Fixed SFE of* H$_2$

Using a data set that overlaps the one presented here, Bigiel et al. (2008) found a linear relationship between $\Sigma_{\rm SFR}$ and $\Sigma_{\rm H2}$. Here we extend that finding: *Where the ISM is mostly* H$_2$ *in spiral galaxies, the SFE does not vary strongly with any of the quantities that we consider*, including radius, $\Sigma_{\rm gas}$, Σ_*, $P_{\rm h}$, $\tau_{\rm orb}$, and β. We plot SFE (H$_2$) as a function of each of these quantities in

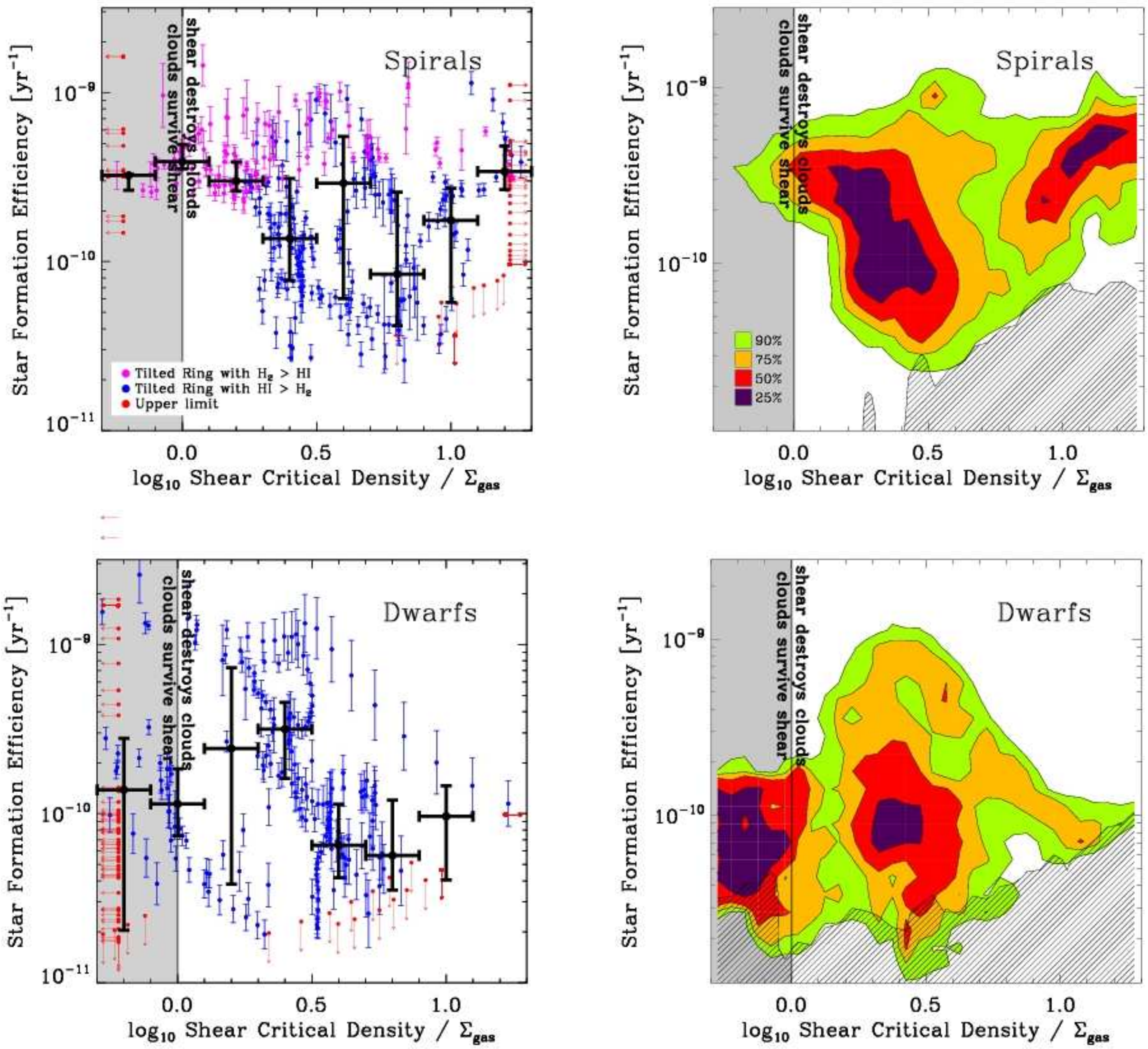

FIG. 13.— SFE as a function of $\Sigma_{\rm crit,A}/\Sigma_{\rm gas}$, the threshold for cloud growth in the presence of shear (Hunter et al. 1998a) for spiral (top row) and dwarf (bottom row) galaxies. Conventions and symbols follow Figure 1. The gray area shows where clouds should be able to survive distribution by shear.

Figure 15. The median value for tilted rings from our spiral subsample is $\log_{10}$ SFE (H_2) $= -9.28 \pm 0.17$, i.e.,

$$\text{SFE (H}_2\text{)} = 5.25 \pm 2.5 \times 10^{-10}\ \text{yr}^{-1}\ . \qquad (27)$$

Constant SFE (H_2) might be expected if 1) conditions within a GMC, rather than the larger scale properties of the ISM, drive star formation (e.g., Krumholz & McKee 2005) and 2) GMC properties are relatively universal rather than, e.g., a sensitive function of formation mechanism or environment. This appears to be the case in the inner Milky Way (excluding the Galactic center) and in M31 and M33, where GMC properties are largely a function of cloud mass alone (Solomon et al. 1987; Rosolowsky et al. 2003; Rosolowsky 2007; Blitz et al. 2007; Bolatto et al. 2008). The constancy of SFE (H_2) hints that a similar case holds in our spiral subsample.

Figure 6 illustrates why (relatively) universal GMC properties may be plausible in our sample. From Equation 9, the internal pressure of a starless GMC with $\Sigma_{\rm gas} \approx 170$ M$_\odot$ pc^{-2} (Solomon et al. 1987) is $P_{\rm h}/k_{\rm B} \sim 10^6$ K cm^{-3}. This is the highest value we plot in Figures 6 and 15 and only a small fraction of our data have higher $P_{\rm h}$ so that even where the ISM is mostly H_2, $P_{\rm h}$ is usually well below the typical internal pressure of a GMC. Thus GMCs are not necessarily pressure-confined, which allows the possibility of bound, isolated GMCs out of pressure equilibrium with the rest of the ISM. In this case, the environmental factors that we consider may never be communicated to GMCs (though some mechanism may still be needed to damp out any imprint left by environment during GMC formation).

The range of $P_{\rm h}$ in our sample also underscores that one should not expect a constant SFE (H_2) to extend to starburst conditions, where $P_{\rm h}$ and $\Sigma_{\rm gas}$ on kiloparsec scales exceed those found for individual Galactic GMCs and SFE (H_2) *is* observed to vary strongly with local conditions (e.g., Kennicutt 1998a; Riechers et al. 2007).

Another important caveat is that the distribution

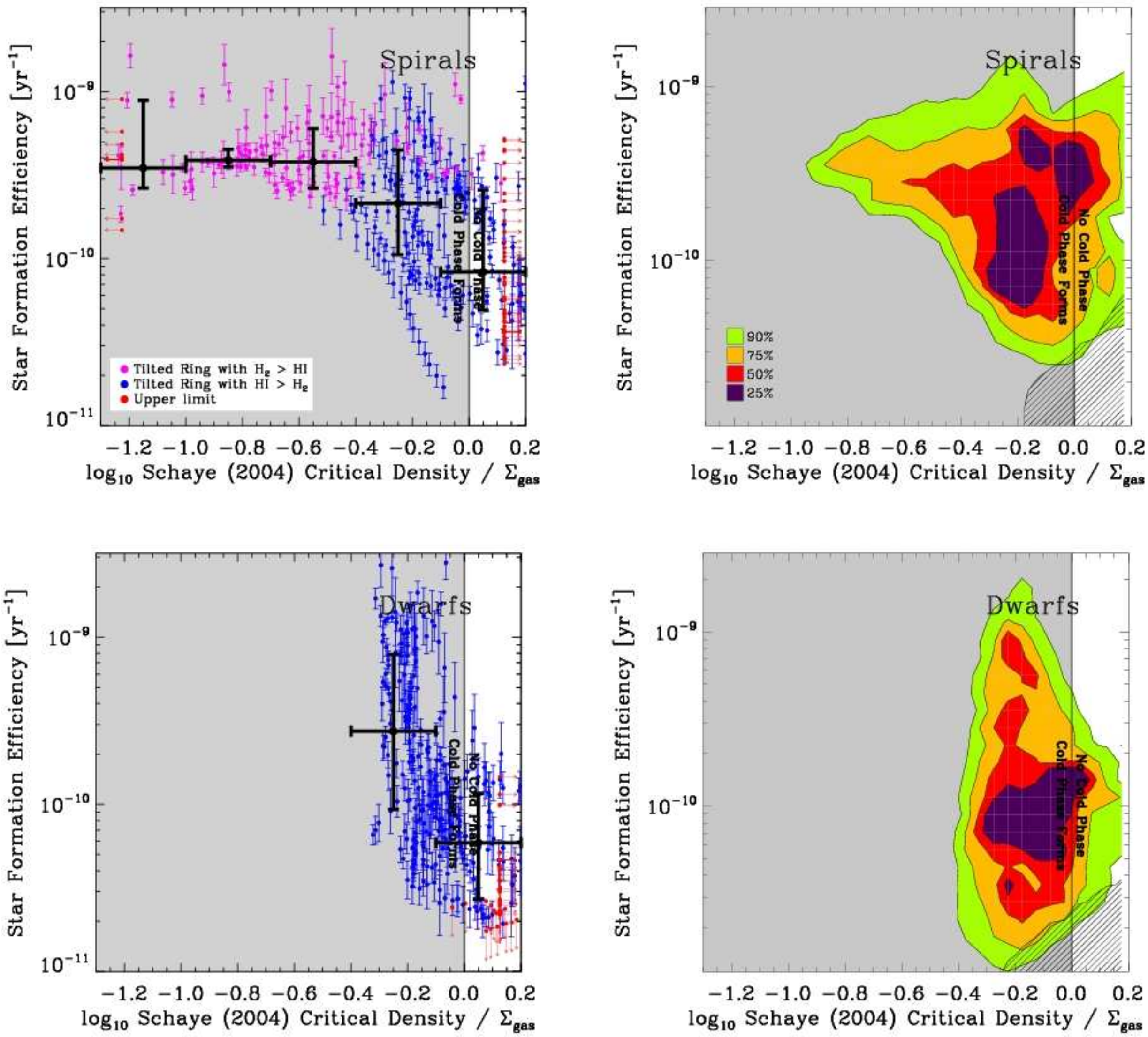

FIG. 14.— SFE as a function of $\Sigma_{S04}/\Sigma_{gas}$, the threshold for the formation of a cold phase Schaye (2004), for spiral (top row) and dwarf galaxies (bottom row). Conventions and symbols follow Figure 1. The gray area indicates where Schaye (2004) estimates that a cold phase can form. Most areas where we observe star formation meet this criterion and the areas that do not tend to have low SFE.

of GMC masses is observed to vary with environment (Rosolowsky 2005), possibly as a result of varying formation mechanisms. This suggests that either the SFE of a GMC is only a weak function of its mass (and thus other properties) or that real variations in SFE (H_2) may exist in dwarf galaxies and the outskirts of spirals.

5.2. *Conditions at the* H I*-to–*H_2 *Transition in Spirals*

In spiral galaxies, the transition between an H I–dominated ISM and a mostly–H_2 ISM occurs at a characteristic value for most quantities. This can be seen from Figures 1, 3, 5, 6, and 7, in which H I-dominated regions (blue points) typically occupy one region and H_2-dominated regions (magenta points) occupy another.

Table 5 gives our estimates of properties where $\Sigma_{HI} \approx \Sigma_{H2}$ in spiral galaxies. For each galaxy, we measure the median of the property in question over all pixels where $\Sigma_{H2} = 0.8 - 1.2\ \Sigma_{HI}$. Table 5 lists the median transition value in our spiral subsample, along with the (1σ) scatter and log scatter among galaxies. These values appear as dotted vertical lines in Figures 1, 5, 3, 6, and 7. Note that methodology — the choice to use pixels or rings, to interpolate, use the mean or median, etc. — affects the values in Table 5 by $\sim 20\%$.

From Table 5, we find that physical conditions at the H I–to–H_2 transition are fairly similar to those found in the solar neighborhood. The orbital time is $\approx 1.8 \times 10^8$ years and the free–fall time in the gas disk is $\approx 4.2 \times 10^7$ years. The midplane gas pressure is $P_{\rm h}/k_{\rm B} \approx 2.3 \times 10^4$ cm^{-3} K, corresponding to a particle density $n \sim 1$ cm^{-3}. The baryon mass budget in the disk is dominated by stars, $\Sigma_* \approx 81$ M$_\odot$ pc^{-2} while $\Sigma_{gas} \approx 14$ M$_\odot$ pc^{-2}. Accordingly, the gas is stable against large scale gravitational collapse on its own ($Q_{gas} \approx 3.8$), but in the presence of stars is only marginally stable $Q_{stars+gas} \sim 1.6$.

Approximately 1% of gas is converted to stars per free fall time at the transition, in agreement with expecta-

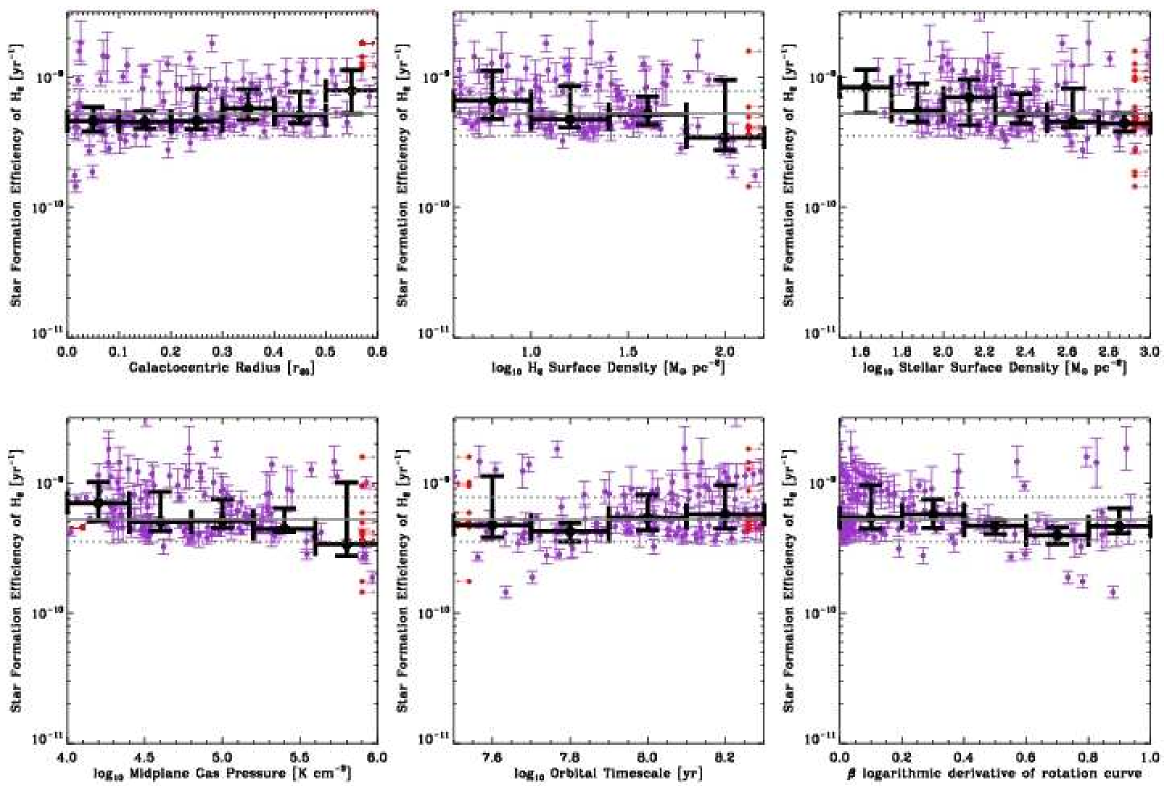

FIG. 15.— SFE (H_2) in individual tilted rings from spiral galaxies as a function of: (*top left*) galactocentric radius, (*top middle*) H_2 surface density, (*top right*) stellar surface density, (*bottom left*) midplane pressure, (*bottom middle*) orbital timescale, (*bottom right*) logarithmic derivative of the rotation curve. Gray lines show the median $\log_{10}$ SFE (H_2) $= -9.28 \pm 0.17$ for our data.

TABLE 5
CONDITIONS AT THE H I-TO-H_2 TRANSITION

Quantity	Median Value[a]	Scatter	Scatter in $\log_{10}$
$r_{\rm gal}$ [r_{25}]	0.43	0.18	0.17
Σ_* [$M_\odot$ pc^{-2}]	81	25	0.15
$\Sigma_{\rm gas}$ [$M_\odot$ pc^{-2}]	14	6	0.18
P_h/k_B [cm^{-3} K]	2.3×10^4	1.5×10^4	0.26
$\tau_{\rm ff}$ [yr]	4.2×10^7	1.2×10^7	0.14
$\tau_{\rm orb}$ [yr]	1.8×10^8	0.4×10^8	0.09
$Q_{\rm gas}$	3.8	2.6	0.31
$Q_{\rm stars+gas}$	1.6	0.4	0.09

[a]Median value in the spiral subsample.

tions by Krumholz & McKee (2005). About 6% of gas is converted to stars per $\tau_{\rm orb}$. This agrees well with the disk–averaged value of $\sim$ 7% derived by Kennicutt (1998a) (adapted to our IMF and CO-to-H_2 conversion factor) and with the range of efficiencies found by Wong & Blitz (2002).

5.3. *H_2 in Dwarf Galaxies*

Because of uncertainties in $X_{\rm CO}$, we do not directly estimate the amount of H_2 in dwarf galaxies . However, indirect evidence suggests that a significant part of the ISM is H_2 in the central parts of these galaxies. Specifically, we observe very high SFE in the centers of dwarf galaxies — higher than SFE (H_2) in spirals — often under conditions associated with an H_2-dominated ISM in spirals (§5.2). It would be surprising if the SFE of H I in dwarfs indeed exceeds SFE (H_2) in spirals. We argue that an unaccounted–for reservoir of H_2 is a more likely explanation.

The SFE (H_2) that we observe in spiral galaxies offers an approximate way to estimate how much H_2 may be present. If we assume that SFE (H_2) is the same in dwarf and spiral galaxies then we can calculate $\Sigma_{\rm H2}$ from the observed $\Sigma_{\rm SFR}$ via

$$\Sigma_{\rm H2} \approx \frac{10^{-6}\ \Sigma_{\rm SFR}}{5.25 \times 10^{-10}\ {\rm yr}^{-1}}\ . \qquad (28)$$

This treatment suggests that in our typical dwarf galaxies, most of the ISM is H_2 within $\sim 0.25\ r_{25}$. This may be seen directly from Equation 24, which translates our fit of SFE to radius to a relation between $R_{\rm mol}$ and radius assuming Equation 28. From Equation 24, $\Sigma_{\rm H2}/\Sigma_{\rm HI}$ in dwarf galaxies is 1–2 inside $\sim 0.25\ r_{25}$, rising as high as ~ 3 at $r_{\rm gal} = 0$.

5.4. *Environment-Dependent GMC/H_2 Formation*

Where the ISM is H I–dominated — in dwarf galaxies and outside the H I-to-H_2 transition in spirals — the SFE declines steadily with increasing radius. In this regime, the SFE is covariant with a number of environmental factors, including Σ_*, pressure, density, free fall time, and orbital timescale. This observation, together with those in §5.1 and 5.2, implies that while star formation *within* GMCs is largely decoupled from environment, *the formation of H_2 / GMCs from* H I *depends sensitively on local conditions.*

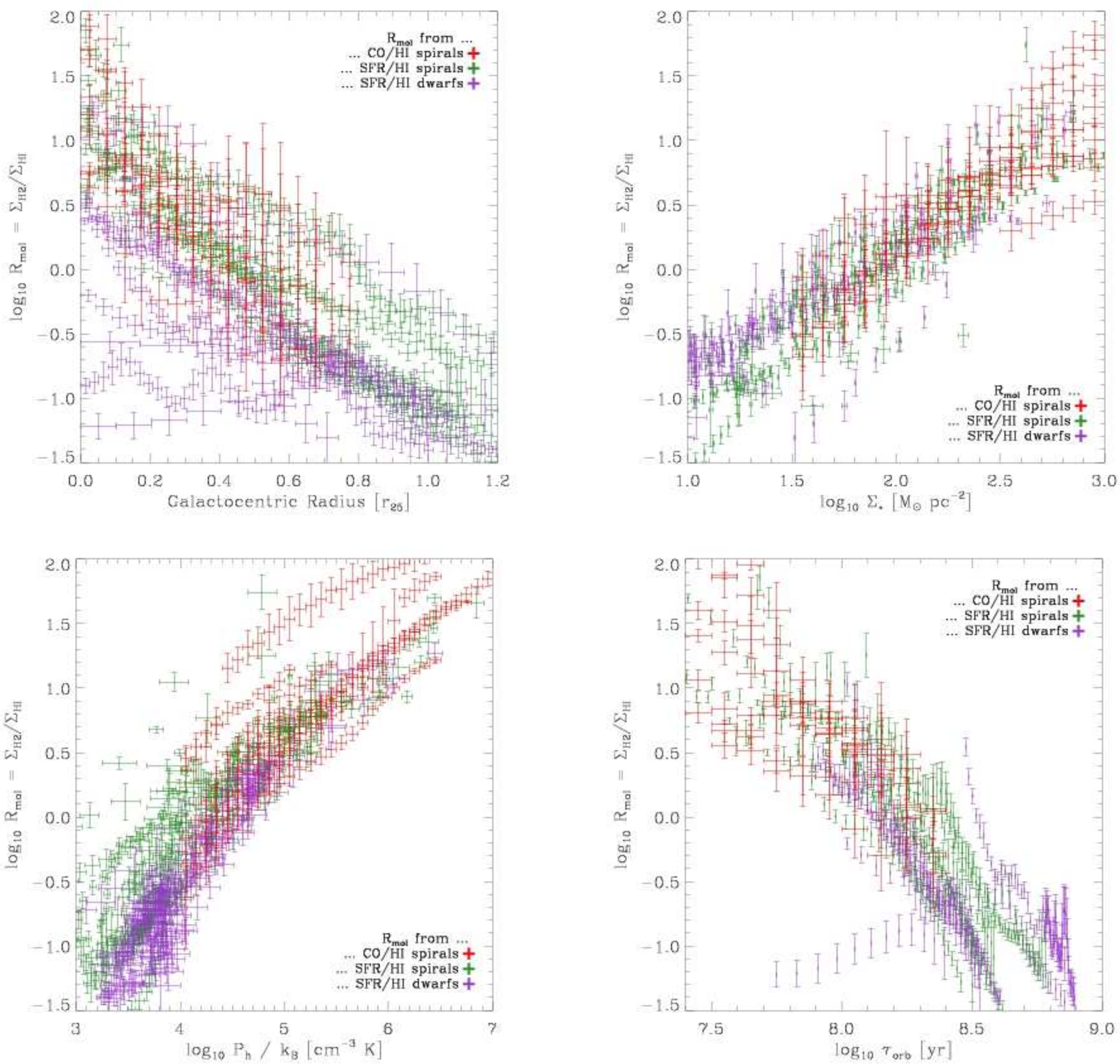

FIG. 16.— The H_2–to–H I ratio, $R_{\rm mol} = \Sigma_{\rm H2}/\Sigma_{\rm HI}$, as a function of (*top left*) radius, (*top right*) Σ_*, (*bottom left*) $P_{\rm h}$ ($\propto \tau_{\rm ff}^{-2}$), and (*bottom right*) $\tau_{\rm orb}$. Red points are pixel–by–pixel measurements of $R_{\rm mol}$ in spirals, binned by the quantity on the x-axis. Green and purple points show tilted rings in spiral and dwarf galaxies with $R_{\rm mol}$ inferred from $\Sigma_{\rm SFR}$ and $\Sigma_{\rm HI}$ assuming a fixed SFE (H_2). We show the same data, binned, in Figure 17.

In this case, we can break the SFE into two parts: star formation within GMCs and GMC formation, so that

$$\mathrm{SFE} = \mathrm{SFE}\,(\mathrm{H}_2)\,\frac{\Sigma_{\rm H2}}{\Sigma_{\rm gas}} = \mathrm{SFE}\,(\mathrm{H}_2)\,\frac{R_{\rm mol}}{R_{\rm mol}+1}\ , \qquad (29)$$

i.e., the SFE is a product of a constant SFE (H_2) and $R_{\rm mol} = \Sigma_{\rm H2}/\Sigma_{\rm HI}$, which is a function of local conditions.

We show this directly in Figure 16 and plot the same data, binned, in Figure 17. We plot $R_{\rm mol} = \Sigma_{\rm H2}/\Sigma_{\rm HI}$ on the y-axis as a function of radius, Σ_*, $P_{\rm h}$ ($\propto \tau_{\rm ff}^{-2}$), and $\tau_{\rm orb}$. Red points show direct measurements of $R_{\rm mol}$ from CO and H I assembled following the methodology used by Blitz & Rosolowsky (2006) to compute $R_{\rm mol}$ as a function of $P_{\rm h}$:

1. For each galaxy, we examine scatter plots to estimate a value of $P_{\rm h}$ above which our pixel-by-pixel measurements of $\Sigma_{\rm H2}$ are approximately complete.
2. Where $P_{\rm h}$ is above this limit, we measure $R_{\rm mol}$ for each pixel.
3. We sort pixels into bins based on $P_{\rm h}$ and calculate the average and scatter in $\log_{10} R_{\rm mol}$ for the pixels in each bin.

A red point in Figure 16 corresponds to one $P_{\rm h}$ bin in one spiral galaxy; the x– and y–error bars indicate the width of the bin and the scatter in $R_{\rm mol}$ within the bin. We carry out analogous procedures to compute $R_{\rm mol}$ as a function of $r_{\rm gal}$, Σ_*, and $\tau_{\rm orb}$.

Because of the limited sensitivity of the CO data, these direct measurements of $R_{\rm mol}$ seldom probe far below $R_{\rm mol} = 1$ and do not extend to dwarfs. Therefore we also use $\Sigma_{\rm SFR}$ and $\Sigma_{\rm HI}$ to estimate $R_{\rm mol}$ by assuming a fixed SFE (H_2). For each tilted ring in both subsamples, we convert $\Sigma_{\rm SFR}$ into $\Sigma_{\rm H2}$ using Equation 28. We divide this by the observed $\Sigma_{\rm HI}$ to estimate $R_{\rm mol}$ for that ring.

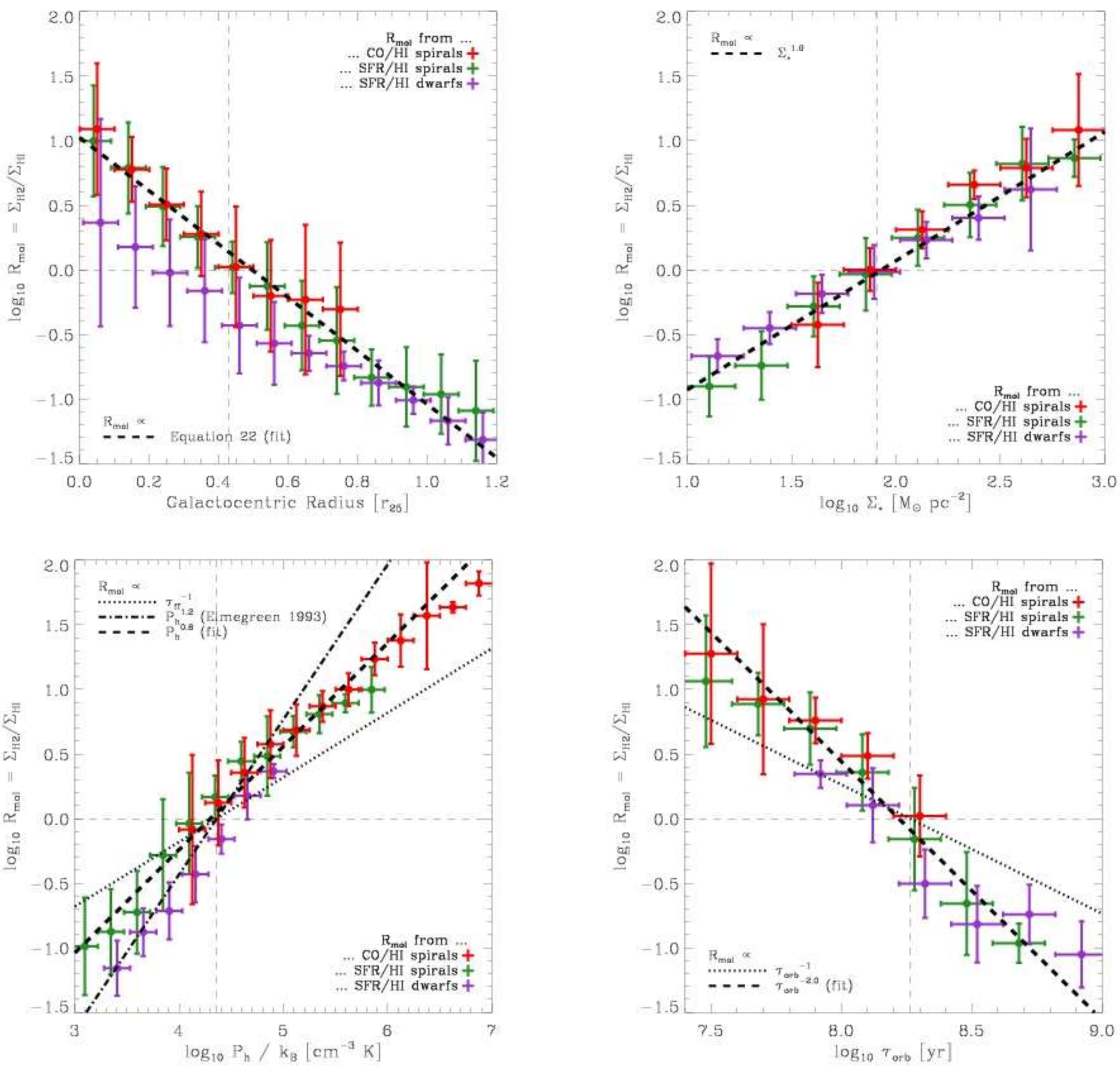

FIG. 17.— The data from Figure 16, binned by the quantity on the x–axis into three trends: $R_{\rm mol}$ measured pixel–by–pixel in spirals (red) and inferred from $\Sigma_{\rm SFR}$ and $\Sigma_{\rm HI}$ in (green) spiral and (purple) dwarf galaxies. Thin dashed lines show $R_{\rm mol} = 1$ (horizontal) and our estimate of each quantity at the H I–to–H_2 transition (vertical). Dotted lines show $R_{\rm mol} \propto \tau_{\rm ff}^{-1}$ (bottom left) and $R_{\rm mol} \propto \tau_{\rm orb}^{-1}$ (bottom right). Thick dashed lines show fits of $R_{\rm mol}$ to each quantity.

We plot the results as green points for spirals and purple points for dwarf galaxies[10]. This approach — essentially plotting SFE (H I) in units of $R_{\rm mol}$ — allows us to estimate $R_{\rm mol}$ far below the sensitivity of our CO maps. While this extrapolation of SFE (H_2) may be aggressive, the quantity $\Sigma_{\rm SFR}/\Sigma_{\rm HI}$ must be closely related to the ability of H I to assemble into star–forming clouds.

Figure 17 shows the data in Figure 16 binned by the quantity on the x-axis. Thin dashed lines horizontal show $R_{\rm mol} = 1$, i.e., $\Sigma_{\rm HI} = \Sigma_{\rm H2}$, and the value of the property on the x-axis that we estimate at the H I–to–H_2 transition (§5.2 and Table 5). Dashed and dotted lines show fits and expectations that we discuss later in this section.

In spirals, the agreement between direct measurements of $R_{\rm mol}$ and estimates based on $\Sigma_{\rm SFR}$ and $\Sigma_{\rm HI}$ is quite good. There is also general agreement between spirals and dwarf galaxies: the two subsamples sweep out similar, though slightly offset, trends in all four panels. The magnitude of the offsets between dwarf and spiral galaxies that we see in Figure 17, typically 0.2–0.3 dex, offers indirect evidence that differences between the subsamples — metallicity, radiation fields, spiral structure (§3.1) — affect cloud formation or SFE (H_2) at the factor of ~ 2–3 level.

Figures 16 and 17 show explictly what we have already seen indirectly throughout §4. $R_{\rm mol}$ is a continuous function of environment spanning from the H_2–dominated ($R_{\rm mol} \sim 10$) to H I–dominated ($R_{\rm mol} \sim 0.1$) ISM, from inner to outer galaxy disks, and over a wide range of ISM pressures. This qualitatively confirms and extends similar findings by Wong & Blitz (2002) and Blitz & Rosolowsky (2006), which were mostly confined to the

[10] Because $P_{\rm h}$ depends on $\Sigma_{\rm gas}$, we make a first–order correction to $P_{\rm h}$ in dwarf galaxies based on the estimated $R_{\rm mol}$.

inner, molecule–dominated parts of spirals.

5.4.1. *Cloud Formation Timescales*

In §2, we discuss two basic ways that $R_{\rm mol}$ might be set by environment. First, the timescale to form GMCs may depend on local conditions. If H I and H_2 are in approximate equilibrium, with the entire neutral ISM actively cycling between these two phases, then

$$R_{\rm mol} = \frac{\Sigma_{\rm H2}}{\Sigma_{\rm HI}} \approx \frac{\rm GMC\ lifetime}{\tau\,({\rm H\ I} \rightarrow {\rm H_2})}\ . \tag{30}$$

For constant GMC lifetimes — perhaps a reasonable extension of fixed SFE (H_2) — $R_{\rm mol}$ is set by $\tau\,({\rm H\ I} \rightarrow {\rm H_2})$. In §4.2.2 and §4.2.3 we saw that SFE anti-correlates with $\tau_{\rm ff}$ and $\tau_{\rm orb}$ where $\Sigma_{\rm HI} > \Sigma_{\rm H2}$. If GMCs form over these timescales then $R_{\rm mol} \propto \tau_{\rm ff}^{-1}$ or $R_{\rm mol} \propto \tau_{\rm orb}^{-1}$.

However, we found that the SFE decreased more steeply than one would expect if these timescales alone dictated $R_{\rm mol}$, so that increasing timescale for GMC formation cannot explain all of the decline in $R_{\rm mol}$. Figures 16 and 17 show this directly: dotted lines in the bottom two panels illustrate $R_{\rm mol} \propto \tau_{\rm ff}^{-1}$ and $R_{\rm mol} \propto \tau_{\rm orb}^{-1}$. In both cases the prediction is notably shallower than the data in both the H_2 and H I–dominated regimes.

5.4.2. *Disk Stability Thresholds*

Of course, the entire ISM may not participate in cloud formation. Star formation thresholds are often invoked to explain the decrease in SFE between inner and outer galaxy disks. The amount of stable, warm H I may depend on environment, with a variable fraction of the disk actively cycling between H I and GMCs. This suggests a straightforward extension of Equation 30,

$$R_{\rm mol} = \frac{\Sigma_{\rm H2}}{\Sigma_{\rm HI}} \approx \frac{\rm GMC\ lifetime}{\tau\,({\rm H\ I} \rightarrow {\rm H_2})} \times f_{\rm GMC\ forming}\ , \tag{31}$$

which again balances GMC formation and destruction but now includes the factor $f_{\rm GMC\ forming}$ to represent the fact that only a fraction of the H I is actively cycling between the molecular and atomic ISM.

We considered three thresholds in which large–scale instabilities dictate $f_{\rm GMC\ forming}$ — $Q_{\rm gas}$, $Q_{\rm stars+gas}$, and shear. One would naively expect these thresholds to correspond to $f_{\rm GMC\ forming} \sim 1$ for supercritical gas and $f_{\rm GMC\ forming} \ll 1$ for subcritical gas, yielding a step function in SFE or $R_{\rm mol}$. However, we do not observe such relationships between thresholds and SFE (§4.3), which agrees with Boissier et al. (2007) who also based their SFR profiles on extinction-corrected FUV maps and found no evidence for sharp star formation cutoffs.

If these instabilities regulate star formation but operate below our resolution, we still expect a correspondence between SFE and the average threshold value, which should indicate what fraction of the ISM is unstable. Despite this expectation, $Q_{\rm gas}$ shows little correspondence to the SFE and almost all of our sample is stable against axisymmetric collapse. Kim & Ostriker (2001) and Kim & Ostriker (2007) discuss $Q_{\rm gas}$ thresholds for the growth of non-axisymmetric instabilities, but these are in the range $Q_{\rm gas} \sim$ 1–2, still lower than the typical values that we observe (§4.3.1). Even independent of the normalization, $Q_{\rm gas}$ shows little relation to the SFE, particularly in dwarf galaxies (see also Hunter et al. 1998a; Wong & Blitz 2002; Boissier et al. 2003).

Including the effects of stellar gravity reduces stability. Over most of our sample, $Q_{\rm stars+gas} \lesssim 2$ with a much narrower range than $Q_{\rm gas}$ (similar improvements were seen by Boissier et al. 2003; Yang et al. 2007). These values are roughly consistent with the conditions for cloud formation found from simulations. Li et al. (2005) find gas collapses where $Q_{\rm stars+gas} \lesssim 1.6$ and Kim & Ostriker (2001, 2007) find runaway instabilities where $Q_{\rm gas} \lesssim 1.4$ (though this is $Q_{\rm gas}$ and not $Q_{\rm stars+gas}$; for a region like the solar neighborhood, Kim & Ostriker 2007, argue that disk thickness, which tends to increase stability, approximately offsets the effect of stars on Q).

$Q_{\rm stars+gas}$ increases towards the central parts of spirals, so that although the ISM in these regions is usually dominated by H_2, they appear more stable than gas near the H I–to–H_2 transition. Hunter et al. (1998a) and Kim & Ostriker (2001) suggest that because of low shear, instabilities aided by magnetic fields may grow in these regions despite supercritical Q. Comparing to the shear threshold proposed by Hunter et al. (1998a), we find some support for this idea: at $\lesssim 0.2\ r_{25}$ many dwarf and spiral galaxies appear unstable or marginally stable. As with $Q_{\rm gas}$, however, $\Sigma_{\rm crit,A}/\Sigma_{\rm gas}$ shows large scatter and no clear ability to predict the SFE.

Thus, we find no clear evidence that disk stability at large scales drives the observed variations in SFE and $R_{\rm mol}$. Improved handling of second–order effects (disk thickness, $\sigma_{\rm gas}$, $X_{\rm CO}$, σ_*, and $\Upsilon_\star^K$) may change this picture, but comparing our first–order analysis to expectations and simulations, disks appear marginally stable more or less throughout with little correlation between proposed thresholds and SFE.

5.4.3. *Cold Phase Formation*

Timescales and thresholds computed at 400 (dwarfs) and 800 pc (spirals) scales do not offer a simple way to predict $R_{\rm mol}$. An alternative view is that physics on smaller scales regulates cloud formation. Comparison with models by Schaye (2004) suggests that a cold phase can form across the entire disk of most of our sample, which agrees with results from Wolfire et al. (2003) modeling our own Galaxy. High density, narrow–linewidth clouds may easily be unstable or be rendered so by the passage of spiral arms or supernova shocks, even where the ISM as a whole is subcritical. Both Schaye (2004) and de Blok & Walter (2006) have emphasized the effect of lower $\sigma_{\rm gas}$ on instability and we have seen that a shift from the observed $\sigma_{\rm gas} = 11$ km s^{-1} to $\sigma_{\rm gas} = 3$ km s^{-1} would render most gas disks in our sample unstable or marginally stable (of course a proper calculation requires estimating the density and fraction of the mass in this phase as well).

A narrow–line component is observed from high–velocity resolution H I observations of nearby irregular galaxies (Young et al. 2003; de Blok & Walter 2006), but an important caveat is the lack of direct evidence for such a component in THINGS. With ~ 2.5 or 5 km s^{-1} velocity resolution, one cannot distinguish a narrow component directly. Therefore, Usero et al. (2008) followed up on work by Braun (1997), who used the peak intensity along each line of sight to estimate the maximum contri-

TABLE 6
FITS[a] OF $R_{\rm mol} = \Sigma_{\rm H2}/\Sigma_{\rm HI}$ TO $(P_{\rm h}/P_0)^\alpha$

Source	$\log_{10} P_0/k_{\rm B}$ ($\rm cm^{-3}$ K)	α
spiral subsample (CO/H I)	4.19	0.73
spiral subsample (SFR/H I)[b]	4.30	0.79
spiral subsample (combined)	4.23	0.80
dwarf subsample (SFE/H I)[b]	4.51	1.05
Wong & Blitz (2002)	···	0.8
Blitz & Rosolowsky (2006)	4.54 ± 0.07	0.92 ± 0.07

[a]Over the range $R_{\rm mol} = 0.1 - 10$.
[b]Estimating $\Sigma_{\rm H2}$ from $\Sigma_{\rm SFR}$.

bution from a cold phase and found pervasive networks of high brightness filaments. Usero et al. (2008) find no clear evidence for a cold phase traced by networks of high brightness filaments, suggesting that a cold phase, if present, is mixed with the warm phase at the THINGS resolution of several times ~ 100 pc.

5.4.4. $R_{\rm mol}$ *and Pressure*

Despite this caveat, our results offer significant circumstantial support that ISM physics below our resolution dictates $R_{\rm mol}$: the lack of obvious threshold behavior, marginal stability of our disks, the ability of a cold phase to form, and the continuous variations in SFE and $R_{\rm mol}$ as a function of radius, Σ_*, and $P_{\rm h}$.

In particular, the relationship between $R_{\rm mol}$ and $P_{\rm h}$ has been studied before. Following theoretical work by Elmegreen (1993) and Elmegreen & Parravano (1994), Wong & Blitz (2002) and Blitz & Rosolowsky (2006) showed that $R_{\rm mol}$ and $P_{\rm h}$ correlate in nearby spiral galaxies (mostly at $R_{\rm mol} > 1$) and Robertson & Kravtsov (2008) recently produced a similar relationship from simulations that include cool gas and photodissociation of H_2; they emphasize the importance of the latter to reproduce the observed scaling.

The dash-dotted line in the bottom left panel of Figure 17 shows $R_{\rm mol} \propto P_{\rm h}^{1.2}$, predicted by Elmegreen (1993) from balancing H_2 formation and destruction in a model ISM. This is a reasonable description of dwarf galaxies, where we derive a best–fit power law with index ≈ 1.05. Spirals show a slightly shallower relation between $R_{\rm mol}$ and $P_{\rm h}$ with best–fit power law index ≈ 0.80. The thick dashed line in the bottom left panel of Figure 17 shows our best fit to the spiral subsample (both CO/H I and SFR/H I) over the range $R_{\rm mol} = 0.1 - 10$. Table 6 lists this fit along with fits to dwarf galaxies and the results of Wong & Blitz (2002) and Blitz & Rosolowsky (2006).

The entry "spiral subsample (combined)" in Table 6 lists the best fit power law like Equation 11 for our spiral subsample. This fit has an index $\alpha = 0.80$ and normalization $\log_{10} P_0/k_{\rm B} = 4.23$ (this is an OLS bisector fit over the range $0.1 < R_{\rm mol} < 10$ giving equal weight to each of the red and green points in Figure 16). Formally, the uncertainty in the fit is small because it includes a large number of data points. However, both $\log_{10} P_0/k_{\rm B}$ and α scatter by several tenths when fit to individual galaxies. This agrees well with $\alpha = 0.8$ derived by Wong & Blitz (2002) and with $\alpha = 0.92 \pm 0.07$ obtained by Blitz & Rosolowsky (2006) given the uncertainties. Fitting the dwarf subsample in the same manner yields $\log_{10} P_0/k_{\rm B} = 4.51$, the pressure at the H I–to–H_2 transition. This is 0.2–0.3 dex higher than $\log_{10} P_0/k_{\rm B} = 4.23$ in spirals, suggesting that at the same pressure (density) GMC/H_2 formation in our dwarf subsample is a factor of ~ 2 less efficient than in spirals.

5.4.5. $R_{\rm mol}$ *and Environment*

The fits between $R_{\rm mol}$ and $P_{\rm h}$ in Table 6 are reasonable descriptions of the data, but do not represent a "smoking gun" regarding the underlying physics; radius, Σ_*, $P_{\rm h}$, and $\tau_{\rm orb}$ are all covariant and each could be used to predict $R_{\rm mol}$ with reasonable accuracy in spirals. Therefore we close our discussion by noting a set of four scaling relations between $R_{\rm mol}$ and environment that describe our spiral subsample

$$R_{\rm mol} = 10.6\ \exp\left(-r_{\rm gal}/0.21\ r_{25}\right) \quad (32)$$

$$R_{\rm mol} = \Sigma_*/81\ M_\odot\ {\rm pc^{-2}} \quad (33)$$

$$R_{\rm mol} = \left(P_{\rm h}/1.7\times10^4\ {\rm cm^{-3}\ K}\ k_{\rm B}\right)^{0.8} \quad (34)$$

$$R_{\rm mol} = \left(\tau_{\rm orb}/1.8\times10^8\ {\rm yr}\right)^{-2.0} \quad (35)$$

these appear as thick dashed lines in Figure 17.

In particular, we stress the relationship between $R_{\rm mol}$ and Σ_* (see also Figure 3). This has several possible interpretations, the most simple of which is that stars form where they have formed in the past. There are physical reasons to think relationship may be causal, however. Considering a similar finding in dwarf irregular galaxies, Hunter et al. (1998a) suggested that stellar feedback may play a critical role in triggering cloud formation. Recently the importance of the stellar potential well has been highlighted, either to triggering large-scale instabilities (Li et al. 2005, 2006; Yang et al. 2007) or in bringing gas to high densities in order for small-scale physics to operate more effectively (Elmegreen 1993; Elmegreen & Parravano 1994; Wong & Blitz 2002; Blitz & Rosolowsky 2004, 2006).

5.5. *A Note on Systematics:* $X_{\rm CO}$, $\sigma_{\rm gas}$, σ_*, $\Upsilon_\star^K$

In this paper, we work "to first order," using the simplest well-motivated assumptions to convert observations to physical quantities. These assumptions are described in §3 and Appendices A – D. These are not always unique and here we note differences with the literature and the effect that they may have on our analysis.

$X_{\rm CO}$: In spirals, we adopt a fixed $X_{\rm CO} = 2 \times 10^{20}\ {\rm cm^{-2}\ (K\ km\ s^{-1})^{-1}}$. Wong & Blitz (2002) and Blitz & Rosolowsky (2006) adopt the same value. Kennicutt (1989), Kennicutt (1998a), Martin & Kennicutt (2001), and Kennicutt et al. (2007) also use a fixed value, but a slightly higher one, $X_{\rm CO} = 2.8 \times 10^{20}\ {\rm cm^{-2}\ (K\ km\ s^{-1})^{-1}}$. Boissier et al. (2003) test the effects of a metallicity–dependent $X_{\rm CO}$ that tends to yield lower $\Sigma_{\rm H2}$ than our values in the inner parts of spirals, but higher in the outer parts.

Variations in the normalization of $X_{\rm CO}$ will affect the location of the H I–to–H_2 transition and the value of SFE (H_2), but not the observations of fixed SFE (H_2) or steadily varying $R_{\rm mol}$. A strong dependence of $X_{\rm CO}$ on environment in spirals would affect many of our results, but leave the basic observation of environment–dependent SFE (H I) intact. Variations in the CO $J =$

2 → 1/1 → 0 line ratio (Appendix A) will manifest as changes in $X_{\rm CO}$.

$\sigma_{\rm gas}$: We adopt $\sigma_{\rm gas} = 11$ km s^{-1} based on the THINGS second moment maps (Appendix B). This is almost twice the commonly used $\sigma_{\rm gas} = 6$ km s^{-1} (Kennicutt 1989, 1998a; Martin & Kennicutt 2001; Boissier et al. 2003) and also higher than $\sigma_{\rm gas} = 8$ km s^{-1}, adopted by Blitz & Rosolowsky (2006). We emphasize the importance of $\sigma_{\rm gas}$ to the stability analysis in §4.3.1; observations with velocity and spatial resolution capable of distenangling different H I components and a multi–phase analysis are needed to move forward on this topic.

σ_*: We assume an isothermal stellar disk with a fixed scale height, as do Boissier et al. (2003) and Blitz & Rosolowsky (2006). Wong & Blitz (2002) and Yang et al. (2007) assume a fixed stellar velocity dispersion. This has a moderate effect on $P_{\rm h}$ and a strong effect on $Q_{\rm stars+gas}$ (§4.3.2).

$\Upsilon_\star^K$: We adopt $\Upsilon_\star^K = 0.5 M_\odot / L_{\odot,K}$ (Appendix C), consistent with our adopted IMF and Bell et al. (2003), the same value used by Blitz & Rosolowsky (2004, 2006). $\Upsilon_\star^K$ directly affects Σ_*, $P_{\rm h}$, $\tau_{\rm ff}$, and $Q_{\rm stars+gas}$. It may vary by $\sim 30\%$ both within and among galaxies (Bell & de Jong 2001), with larger variations in the bluest galaxies or from changes to the assumed IMF (Bell et al. 2003).

Star formation rate tracer: We use FUV+24μm to estimate recent $\Sigma_{\rm SFR}$, discussed in detail in Appendix D. This is similar to Boissier et al. (2007) but in contrast to Kennicutt (1989), Kennicutt (1998a), Martin & Kennicutt (2001), Wong & Blitz (2002), and Boissier et al. (2003), who each used Hα emission with various extinction corrections. Boissier et al. (2007) considered differences between between Hα and FUV profiles in detail, suggesting that stochasticity leads Hα to show signs of knees and turnoffs while FUV remains smooth. We work pixel–by–pixel and in radial profile (similar to Martin & Kennicutt 2001; Wong & Blitz 2002; Boissier et al. 2003; Blitz & Rosolowsky 2006) rather than attempting to isolate individual star forming regions (e.g., Kennicutt et al. 2007). Both differences mean that we measure "recent" rather than "present" $\Sigma_{\rm SFR}$, which may account for some of the smoothness in the trends seen in §4.

6. STAR FORMATION RECIPES

As a final exercise, we compare our galaxies to simple star formation recipes based on the laws and thresholds discussed in §2 and normalized to the H I–to–H$_2$ transition in spirals (§5.2). We predict the SFE in this way:

1. We assume SFE (H$_2$)= 5.25×10^{-10} yr^{-1}
2. We calculate $R_{\rm mol} = \Sigma_{\rm H2}/\Sigma_{\rm HI}$ either:
   (a) By setting $R_{\rm mol} = \tau_{\rm ff,0}/\tau_{\rm ff}$ or $\tau_{\rm orb,0}/\tau_{\rm orb}$.
   (b) From our fits of $R_{\rm mol}$ to radius, Σ_*, $P_{\rm h}$, and $\tau_{\rm orb}$ in spirals galaxies (Equation 32).
3. We derive $\Sigma_{\rm SFR}$ from SFE (H$_2$), $R_{\rm mol}$, and $\Sigma_{\rm HI}$.
4. We calculate the predicted SFE, dividing $\Sigma_{\rm SFR}$ by $\Sigma_{\rm gas}$ in spirals and $\Sigma_{\rm HI}$ in dwarf galaxies.
5. We combine $R_{\rm mol} \propto \tau_{\rm ff}^{-1}$ or $\tau_{\rm orb}^{-1}$ with thresholds. In subcritical areas, we set SFE $= 5 \times 10^{-11}$ yr^{-1}, roughly the observed value at r_{25} in both subsamples.

Figure 18 illustrates the procedure for $R_{\rm mol} \propto \tau_{\rm ff}^{-1}$ and the $Q_{\rm stars+gas}$ threshold in the spiral galaxy NGC 3184.

We set $\tau_{\rm ff,0}$ and $\tau_{\rm orb,0}$ equal to the timescale at the H I–to–H$_2$ transition in spirals (§5.2, Table 5), i.e., we predict $R_{\rm mol}$ using the dotted lines in Figure 16. The predictions will therefore intersect our data where $R_{\rm mol} = \Sigma_{\rm H2}/\Sigma_{\rm HI} \approx 1$ in spirals.

We adopt the same approach to normalize thresholds. For shear and $Q_{\rm stars+gas}$, we define the boundary between supercritical and subcritical data as 2.3 and 1.6, respectively, approximately the values at the H I–to–H$_2$ transition in spirals. For the Schaye (2004) cold phase threshold we use a critical value of 1.

We implement thresholds pixel–by–pixel and present our results in radial average. Within a tilted ring, some lines of sight can be supercritical and some can be subcritical, allowing the threshold to damp the average SFE in a ring without setting it to the minimum value.

The choice to normalize the recipes for both dwarf and spiral galaxies using values measured for spirals is meant to highlight differences between the subsamples.

6.1. *Results*

Figure 19 shows the results of these calculations. The observed SFE as a function of radius appears as a shaded gray region (based on Figure 1). Radial profiles of SFE compiled from predictions appear in color (these follow the same methodology used to make the bins in Figure 1). The top row shows results for spiral (*left*) and dwarf (*right*) galaxies setting $R_{\rm mol} \propto \tau_{\rm ff}^{-1}$ combined with several thresholds, the middle row shows results for $R_{\rm mol} \propto \tau_{\rm orb}^{-1}$ combined with the same stable of thresholds, and the bottom row shows $R_{\rm mol}$ set by fits to radius, Σ_*, $P_{\rm h}$, and $\tau_{\rm orb}$.

Figure 19 illustrates much of what we saw in §4 and 5. First, adopting fixed SFE (H$_2$) ensures that we match the observed SFE with reasonable accuracy in the inner parts of spirals regardless of how we predict $R_{\rm mol}$. Using fits to predict $R_{\rm mol}$ (bottom row) offers a small refinement over the timescales in this regime, but as long as $R_{\rm mol} \gtrsim 1$ then SFE $\sim$ SFE (H$_2$). As a result, the available gas reservoir sets the SFR in this regime.

Setting $R_{\rm mol} \propto \tau_{\rm ff}^{-1}$ or $\tau_{\rm orb}^{-1}$ smoothly damps the SFE with increasing radius, but not by enough to match observations. Without a threshold, $\tau_{\rm ff}$ and $\tau_{\rm orb}$ overpredict the SFE at large radii in spiral galaxies and at $r \gtrsim 0.4\, r_{25}$ in dwarf galaxies (black bins, top two rows).

Thresholds damp the SFE with mixed success (green, magenta, and blue bins in the top two panels). Each somewhat lowers the SFE in the outer parts of galaxies. In the process, however, both $Q_{\rm stars+gas}$ and shear predict suppressed star formation at low or intermediate radii in both dwarf and spiral galaxies, areas where we observe ongoing star formation (the vertical error bars show that the 50% range includes completely subcritical galaxies in both cases). We saw in §4.3 that the radial variation in these thresholds is often less than the scatter among galaxies at a given radius and that the step function behavior that we implement here is not clear in our data.

The Schaye (2004) threshold predicts that a cold phase

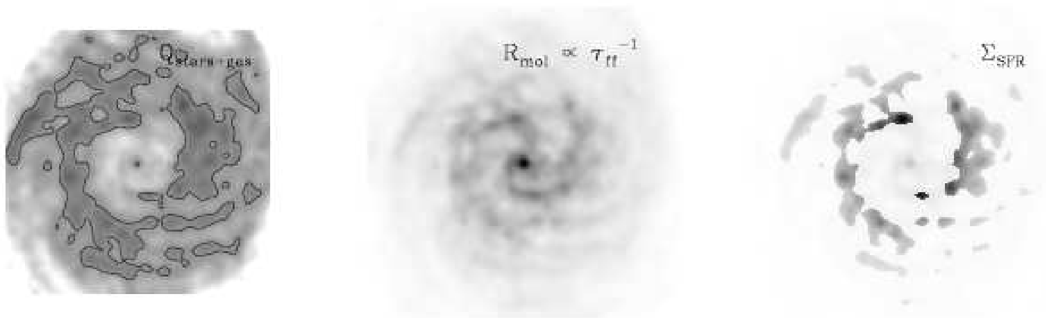

FIG. 18.— How we predict $\Sigma_{\rm SFR}$, illustrated for NGC 3184. We calculate the threshold value (*left*, here $Q_{\rm stars+gas}$), identify supercritical areas (solid contour). In parallel, we estimate $R_{\rm mol} = \Sigma_{\rm H2}/\Sigma_{\rm HI}$ (*middle*), here from $R_{\rm mol} \propto \tau_{\rm ff}^{-1}$. We combine these with the assumption of a fixed SFE (H_2) and a (fixed) low SFE in subcritical areas to predict $\Sigma_{\rm SFR}$ (*right*).

can form almost everywhere in our sample and so only comes into play in the outer parts of spirals and in dwarf galaxies, where it damps the predicted SFE, but not by enough to match observations.

The bottom left panel shows that the fits mostly do a good job of reproducing the SFE in spirals, which is expected because they are fits to these data.

The same fits (to spirals) yield mixed results when applied to dwarf galaxies. The fits to Σ_* and $\tau_{\rm orb}$ show very large scatter and fits to radius, $P_{\rm h}$, and $\tau_{\rm orb}$ all overpredict SFE by varying amounts (similar discrepancies are evident comparing spirals and dwarfs in the top two panels). The scaling relations relating $R_{\rm mol}$ to environment in spirals apparently do not apply perfectly to dwarfs. Likely drivers for the discrepancy are the lower abundance of metals and dust and more intense radiation fields, which affect phase balance in the ISM and the rate of H_2 formation and destruction. Focusing on the pressure fit (green), we can phrase the observation this way: for the same pressure (density), cloud formation in our dwarf subsample is suppressed relative to that in spirals by a factor of ~ 2.

7. SUMMARY

We combine THINGS, SINGS, the GALEX NGS, HERACLES, and BIMA SONG to study what sets the star formation efficiency in 12 nearby spirals and 11 nearby dwarf galaxies.

We use these data to estimate the star formation rate surface density, gas kinematics, and the mass surface densities of H I, H_2, and stars (Appendices A and C). To trace recent star formation, we use a linear combination of GALEX FUV and *Spitzer* 24μm (Appendix D). We suggest that this combination represent a useful tool given the outstanding legacy data sets now available from these two observatories (e.g., SINGS and the GALEX NGS).

We focus on the star formation efficiency (SFE), $\Sigma_{\rm SFR}/\Sigma_{\rm gas}$, and the H_2-to-H I ratio, $R_{\rm mol}$. These quantities remove the basic scaling between gas and SFR, allowing us to focus on where gas forms stars quickly/efficiently (SFE) and the phase of the neutral ISM ($R_{\rm mol}$). We measure the SFE out to $\sim 1.2\ r_{25}$, compare it to a series of variables posited to influence star formation, and test the ability of several predictions to reproduce the observed SFE.

7.1. *Structure of Our Typical Spiral and Dwarf Galaxy*

We deliberately avoid discussing individual galaxies in the main text (these data appear in Appendices E and F). Instead, we study "stacked" versions of a spiral and dwarf galaxy. We sketch their basic structure here.

The spiral galaxy has a roughly constant distribution of H I, $\Sigma_{\rm HI} \sim 6$ M$_\odot$ pc^{-2} out to $\sim r_{25}$. H I surface densities seldom exceed $\Sigma_{\rm HI} \sim 10$ M$_\odot$ pc^{-2}; gas in excess of this surface density tends to be molecular. We observe no analogous saturation in $\Sigma_{\rm H2}$, finding $\Sigma_{\rm H2} \gtrsim 100$ M$_\odot$ pc^{-2} in the very central parts of many galaxies.

Molecular gas, star formation, and stellar surface density all decline with nearly equal exponential scale lengths, $\sim 0.2\ r_{25}$, giving the appearance of a long–lived star–forming disk embedded in a sea of H I. The ISM is mostly H_2 within $\sim 0.5\ r_{25}$ and where $\Sigma_* \gtrsim 80$ M$_\odot$.

Over a wide range of conditions the SFR per unit H_2, SFE (H_2), $= 5.25 \pm 2.5 \times 10^{-10}$ yr^{-1} at scales of 800 pc. This is a "limiting efficiency" in the sense that we do not observe the average SFE in spirals to climb above this value. Where the ISM is mostly H I, the SFE is lower than this limiting value and declines radially with an exponential scale length ~ 0.2–$0.25\ r_{25}$. In this regime, the star formation rate per unit stellar mass remains nearly fixed at a value about twice the cosmologically average rate (i.e., the stellar assembly time is $\sim$ twice the Hubble time).

Dwarf galaxies also exhibit flat H I distributions, declining SFE with increasing radius, and a nearly constant stellar assembly time. Normalized to r_{25}, the scale length of the decline in the SFE is identical to that observed in spirals within the uncertainties. The stellar assembly time is half that found in spirals, corresponding to roughly a Hubble time. Dwarfs exhibit only the crudest relationship between $\Sigma_{\rm SFR}$ and $\Sigma_{\rm HI}$ and, as a result, Σ_* is a much better predictor of the SFR than $\Sigma_{\rm gas}$ (in good agreement with Hunter et al. 1998a). The lack of a clear relationship between $\Sigma_{\rm SFR}$ and $\Sigma_{\rm gas}$ is at least partially due to an incomplete census of the ISM: conditions in the central parts of dwarf galaxies often match those where we find H_2 in spirals and in these same regions the SFE is (unexpectedly) higher than we observe anywhere in spirals (where H_2 is included).

7.2. *Conclusions for Specific Laws and Thresholds*

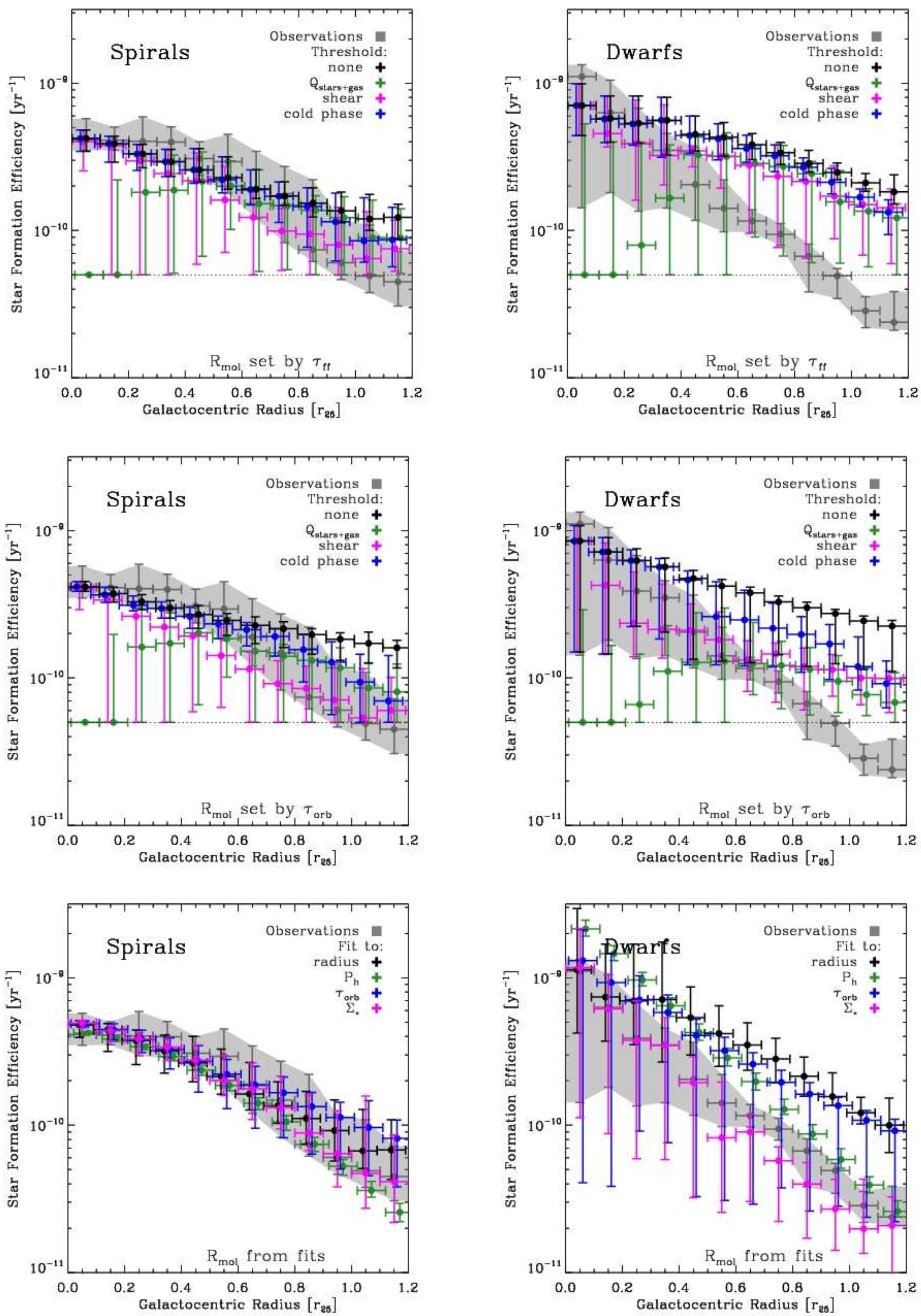

FIG. 19.— Comparison of predicted (color bins) to observed (gray region) SFE in spiral (*left*) and dwarf (*right*) galaxies. We adopt fixed SFE (H_2) and predict $R_{\rm mol}$ from $\tau_{\rm ff}^{-1}$ (*top row*) and $\tau_{\rm orb}^{-1}$ (*middle panel*) combined with thresholds. We also show four fits of $R_{\rm mol}$ to other quantities in spirals (*bottom row*). The dotted horizontal line in the top two rows shows the SFE that we adopt for subcritical data.

We compare the observed SFE to proposed star formation laws and thresholds described in §2. For star formation laws we find:

- The SFE varies dramatically over a small range of $\Sigma_{\rm HI}$ and very little with changing $\Sigma_{\rm H2}$. Therefore, the *disk free-fall time for a fixed scale height disk* or any other weak dependence of SFE on $\Sigma_{\rm gas}$ is of little use to predict the SFE (§4.2.1).

- *The disk free-fall time accounting for a changing scale height*, $\tau_{\rm ff}$, correlates with both SFE and $R_{\rm mol}$ (§4.2.2). Setting SFE proportional to $\tau_{\rm ff}$ broadly captures the drop in SFE in spirals, but predicts variations in SFE (H_2) that we do not observe and is a poor match to dwarf galaxies. Taking $\tau_{\rm ff}$ to be the relevant timescale for H I to form GMCs (i.e., $R_{\rm mol} \propto \tau_{\rm ff}^{-1}$), fails to capture the full drop in the SFE in either subsample.

- The *orbital timescale*, $\tau_{\rm orb}$, also correlates with both SFE and $R_{\rm mol}$, but in outer spirals and dwarf galaxies both SFE and $R_{\rm mol}$ drop faster than $\tau_{\rm orb}$ increases (§4.2.3). As with $\tau_{\rm ff}$, $\tau_{\rm orb}$ alone cannot describe cloud or star formation in our sample.

- In spirals, we observe no clear relationship between SFE (H_2) and the logarithmic derivative of the rotation curve, β (§4.2.3). In dwarf galaxies, SFE correlates with β. Both observations are contrary to the anti-correlation between SFE and β expected if *cloud–cloud collisions* set the SFE (Tan 2000).

- *Fixed GMC efficiency* appears to be a good description of our spiral subsample (§4.1 and Bigiel et al. 2008). SFE (H_2) is constant as a function of a range of environmental parameters. This observation applies only to the disks of spiral galaxies, not starbursts or low metallicity dwarf galaxies.

- We observe a correspondence between hydrostatic *pressure and ISM phase* (§4.2.2 and §5.4.4). In spirals our results are consistent with previous work (Wong & Blitz 2002; Blitz & Rosolowsky 2006). In dwarf galaxies and the outer parts of spirals, inferring $R_{\rm mol}$ from SFE (H I) yields results roughly consistent with predictions by Elmegreen (1993).

For thresholds we find:

- Despite a suggestion of increased stability at large radii in spirals, there is no clear relation between $Q_{\rm gas}$ — which measures stability against axisymmetric collapse due to *self-gravity in the gas disk alone* — and SFE. Most regions are quite stable and $Q_{\rm gas}$ has large scatter, even appearing weakly *anti*–correlated with the SFE in dwarfs (§4.3.1).

- When the effects of stars are included, most disks are only marginally stable: $Q_{\rm stars+gas}$ (Rafikov 2001), which measures *gravitational instability in a disk of gas and stars*, lies mostly in the narrow range 1.3–2.5, increasing slightly towards the centers and edges of galaxies. We emphasize that adopted parameters — $X_{\rm CO}$, $\sigma_{\rm gas}$, $\Upsilon_\star^K$, and σ_* — strongly affect both $Q_{\rm gas}$ and $Q_{\rm stars+gas}$ (§4.3.2).

- The ability of instabilities to survive *competition with shear* (Hunter et al. 1998a) shows the same large scatter and high stability as $Q_{\rm gas}$ in the outer disks of spirals, but identifies most areas in dwarf galaxies and inner spirals as only marginally stable, an improvement over $Q_{\rm gas}$ (§4.3.3).

- Most areas in both dwarf and spiral galaxies meets the condition needed *for a cold phase to form* (§4.3.4) (Schaye 2004). Regions that do not meet this criterion tend to come from outer disks and have low SFE. Because this criterion is met over such a large area, it is of little use on its own to predict variation in the SFE within galaxy disks.

Finally, we distinguish three different *critical surface densities*. First, in spirals $\Sigma_{\rm gas} \sim 14$ M$_\odot$ pc^{-2} at the H I-to-H_2 transition. We find no evidence that this is a real threshold for cloud formation: $R_{\rm mol} = \Sigma_{\rm H2}/\Sigma_{\rm HI}$ varies continuously across $R_{\rm mol} = 1$ as a function of other quantities. However, it is useful to predict the SFE, which will be nearly constant above this $\Sigma_{\rm gas}$. A related (but not identical) value, $\Sigma_{\rm HI} \sim 10$ M$_\odot$ pc^{-2}, is the surface density at which H I "saturates." Gas in excess of this surface density is in the molecular phase (Martin & Kennicutt 2001; Wong & Blitz 2002; Bigiel et al. 2008). This presumably drives the observation that most vigorous star formation takes place where $\Sigma_{\rm HI} \gtrsim 10$ M$_\odot$ pc^{-2} (e.g., Skillman 1987). Last, lower values, $\Sigma_{\rm gas} \sim$ 3–4 M$_\odot$ pc^{-2} (e.g. Kennicutt 1989; Schaye 2004), may correspond to the edge of the star–forming disk. At our resolution such values are relatively rare inside 1.2 r_{25} and we draw no conclusion regarding whether this "outer disk threshold" corresponds to a real shift in the mode of star formation.

7.3. *General Conclusions*

Our general conclusions are:

1. In the disks of spiral galaxies, the SFE of H_2 is roughly constant as a function of: galactocentric radius, Σ_*, $\Sigma_{\rm gas}$, $P_{\rm h}$, $\tau_{\rm orb}$, $Q_{\rm gas}$, and β (§5.1). This fixed SFE (H_2)= $5.25 \pm 2.5 \times 10^{-10}$ yr^{-1} ($\tau_{\rm Dep}$(H2) $= 1.9 \times 10^9$ yr) sets the SFE of total gas across the H_2–dominated inner parts ($r_{\rm gal} \lesssim 0.5\ r_{25}$) of spiral galaxies.

2. In spiral galaxies, the transition between a mostly–H I and a mostly–H_2 ISM is a well–defined function of local conditions (§5.2). It occurs at a characteristic radius ($0.43 \pm 0.18\ r_{25}$), Σ_* (81 ± 25 M$_\odot$ pc^{-2}), $\Sigma_{\rm gas}$ (14 ± 6 M$_\odot$ pc^{-2}), $P_{\rm h}$ ($2.3 \pm 1.5 \times 10^4\ k_{\rm B}$ cm^{-3} K), and $\tau_{\rm orb}$ ($1.8 \pm 0.4 \times 10^8$ yr).

3. We find indirect evidence for abundant H_2 in the central parts of many dwarf galaxies, where SFE (H I) exceeds SFE (H_2) found in spirals. The simplest explanation is that H_2 accounts for a significant fraction of the ISM along these lines of sight (§4.1.1 and §5.3). The implied central $\Sigma_{\rm H2}/\Sigma_{\rm HI}$ is ~ 2.5 with $\Sigma_{\rm H2} = \Sigma_{\rm HI}$ at $\sim 0.25\ r_{25}$.

4. Where $\Sigma_{\rm HI} > \Sigma_{\rm H2}$ — in the outer parts of spirals and throughout dwarf galaxies (by assumption) —

we observe the SFE to decline steadily with increasing radius, with scale length ~ 0.2–$0.25\ r_{25}$ in both subsamples (§4.1). We also observe a decline in SFE with decreasing Σ_*, decreasing $P_{\rm h}$, and increasing $\tau_{\rm orb}$, which are all covariant with radius.

5. Where $\Sigma_{\rm HI} > \Sigma_{\rm H2}$, we find little relation between SFE and $\Sigma_{\rm gas}$ (§4.1.3) but a strong relationship between SFE and Σ_* (§4.1.2). The simplest explanation is that present day star formation roughly follows past star formation. A more aggressive interpretation is that the stellar potential well or feedback are critical to bring gas to high densities.

6. The H_2–to–H I ratio, $R_{\rm mol} = \Sigma_{\rm H2}/\Sigma_{\rm HI}$, and by extension cloud formation, depends strongly on environment. $R_{\rm mol}$ correlates with radius, $P_{\rm h}$, $\tau_{\rm ff}$, $\tau_{\rm orb}$, and Σ_* in spirals. We find corresponding correlations between these quantities and $\Sigma_{\rm SFR}/\Sigma_{\rm HI}$, a proxy for the efficiency of cloud formation in dwarfs and the outer parts of spirals. At our resolution, $R_{\rm mol}$ appears to be a continuous function of environment from the H I–dominated ($R_{\rm mol} \sim 0.1$) to H_2–dominated ($R_{\rm mol} \sim 10$) regime (§5.4).

7. The variation in $R_{\rm mol}$ is too strong to be reproduced only by varying $\tau_{\rm orb}$ or $\tau_{\rm ff}$ (§4.2 and 5.4.1). Physics other than these timescales must also play an important role in cloud formation (points 8 – 11).

8. Thresholds for large scale stability do not offer an obvious way to predict $R_{\rm mol}$. We find no clear relationship (continuous or step–function) between SFE and $Q_{\rm gas}$, $Q_{\rm stars+gas}$, or the shear threshold. The threshold values we find suggest disks that are stable or marginally stable throughout once the effects of stars are included (§4.3 and 5.4.2).

9. We derive a power law relationship between $R_{\rm mol}$ and hydrostatic pressure (Elmegreen 1989) that is roughly consistent with expectations by Elmegreen (1993), observations by Wong & Blitz (2002) and Blitz & Rosolowsky (2006), and simulations by Robertson & Kravtsov (2008). In its simplest form, this is a variation on the classical Schmidt law, i.e., $R_{\rm mol}$ set by gas volume density (§4.2 and 5.4.4).

10. Power law fits of $R_{\rm mol}$ to $P_{\rm h}$ ($\tau_{\rm ff}$), radius, $\tau_{\rm orb}$, and Σ_* reproduce observed SFE reasonably in spiral galaxies but yield large scatter or higher–than–expected SFE in the outer parts of dwarf galaxies, offering indirect evidence that the differences between our two subsamples — metallicity (dust), radiation field, and strong spiral shocks — play a role in setting these relations (§5.4.5 and 6).

11. Our data do not identify a unique driver for the SFE, but suggest that ISM physics below our resolution — balance between warm and cold H I phases, H_2 formation, and perhaps shocks and turbulent fluctuations driven by stellar feedback — govern the ability of the ISM to form GMCs out of marginally stable galaxy disks (§5.4.5).

We thank the anonymous referee for helpful suggestions that improved the paper. We thank Daniela Calzetti, Robert Kennicutt, Erik Rosolowsky, Tony Wong, Leo Blitz, and Helene Roussel for suggestions and discussion during this project. We gratefully acknowledge the hard work of the SINGS, GALEX NGS, and BIMA SONG teams and thank them for making their data publicly available. EB gratefully acknowledges financial support through an EU Marie Curie International Reintegration Grant (Contract No. MIRG-CT-6-2005-013556). FB acknowledges support from the Deutsche Forschungsgemeinschaft (DFG) Priority Program 1177. The work of WJGdB is based upon research supported by the South African Research Chairs Initiative of the Department of Science and Technology and National Research Foundation. We have made use of: the NASA/IPAC Extragalactic Database (NED) which is operated by the Jet Propulsion Laboratory, California Institute of Technology, under contract with the National Aeronautics and Space Administration; the HyperLeda catalog, located on the World Wide Web at http://www-obs.univ-lyon1.fr/hypercat/intro.html; NASA's Astrophysics Data System (ADS); and data products from the Two Micron All Sky Survey, which is a joint project of the University of Massachusetts and the Infrared Processing and Analysis Center/California Institute of Technology, funded by the National Aeronautics and Space Administration and the National Science Foundation.

REFERENCES

Bell, E. F., & de Jong, R. S. 2001, ApJ, 550, 212
Bell, E. F., McIntosh, D. H., Katz, N., & Weinberg, M. D. 2003, ApJS, 149, 289
Bell, E. F. 2003, ApJ, 586, 794
Bianchi, L., et al. 2005, ApJ, 619, L71
Bigiel, F., Leroy, A., Walter, F., Brinks, E., de Blok, W.J.H., Madore, .B, & Thornley, M., AJ submitted
Binney, J., & Merrifield, M. 1998, Galactic astronomy / James Binney and Michael Merrifield. Princeton, NJ : Princeton University Press, 1998. (Princeton series in astrophysics)
Blitz, L. 1993, Protostars and Planets III, 125
Blitz, L., & Rosolowsky, E. 2004, ApJ, 612, L29
Blitz, L., Fukui, Y., Kawamura, A., Leroy, A., Mizuno, N., & Rosolowsky, E. 2007, Protostars and Planets V, 81
Blitz, L., & Rosolowsky, E. 2006, ApJ, 650, 933
Bohlin, R. C., Savage, B. D., & Drake, J. F. 1978, ApJ, 224, 132
Bolatto, A. et al., ApJ submitted
Boissier, S., Prantzos, N., Boselli, A., & Gavazzi, G. 2003, MNRAS, 346, 1215
Boissier, S., et al. 2007, ApJS, 173, 524
Bottema, R. 1993, A&A, 275, 16
Braine, J., Combes, F., Casoli, F., Dupraz, C., Gerin, M., Klein, U., Wielebinski, R., & Brouillet, N. 1993, A&AS, 97, 887
Braun, R. 1997, ApJ, 484, 637
Buat, V., & Xu, C. 1996, A&A, 306, 61
Buat, V., Boselli, A., Gavazzi, G., & Bonfanti, C. 2002, A&A, 383, 801
Calzetti, D., Kinney, A. L., & Storchi-Bergmann, T. 1994, ApJ, 429, 582
Calzetti, D., Bohlin, R. C., Kinney, A. L., Storchi-Bergmann, T., & Heckman, T. M. 1995, ApJ, 443, 136
Calzetti, D., et al. 2005, ApJ, 633, 871
Calzetti, D., et al. 2007, ApJ, 666, 870
Cardelli, J. A., Clayton, G. C., & Mathis, J. S. 1989, ApJ, 345, 245
Chabrier, G. 2003, PASP, 115, 763
Ciardullo, R., Durrell, P. R., Laychak, M. B., Herrmann, K. A., Moody, K., Jacoby, G. H., & Feldmeier, J. J. 2004, ApJ, 614, 167

Cortese, L., et al. 2006, ApJ, 637, 242
Crosthwaite, L., & Turner, J. 2007, ArXiv e-prints, 707, arXiv:0707.2636
Daigle, O., Carignan, C., Amram, P., Hernandez, O., Chemin, L., Balkowski, C., & Kennicutt, R. 2006, MNRAS, 367, 469
Dalcanton, J. J., Yoachim, P., & Bernstein, R. A. 2004, ApJ, 608, 189
Dale, D. A., & Helou, G. 2002, ApJ, 576, 159
Dale, D. A., et al. 2007, ApJ, 655, 863
Dame, T. M., Hartmann, D., & Thaddeus, P. 2001, ApJ, 547, 792
Dib, S., Bell, E., & Burkert, A. 2006, ApJ, 638, 797
de Blok, W. J. G., & Walter, F. 2006, AJ, 131, 363
de Blok, E., et al., AJ submitted
Draine, B. T., et al. 2007, ApJ, 663, 866
Elmegreen, B. G. 1989, ApJ, 338, 178
Elmegreen, B. G. 1993, ApJ, 411, 170
Elmegreen, B. G., & Parravano, A. 1994, ApJ, 435, L121
Elmegreen, B. G. 1997, Revista Mexicana de Astronomia y Astrofisica Conference Series, 6, 165
Engargiola, G., Plambeck, R. L., Rosolowsky, E., & Blitz, L. 2003, ApJS, 149, 343
Fazio, G. G., et al. 2004, ApJS, 154, 10
Fukui, Y., et al. 1999, PASJ, 51, 745
Gil de Paz, A., et al. 2007, ApJS, 173, 185
Gordon, K. D., et al. 2005, PASP, 117, 503
Helfer, T. T., Thornley, M. D., Regan, M. W., Wong, T., Sheth, K., Vogel, S. N., Blitz, L., & Bock, D. C.-J. 2003, ApJS, 145, 259
Helou, G., et al. 2004, ApJS, 154, 253
Heyer, M. H., Corbelli, E., Schneider, S. E., & Young, J. S. 2004, ApJ, 602, 723
Hunter, D. A., Elmegreen, B. G., & Baker, A. L. 1998, ApJ, 493, 595
Hunter, D. A., Wilcots, E. M., van Woerden, H., Gallagher, J. S., & Kohle, S. 1998, ApJ, 495, L47
Jarrett, T. H., Chester, T., Cutri, R., Schneider, S. E., & Huchra, J. P. 2003, AJ, 125, 525
Jog, C. J., & Solomon, P. M. 1984, ApJ, 276, 127
Johnson, B. D., et al. 2007, ApJS, 173, 392
Kauffmann, G., et al. 2003, MNRAS, 341, 54
Kennicutt, R. C. 1989, ApJ, 344, 685
Kennicutt, R. C. 1998, ApJ, 498, 541
Kennicutt, R. C., Jr. 1998, ARA&A, 36, 189
Kennicutt, R. C., Jr., et al. 2003, PASP, 115, 928
Kennicutt, R. C., Jr., et al. 2007, ArXiv e-prints, 708, arXiv:0708.0922
Kim, W.-T., & Ostriker, E. C. 2001, ApJ, 559, 70
Kim, W.-T., & Ostriker, E. C. 2007, ApJ, 660, 1232
Kregel, M., van der Kruit, P. C., & de Grijs, R. 2002, MNRAS, 334, 646
Kregel, M., & van der Kruit, P. C. 2005, MNRAS, 358, 481
Kroupa, P. 2001, MNRAS, 322, 231
Krumholz, M. R., & McKee, C. F. 2005, ApJ, 630, 250
Krumholz, M. R., & Thompson, T. A. 2007, ArXiv e-prints, 704, arXiv:0704.0792
Lee, J. C. 2006, Ph.D. Thesis
Lequeux, J., Maucherat-Joubert, M., Deharveng, J. M., & Kunth, D. 1981, A&A, 103, 305
Leroy, A., Bolatto, A. D., Simon, J. D., & Blitz, L. 2005, ApJ, 625, 763
Leroy, A. K., Walter, F., Bigiel, F., Usero A., Weiss A., Brinks, E., de Blok, W.J.G., Kennicutt R. C., Schuster, K., Wiesemeyer H., Kramer, C., Roussel, H., 2008, AJ submitted
Leitherer, C., et al. 1999, ApJS, 123, 3
Li, Y., Mac Low, M.-M., & Klessen, R. S. 2005, ApJ, 626, 823
Li, Y., Mac Low, M.-M., & Klessen, R. S. 2006, ApJ, 639, 879
Lupton, R. H., Gunn, J. E., & Szalay, A. S. 1999, AJ, 118, 1406
Madore, B. F. 1977, MNRAS, 178, 1
Martin, C. L., & Kennicutt, R. C., Jr. 2001, ApJ, 555, 301
Martin, D. C., et al. 2005, ApJ, 619, L1
McKee, C. F., & Ostriker, J. P. 1977, ApJ, 218, 148
McKee, C. F., & Ostriker, E. C. 2007, ARA&A, 45, 565
Melisse, J. P. M., & Israel, F. P. 1994, A&AS, 103, 391
Merrett, H. R., et al. 2006, MNRAS, 369, 120
Moustakas, J., & Kennicutt, R. C., Jr. 2006, ApJ, 651, 155
Murgia, M., Crapsi, A., Moscadelli, L., & Gregorini, L. 2002, A&A, 385, 412
Pahre, M. A., Ashby, M. L. N., Fazio, G. G., & Willner, S. P. 2004, ApJS, 154, 235
de Grijs, R., & Peletier, R. F. 1997, A&A, 320, L21
Prugniel, P., & Heraudeau, P. 1998, A&AS, 128, 299
Pérez-González, P. G., et al. 2006, ApJ, 648, 987
Oh, S.-H., et al. 2008, in prep.
Ott, J., Walter, F., Brinks, E., Van Dyk, S. D., Dirsch, B., & Klein, U. 2001, AJ, 122, 3070
Quirk, W. J. 1972, ApJ, 176, L9
Rafikov, R. R. 2001, MNRAS, 323, 445
Regan, M. W., Thornley, M. D., Helfer, T. T., Sheth, K., Wong, T., Vogel, S. N., Blitz, L., & Bock, D. C.-J. 2001, ApJ, 561, 218
Riechers, D. A., Walter, F., Carilli, C. L., & Bertoldi, F. 2007, ApJ, 671, L13
Rieke, G. H., et al. 2004, ApJS, 154, 25
Robertson, B. E., & Kravtsov, A. V. 2008, ApJ, 680, 1083
Rosolowsky, E., Engargiola, G., Plambeck, R., & Blitz, L. 2003, ApJ, 599, 258
Rosolowsky, E. 2005, PASP, 117, 1403
Rosolowsky, E. 2007, ApJ, 654, 240
Roussel, H., Gil de Paz, A., Seibert, M., Helou, G., Madore, B. F., & Martin, C. 2005, ApJ, 632, 227
Salim, S., et al. 2007, ArXiv e-prints, 704, arXiv:0704.3611
Salpeter, E. E. 1955, ApJ, 121, 161
Sawada, T., et al. 2001, ApJS, 136, 189
Schlegel, D. J., Finkbeiner, D. P., & Davis, M. 1998, ApJ, 500, 525
Schaye, J. 2004, ApJ, 609, 667
Schuster, K.-F., et al. 2004, A&A, 423, 1171
Schmidt, M. 1959, ApJ, 129, 243
Schmidt, M. 1963, ApJ, 137, 758
Schuster, K. F., Kramer, C., Hitschfeld, M., Garcia-Burillo, S., & Mookerjea, B. 2007, A&A, 461, 143
Shapiro, K. L., Gerssen, J., & van der Marel, R. P. 2003, AJ, 126, 2707
Silk, J. 1997, ApJ, 481, 703
Simon, J. D., Bolatto, A. D., Leroy, A., Blitz, L., & Gates, E. L. 2005, ApJ, 621, 757
Skillman, E. D. 1987, Star Formation in Galaxies, 263
Spitzer, L. 1978, New York Wiley-Interscience, 1978. 333 p.
Springel, V., & Hernquist, L. 2003, MNRAS, 339, 289
Solomon, P. M., Rivolo, A. R., Barrett, J., & Yahil, A. 1987, ApJ, 319, 730
Strong, A. W., & Mattox, J. R. 1996, A&A, 308, L21
Tamburro, D., et al., AJ in press
Tan, J. C. 2000, ApJ, 536, 173
Taylor, C. L., Kobulnicky, H. A., & Skillman, E. D. 1998, AJ, 116, 2746
Temi, P., Brighenti, F., & Mathews, W. G. 2005, ApJ, 635, L25
Thilker, D. A., et al. 2005, ApJ, 619, L79
Thilker, D. A., et al. 2005, ApJ, 619, L67
Thornley, M. D., Braine, J., & Gardan, E. 2006, ApJ, 651, L101
Toomre, A. 1964, ApJ, 139, 1217
Trachternach, C., et al. 2008, in prep.
Usero, A., et al. 2008, submitted
van der Kruit, P. C., & Searle, L. 1981, A&A, 95, 105
van der Kruit, P. C. 1988, A&A, 192, 117
Walter, F., Taylor, C. L., Hüttemeister, S., Scoville, N., & McIntyre, V. 2001, AJ, 121, 727
Walter, F., Weiss, A., Martin, C., & Scoville, N. 2002, AJ, 123, 225
Walter, F., et al. 2007, ApJ, 661, 102
Walter et al., 2008, AJ submitted
Wilson, B. A., Dame, T. M., Masheder, M. R. W., & Thaddeus, P. 2005, A&A, 430, 523
Wong, T., & Blitz, L. 2002, ApJ, 569, 157
Wolfire, M. G., Hollenbach, D., & Tielens, A. G. G. M. 1993, ApJ, 402, 195
Wolfire, M. G., McKee, C. F., Hollenbach, D., & Tielens, A. G. G. M. 2003, ApJ, 587, 278
Wyder, T. K., et al. 2007, ApJS, 173, 293
Yang, C.-C., Gruendl, R. A., Chu, Y.-H., Mac Low, M.-M., & Fukui, Y. 2007, ArXiv e-prints, 708, arXiv:0708.3243
Young, J. S. & Scoville, N. Z. 1991, ARA&A, 29, 581
Young, J. S., et al. 1995, ApJS, 98, 219
Young, L. M., van Zee, L., Lo, K. Y., Dohm-Palmer, R. C., & Beierle, M. E. 2003, ApJ, 592, 111

APPENDIX

These appendices describe how we assemble the database of radial profiles and maps that are used in the main text. We discuss the data and methods that we use to derive gas surface densities (Appendix A), kinematics (Appendix B), stellar surface densities (Appendix C), and star formation rate surface densities (Appendix D). Finally, we present a table containing radial profiles of key quantities (Appendix E) and an atlas showing maps, profiles, and basic results for each galaxy (Appendix F) .

MAPS OF H I AND H_2 SURFACE DENSITY

$\Sigma_{\rm HI}$ *from THINGS 21cm Maps*

The H I Nearby Galaxy Survey (THINGS, Walter et al. 2008) mapped 21-cm line emission from all of our sample galaxies using the Very Large Array. We calculate atomic gas mass surface density, $\Sigma_{\rm HI}$, from natural-weighted data that have mean angular resolution $11''$ and mean velocity resolution 5 km s^{-1}. THINGS includes data from the most compact VLA configuration and therefore comfortably recovers extended structure (up to $15'$) in our sources. At $30''$ resolution, THINGS maps are sensitive to $\Sigma_{\rm HI}$ as low as ~ 0.5 M$_\odot$ pc^{-2}; here we adopt a working sensitivity of $\Sigma_{\rm HI} = 1$ M$_\odot$ pc^{-2}. In practice the sensitivity and field of view of the THINGS maps are sufficient to measure $\Sigma_{\rm HI}$ to $\gtrsim r_{25}$ in almost every galaxy. For detailed description and presentation of THINGS, we refer the reader to Walter et al. (2008).

To convert from integrated intensity to $\Sigma_{\rm HI}$ we use

$$\Sigma_{\rm HI}\ \left[{\rm M_\odot\ pc^{-2}}\right] = 0.020\ \cos i\ I_{\rm 21cm}\ \left[{\rm K\ km\ s^{-1}}\right]\ . \tag{A1}$$

which accounts for inclination and includes a factor of 1.36 to reflect the presence of helium.

$\Sigma_{\rm H2}$ *from HERACLES (IRAM 30-m) and BIMA SONG CO Maps*

We estimate the surface density of molecular hydrogen, $\Sigma_{\rm H2}$, from CO emission, the most commonly used tracer of H_2. Along with Bigiel et al. (2008), this study presents the first scientific results from HERACLES, a large project that used the HERA focal plane array (Schuster et al. 2004) on the IRAM 30–m telescope to map CO $J = 2 \rightarrow 1$ emission from the full optical disk in 18 THINGS galaxies (Leroy et al. 2008). These data have an angular resolution of $11''$ and a velocity resolution of 2.6 km s^{-1}. The typical noise in an individual channel map is 40–80 mK, yielding (masked) integrated intensity maps that are sensitive to $\Sigma_{\rm H2} \gtrsim 4$ M$_\odot$ pc^{-2} at our working resolution and adopted conversion factor.

HERA maps are not available for NGC 3627 and NGC 5194. In these galaxies, we use CO $J = 1 \rightarrow 0$ maps from the BIMA Survey of Nearby Galaxies (BIMA SONG, Helfer et al. 2003) to estimate $\Sigma_{\rm H2}$. These data have angular resolution $\sim 7''$ and include zero-spacing data from the Kitt Peak 12m, ensuring sensitivity to extended structure.

We derive $\Sigma_{\rm H2}$ from integrated CO intensity, $I_{\rm CO}$ by adopting a constant CO-to-H_2 conversion factor, $X_{\rm CO} = 2 \times 10^{20}$ cm^{-2} (K km s^{-1})$^{-1}$. Based on comparison to γ-ray and FIR observations, this value is appropriate in the Solar Neighborhood (Strong & Mattox 1996; Dame et al. 2001). For CO $J = 1 \rightarrow 0$ emission, the conversion to $\Sigma_{\rm H2}$ is

$$\Sigma_{\rm H2}\ \left[{\rm M_\odot\ pc^{-2}}\right] = 4.4\ \cos i\ I_{\rm CO}\ \ (1 \rightarrow 0)\ \ \left[{\rm K\ km\ s^{-1}}\right]\ . \tag{A2}$$

To relate CO $J = 2 \rightarrow 1$ to CO $J = 1 \rightarrow 0$ intensity, we further assume a line ratio of $I_{\rm CO}(2 \rightarrow 1) = 0.8\ I_{\rm CO}(1 \rightarrow 0)$. Based on direct comparison of HERACLES and previous surveys, thisis a typical value in our sample (Leroy et al. 2008) and is intermediate in the range ($\sim 0.6 - -1.0$) observed for the Milky Way and other spiral galaxies (, e.g., Braine et al. 1993; Sawada et al. 2001; Schuster et al. 2007). Thus, for the HERACLES maps we derive $\Sigma_{\rm H2}$ via

$$\Sigma_{\rm H2}\ \left[{\rm M_\odot\ pc^{-2}}\right] = 5.5\ \cos i\ I_{\rm CO}\ \ (2 \rightarrow 1)\ \ \left[{\rm K\ km\ s^{-1}}\right]\ . \tag{A3}$$

The CO–to–H_2 *Conversion Factor*

The CO–to–H_2 conversion factor is presumably a source of significant systematic uncertainty in $\Sigma_{\rm H2}$. $X_{\rm CO}$ almost certainly varies: it is likely to be lower than Galactic (yielding lower $\Sigma_{\rm H2}$) in overwhelmingly molecular, heavily excited regions; it is likely to be higher (yielding higher $\Sigma_{\rm H2}$) in regions with low dust content and intense radiation fields, such as dwarf irregular galaxies. There is compelling evidence for both senses of variation, but it is our assessment that no reliable calibration of $X_{\rm CO}$ as a function of metallicity, radiation field, and $\Sigma_{\rm H2}$ yet exists. A useful calibration must reflect all of these quantities, which all affect $X_{\rm CO}$ and are not universally covariant.

In light of this uncertainty, our approach is: 1) to treat $X_{\rm CO}$ as unknown in low mass, low–metallicity galaxies, where different approaches to measure $\Sigma_{\rm H2}$ yield results that differ by an order of magnitude or more and 2) to assume that variations in $X_{\rm CO}$ within spiral galaxies are relatively small. The second point might be expected based on theoretical modeling of GMCs (Wolfire et al. 1993) and the observed uniformity of GMC properties across a wide range of environments (Bolatto et al. 2008). We emphasize that even if present, the most extreme variations are likely to contribute primarily to the central resolution element, which is not the focus of this study, and the far outer disk, where $\Sigma_{\rm H2}$ is not the dominant mass component.

Variations aside, estimates of "typical" values of $X_{\rm CO}$ in the Milky Way and other spiral galaxies span the range ~ 1.5–4×10^{20} cm^{-2} (K km s^{-1})$^{-1}$ (e.g. Blitz et al. 2007; Draine et al. 2007, in addition to the references already

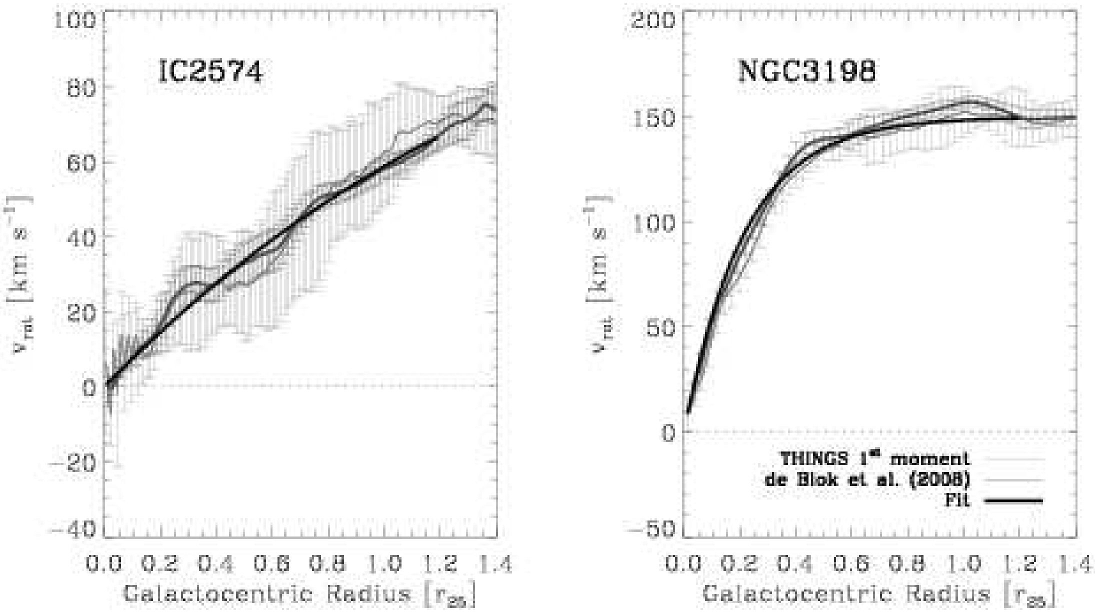

FIG. B1.— Illustration of our rotation curve treatment. Light gray profiles show median rotation velocity and scatter measured directly from the THINGS first moment maps; dark gray profiles and scatter show the higher quality (de Blok et al. 2008) rotation curves. The thick black lines show the fit that we use to approximate the rotation curve. This simple function (Equation B1) does a good job of capturing both the steadily rising rotation curves typical of dwarf galaxies (e.g., IC 2574, left panel) and the rapidly rising then flat curves seen in more massive spiral galaxies (e.g., NGC 3198, right panel).

given). The choice of mean $X_{\rm CO}$ within this range can have a large impact on, e.g., assessing gravitational stability or conditions at the H_2-to-H I transition. We refer the reader to Boissier et al. (2003) for a quantitative exploration of how different assumptions regarding $X_{\rm CO}$ affect a stability analysis.

Masking the H I *and CO Data Cubes*

The H I and CO data cubes have large bandwidth, only a small part of which contains signal of the spectral line. In order to produce integrated intensity maps with good signal-to-noise ratio, we blank signal-free regions of the H I and CO cubes. Walter et al. (2008) describe this process for THINGS. We apply an analogous procedure to the HERACLES and BIMA SONG data. We convolve the cubes to 30″ resolution, identify regions with significant emission, and then blank the original data cubes outside these regions. We integrate these blanked cubes to create intensity maps. For HERACLES, we require $I_{\rm CO} > 2\sigma_{\rm RMS}$ in 3 consecutive (2.6 km s^{-1}) channels at 30″ resolution. Note that our use of masking drives the small ($\sim 10\%$) numerical differences with the HERACLES survey paper (which uses a different approach to create integrated intensity maps). For BIMA SONG, we require either $I_{\rm CO} > 3\sigma_{\rm RMS}$ in a single (10 km s^{-1}) channel at 30″ resolution or $I_{\rm CO} > 2\sigma_{\rm RMS}$ in consecutive velocity channels, similar to the original masking by Helfer et al. (2003). In both cases we consider only CO emission within ~ 100 km s^{-1} of the mean H I velocity.

KINEMATICS

Rotation Curves from THINGS

We approximate all galaxies to have rotation curves with the following functional form (Boissier et al. 2003):

$$v_{\rm rot}\,(r) = v_{\rm flat}\ \left[1 - \exp\left(\frac{-r}{l_{\rm flat}}\right)\right] \tag{B1}$$

where $v_{\rm rot}$ is the circular rotation speed of the galaxy at a radius r and $v_{\rm flat}$ and $l_{\rm flat}$ are free parameters that represent the velocity at which the rotation curve is flat and the length scale over which it approaches this velocity. For a continuously rising rotation curve, common for low–mass galaxies, we expect large $l_{\rm flat}$, while the almost flat rotation curves of massive spiral galaxies will have small $l_{\rm flat}$ and then remain nearly constant at $v_{\rm flat}$.

In most cases, Equation B1 captures the basic behavior of the rotation curve well. Small scale variations are lost, but these may be due to streaming motions near spiral arms or warps in the gas disk as easily as real variations in the circular velocity. On the other hand, Equation B1 offers the distinct advantage of having a smooth, analytic derivative. Our analysis uses the rotation curve to estimate the orbital timescale, shear, and coriolis force (see §2). The former is quite reasonably captured by Equation B1 and the latter two depend critically on the derivative of the rotation curve $\beta = d\log\ v(r_{\rm gal})/d\log\ r_{\rm gal}$.

For each galaxy, we derive $v_{\rm flat}$ and $l_{\rm flat}$ from a non-linear least squares fit using Equation B1 and profiles of $v_{\rm rot}$ measured from the THINGS data cubes. We calculate $v_{\rm rot}$ from the intensity–weighted first moment, $v_{\rm r}$, via

$$v_{\rm rot} = \frac{v_{\rm r} - v_{\rm sys}}{\sin i \ \cos\theta} \ . \quad (B2)$$

Here $v_{\rm sys}$ is the systemic velocity, i is the inclination, and θ is the azimuthal angle relative to the receding major axis measured in the plane of the galaxy. We calculate maps of $v_{\rm rot}$ and then convert these into profiles of the median and 1σ scatter in $v_{\rm rot}$ within 60° of the major axis in a series $5''$–wide tilted rings. We fit Equation B1 to the profile of median $v_{\rm rot}$ weighted by the scatter in that ring.

For many of our galaxies, high quality rotation curves are available from the analysis of de Blok et al. (2008, see Table 2). Wherever possible, we include these in our fit with very high weight, so that they drive the best–fit $v_{\rm flat}$ and $l_{\rm flat}$ for these galaxies. For the 7 low–inclination galaxies in our sample that are not part of the study by de Blok et al. (2008) (see Column 4 of Table 2) we only fit the first moment data.

Figure B1 shows examples of this procedure for two galaxies: the dwarf irregular IC 2574, which has a steadily rising rotation curve, and the spiral galaxy NGC 3198, which has a quickly rising rotation curve that remains flat over most of the disk. We plot $v_{\rm rot}$ and associated scatter, the de Blok et al. (2008) rotation curve, and the best–fit version of Equation B1. The best–fit values of $v_{\rm flat}$ and $l_{\rm flat}$ for all galaxies are given in Table 4; for the three galaxies that overlap the sample of Boissier et al. (2003), we match their fitted parameters well.

The dynamics of the irregular galaxies NGC 3077 and NGC 4449 are not well–described by Equation B1; the former is disturbed by an ongoing interaction with M81 and the latter has a counter–rotating core, perhaps due to a recent interaction (Hunter et al. 1998b). We neglect both galaxies in the kinematic analyses.

Gas Velocity Dispersion

Throughout this paper, we adopt a single gas velocity dispersion, $\sigma_{\rm gas} = 11$ km s^{-1}. This is typical of the outer (H I-dominated) parts of THINGS galaxies and agrees well with values derived by Tamburro et al. (in prep.), who are conducting a thorough study of $\sigma_{\rm gas}$ in THINGS. The left panel in Figure C1 motivates this choice. We plot the median and 1σ range of $\sigma_{\rm gas}$ over the range 0.5 r_{25}–1.0 r_{25} for each galaxy in THINGS as a function of the inclination of the galaxy. We restrict ourselves to the outer disk because over this regime H I usually dominates the ISM. This figure shows that a fixed $\sigma_{\rm gas} = 11 \pm 3$ km s^{-1} is a good description of the outer disk for galaxies with $i < 60^\circ$; variations both within and among galaxies are comparatively small, typically 25%. On the other hand, highly inclined galaxies show large scatter and systematically high velocity dispersions, likely because the velocity dispersion is significantly affected by projection effects.

Variations in the gas velocity dispersion inside 0.5 r_{25} could be expected to take two forms: $\sigma_{\rm gas}$ in the warm neutral medium may increase in regions of active star formation due to stellar feedback (e.g. Dib et al. 2006) and the fraction of gas in a narrow–line width (cold) H I phase may increase towards the centers of galaxies (e.g. Schaye 2004). The first effect may be observed in THINGS: the second moment maps show a gradual increase in $\sigma_{\rm gas}$ from the outskirts to the centers of galaxies. The second effect can, in principle, be observed using 21–cm line observations (de Blok & Walter 2006), but doing so is very challenging, requiring better spatial and velocity resolution and a higher signal–to–noise ratio than is achieved in most THINGS targets. Further, we know that a large fraction of the ISM is H_2 in the central parts of our spiral galaxies, making it even more complicated to interpret measurements based only on H I. Because measuring the detailed behavior of $\sigma_{\rm gas}$ inside ~ 0.5 r_{25} is beyond the limit of our current data, and because $\sigma_{\rm gas}$ varies only gradually in the outer parts of galaxies, we adopt a fixed $\sigma_{\rm gas}$ (an almost universal approach in this field, following Kennicutt 1989; Hunter et al. 1998a; Martin & Kennicutt 2001; Wong & Blitz 2002; Boissier et al. 2003).

Stellar Velocity Dispersion

Direct measurements of the stellar velocity dispersion, σ_*, across the disks of nearby galaxies are extremely scarce. In lieu of such observations for our sample, we make four assumptions to estimate σ_*. First, we assume that the exponential stellar scale height, h_*, of a galaxy does not vary with radius. This is generally observed for edge–on disk galaxies (van der Kruit & Searle 1981; de Grijs & Peletier 1997; Kregel et al. 2002). Second, we assume that h_* is related to the stellar scale length, l_*, by $l_*/h_* = 7.3 \pm 2.2$, the average flattening ratio measured by Kregel et al. (2002). Because we measure l_*, this yields an estimate of h_*. Third, we assume that our disks are isothermal in the z-direction, so that hydrostatic equilibrium yields $h_* = 1/2 \ \left(\sigma_{*,z}^2/2\pi G\rho_*\right)^{0.5}$ (van der Kruit & Searle 1981), where ρ_* is the midplane stellar volume density and $\Sigma_* = 4\rho_* h_*$ (van der Kruit 1988). Eliminating ρ_*, then in terms of measured quantities, $\sigma_{*,z} = \sqrt{2 \ \pi \ G \ \Sigma_* \ h_*}$ (van der Kruit 1988) and

$$\sigma_{*,z} = \sqrt{\frac{2 \ \pi \ G \ l_*}{7.3}} \ \Sigma_*^{0.5} \ . \quad (B3)$$

Finally, we assume a fixed ratio $\sigma_{*,z} = 0.6 \ \sigma_{*,r}$ to relate the radial and vertical velocity dispersions, which is reasonable for most late-type galaxies based on the limited available evidence (e.g., Shapiro et al. 2003).

These assumptions yield disk–averaged $Q_{\rm stars}$ (Equation 15) mostly in the range $\sim$ 2–4, in reasonable agreement with estimates in the Milky Way (Jog & Solomon 1984; Rafikov 2001) and the expectation that stellar disks are marginally stable against collapse, $Q_{\rm stars} \sim 2$ (Kregel & van der Kruit 2005, and references therein). Our fixed flattening ratio yields nearly identical results to the fit used by Blitz & Rosolowsky (2006) to derive h_* from l_*. The scaling between σ_* and maximum rotation velocity observed by Bottema (1993) and Kregel & van der Kruit (2005) yields roughly

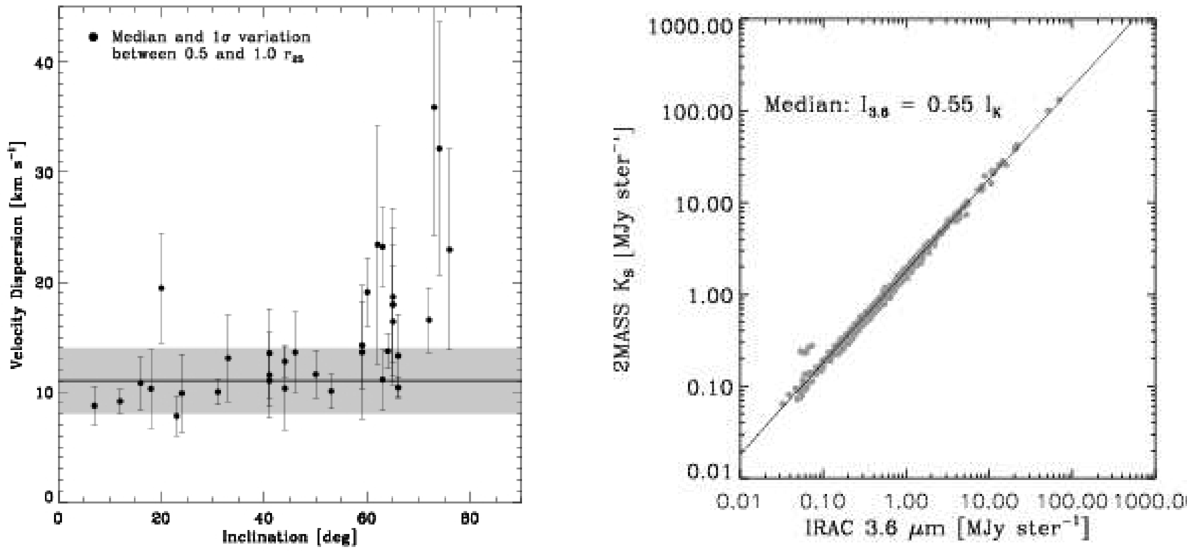

FIG. C1.— (left) Motivation for our adopted gas velocity dispersion, $\sigma_{\rm gas}$. We plot the median and 1σ range of $\sigma_{\rm gas}$ over the outer disk (0.5–1.0 r_{25}) of each THINGS galaxy (including galaxies that are not part of this study) as a function of inclination. We see that variations within a galaxy are relatively small and that $\sigma_{\rm gas} = 11 \pm 3$ km s^{-1} is a good description of galaxies with inclination $i \lesssim 60°$. Above this inclination, $\sigma_{\rm gas}$ is systematically higher with more scatter as a likely consequence of projection effects in these systems. We adopt a fixed $\sigma_{\rm gas}$ (gray line) throughout this work. (right) Median K-band intensity vs. median 3.6μm intensity in 10″-wide tilted rings. A single scaling, $I_{3.6} = 0.55\ I_K$ (shown by the solid line), relates the two well.

similar scale heights but is more sensitive to adopted structural parameters (a problem for several face–on galaxies). The scatter among the various methods to estimate σ_* or h_* and observations remains $\sim 50\%$ and this is clearly an area where more observations are needed (particularly measuring σ_* as a function of radius, though see Ciardullo et al. 2004; Merrett et al. 2006).

STELLAR SURFACE DENSITIES FROM THE IRAC 3.6 μM BAND

SINGS (Kennicutt et al. 2003) imaged most of our sample using the IRAC instrument on *Spitzer* (Fazio et al. 2004). Emission from old stellar photospheres accounts for most of the emission seen in the IRAC 3.6 μm band (e.g., Pahre et al. 2004), although we note that there may be some contribution from very hot dust and PAH features. Therefore we use these data to estimate radial profiles of the stellar surface density, Σ_*. To convert from 3.6μm intensity, $I_{3.6}$, to Σ_* we apply an empirical conversion from 3.6μm to K-band intensity and then adopt a standard K-band mass-to-light ratio.

We work with median profiles of $I_{3.6}$, taken over a series of 10″-wide tilted rings using the structural parameters in Table 4. Real azimuthal variations, e.g., due to bars or spiral arms, are lost. This is balanced by three major advantages from the median: 1) we avoid contamination by hot dust or PAH emission near star forming regions, a potential issue with the 3.6μm band; 2) we filter out foreground stars; and 3) we increase our sensitivity by averaging over the ring. The first advantage avoids a serious possible bias due to confusing Σ_* and $\Sigma_{\rm SFR}$. The latter two allow us to measure Σ_* out to large radii.

To calibrate the ratio of $I_{3.6}$ to K-band intensity, I_K, we compare $I_{3.6}$ profiles to I_K profiles from the 2MASS Large Galaxy Atlas (LGA Jarrett et al. 2003). The profiles from the LGA are not sensitive enough to reach $\gtrsim r_{25}$ in most cases, but they yield sufficient data to measure a typical I_K-to-$I_{3.6}$ ratio. The right panel in Figure C1 shows this measurement. We plot I_K as a function of $I_{3.6}$; each point gives median intensities in one 10″-wide tilted ring in one galaxy. The solid line shows a fixed ratio $I_{3.6} = 0.55\ I_K$ (both in MJy ster^{-1}), which matches the data very well. This agrees with results from Oh et al. (2008), who investigated the K-to-3.6μm ratio using stellar population modeling and found only very weak variations.

To convert I_K to Σ_* we apply a fixed K-band mass-to-light ratio, $\Upsilon_\star^K = 0.5$ M$_\odot$/L$_{\odot,K}$. This is near the mean expected for our sample: applying the Bell et al. (2003) relation between $B-V$ color and mean $\Upsilon_\star^K$, we find $\Upsilon_\star^K = 0.48$–0.60 M$_\odot$/L$_{\odot,K}$ (using global $B-V$ colors and assuming a Kroupa 2001, IMF to match our star formation rate). This small range in mean $\Upsilon_\star^K$ motivates our decision to adopt a constant value.

With our K-to-3.6μm ratio, $\Upsilon_\star^K = 0.5$ M$_\odot$/L$_{\odot,K}$, and the K-band magnitude of the Sun = 3.28 mag (Binney & Merrifield 1998), the conversion from 3.6 μm intensity to stellar surface density is

$$\Sigma_* = \Upsilon_\star^K \ \left\langle \frac{I_K}{I_{3.6}} \right\rangle \ \cos i \ I_{3.6} \ = 280 \ \cos i \ I_{3.6}, \qquad \text{(C1)}$$

with Σ_* in M$_\odot$ pc^{-2} assuming a Kroupa (2001) IMF and $I_{3.6}$ in MJy ster^{-1}.

The major uncertainty in Equation C1 is the mass–to–light ratio, which depends on the star formation history, metallicity, and IMF. The mass–to–light ratio varies less in the NIR than the optical but it does vary, showing ~ 0.1 dex scatter for redder galaxies and 0.2 dex for bluer galaxies (Bell & de Jong 2001; Bell et al. 2003). Because metallicity and star formation history exert different influences on galaxy colors and $\Upsilon_\star^K$, these variations are not readily inferred from colors (unlike in the optical, e.g., Bell et al. 2003).

In their analysis of the THINGS rotation curves, de Blok et al. (2008) also derive Σ_* from $I_{3.6}$. They use $J - K$ colors from the 2MASS LGA to estimate variations in $\Upsilon_\star^K$. Their Figure 21 compares our integrated masses to those that they derive using color–dependent $\Upsilon_\star^K$ for both a (Kroupa 2001) and "diet Salpeter" (see Bell & de Jong 2001) IMF. Because they use the Bell & de Jong (2001) results, which have a fairly strong dependence on NIR color, they find $\Upsilon_\star^K \sim 30$–40% higher than we do in massive (red) spiral galaxies, even for matched (Kroupa 2001) IMFs.

STAR FORMATION RATE SURFACE DENSITY MAPS

We combine GALEX FUV and *Spitzer* 24μm maps to estimate the star formation rate surface density, $\Sigma_{\rm SFR}$, along each line of sight. FUV maps show mostly photospheric emission from O and B stars and thus trace unobscured star formation over a timescale of $\tau_{\rm FUV} \sim 10$–100 Myr (e.g., Kennicutt 1998b; Calzetti et al. 2005; Salim et al. 2007). Emission at 24μm originates from small dust grains mainly heated by UV photons from young stars. It has been shown to directly relate to ongoing star formation over a timescale of $\tau_{24} \sim 10$ Myr (e.g., Calzetti et al. 2005; Pérez-González et al. 2006; Calzetti et al. 2007). We adopt this tracer because: 1) the resolution and sensitivity of the GALEX FUV and *Spitzer* 24μm maps are both good (and well–matched), 2) these data are available for our whole sample, and 3) the combination is directly sensitive to both exposed and embedded star formation.

In this section, we take a practical approach, calibrating our tracer by comparing it to other estimates of $\Sigma_{\rm SFR}$. For a more thorough discussion of the relationship between extinction, UV, and IR emission, we refer the reader to, e.g., Calzetti et al. (1995); Buat et al. (2002); Bell (2003); Cortese et al. (2006); Boissier et al. (2007). Our tracer builds mainly on two recent results: 1) for entire galaxies, Salim et al. (2007) showed that FUV emission can be used to accurately measure star formation rates (with typical $\tau_{\rm FUV} \sim 20$ Myr) if extinction is properly accounted for and 2) Calzetti et al. (2007) and Kennicutt et al. (2007) demonstrated that 24μm data could be used to accurately correct Hα for extinction. We combine these results using a method similar to that of Calzetti et al. (2007): via comparisons to other estimates of extinction–corrected $\Sigma_{\rm SFR}$, we derive a linear combination of FUV and 24μm intensity that we use to estimate $\Sigma_{\rm SFR}$,

$$\Sigma_{\rm SFR} = \left(\ 8.1 \times 10^{-2}\ I_{\rm FUV} + 3.2^{+1.2}_{-0.7} \times 10^{-3}\ I_{24}\ \right)\ \cos i\ . \qquad \text{(D1)}$$

Here $\Sigma_{\rm SFR}$ has units of M$_\odot$ kpc^{-2} yr^{-1} and FUV and 24μm intensity are each in MJy ster^{-1}. The first term measured unobscured SFR using the FUV-to-SFR calibration found by Salim et al. (2007); the second term measures embedded SFR from 24μm and is 30% higher than the matching term in the Hα+24μm calibration of Calzetti et al. (2007). The additional weight reflects the fact that FUV is more heavily absorbed than Hα. More detailed motivation for Equation D1 is given in Appendix D.2.

Following Calzetti et al. (2007), Equation D1 assumes the default initial mass function (IMF) of STARBURST99 (Leitherer et al. 1999), the broken power law given by Kroupa (2001) with a maximum mass of 120 M$_\odot$. This yields $\Sigma_{\rm SFR}$ a factor of 1.59 lower than a 0.1–100 M$_\odot$ Salpeter (1955) IMF (e.g. Kennicutt 1989, 1998a). Our FUV term is Equation 10 from Salim et al. (2007) divided by this value (1.59); the calibration is the same found for the Chabrier (2003) IMF over the range 0.1–100 M$_\odot$ (their Equations 7 and 8).

Data

GALEX NGS FUV Maps

We use FUV maps obtained by the GALEX satellite (Martin et al. 2005) as part of the GALEX Nearby Galaxies Survey (NGS, Gil de Paz et al. 2007). The GALEX FUV band covers $\lambda = 1350$–1750 Å with a resolution of 5.6$''$ and a 1.25° diameter field of view. These maps have excellent sensitivity and well-behaved backgrounds over a large field of view. GALEX simultaneously observes in a near–UV (NUV) band ($\lambda = 1750$–2750 Å). We use these data to measure UV colors and to identify foreground stars.

We correct the FUV maps for Galactic extinction using the dust map of Schlegel et al. (1998). We subtract a small background, measured away from the galaxy. We identify and remove foreground stars using their UV color: any pixel with a NUV–to–FUV intensity ratio $\gtrsim 15$ (varying ± 5 from galaxy–to–galaxy) that is also detected in the NUV map with $> 5\sigma$ significance is blanked. In convolution to our working resolution, blank pixels are replaced with the average of nearby data. We also blank a few regions with obvious artifacts. These include bright stars (e.g., in NGC 3198 and NGC 6946) that are usually beyond the optical radius of the galaxy and M51b, the companion of M51a.

SINGS 24μm Maps

We use maps of 24μm emission obtained as part of the SINGS Legacy program (Kennicutt et al. 2003) using the MIPS instrument on *Spitzer* (Rieke et al. 2004). Gordon et al. (2005) describe the reduction of these scan maps, which have 6$''$ resolution. The sensitivity and background subtraction are both very good, and it is typical to find 3σ emission at $\sim r_{25}$ in a spiral. The MIPS PSF at 24μm is complex at low levels, but our working resolution of $\sim 20''$ makes this only a minor concern.

NGC 3077, NGC 4214, and NGC 4449 are not part of SINGS. For these galaxies we use 24μm (and IRAC) maps from the *Spitzer* archive. We use the post basic calibrated data produced by the automated *Spitzer* pipeline.

As with the FUV maps, we subtract a small background from the 24 μm maps, which we measure away from the galaxy. We blank the same set of foreground stars as in the FUV maps. In convolution to our working resolution, these pixels are replaced with the average of nearby data. We also blank the edges of the 24μm maps perpendicular to the scan, which are noisy (and outside the optical radius) and the same artifacts blanked in the FUV maps.

SINGS Hα

The SINGS fourth data release includes Hα maps, which we use to compare $\Sigma_{\rm SFR}$ derived from Hα, FUV, and 24μm emission in 13 galaxies. We convert Hα to $\Sigma_{\rm SFR}$ following Calzetti et al. (2007) and the SINGS data release documentation. We correct for [NII] contamination following Calzetti et al. (2005) and Lee (2006) and correct for Galactic extinction using the Schlegel et al. (1998) dust maps. We check the flat-fielding by eye and mask regions or fit backgrounds where necessary.

Motivation for the FUV+24 to $\Sigma_{\rm SFR}$ Relation

Because 24μm lies well short of the FIR peak for a typical galaxy SED (e.g., Dale & Helou 2002), a measurement in this band does not directly trace the total IR luminosity. Therefore using 24μm to measure embedded SFR relies on modeling of the IR SED or empirical calibration against other estimates of extinction. Calzetti et al. (2007) compared Hα and 24μm to Paschen α (Paα) emission, a tracer of ionizing photons largely unaffected by extinction. They showed that a linear combination of Hα and 24μm,

$$\begin{aligned} {\rm SFR}_{\rm Tot} &= {\rm SFR}_{\rm H\alpha}^{\rm unobscured}\left({\rm H}\alpha\right) + {\rm SFR}_{\rm H\alpha}^{\rm embedded}\left(24\mu{\rm m}\right) \\ {\rm SFR}_{\rm Tot} &= 5.3\times10^{-42}\left(L\left(H\alpha\right) + 0.031\ L\left(24\mu{\rm m}\right)\right)\ , \end{aligned} \tag{D2}$$

matches ${\rm SFR}_{\rm Tot}$ inferred from Paα for 220 individual star forming regions in 33 nearby galaxies and that the same calibration also works well when integrated over a large fraction of a galaxy disk. Here $L\left(H\alpha\right)$ is the luminosity of Hα emission from the region in erg s^{-1} and $L\left(24\mu{\rm m}\right) = \nu_{24\mu{\rm m}}\ L_\nu\left(24\mu{\rm m}\right)$, also in erg s^{-1}, is the specific luminosity of the region times the frequency at 24μm. SFR is the star formation rate in that region in M$_\odot$ yr^{-1}.

We require an analogous formula to combine FUV and 24μm data,

$${\rm SFR}_{\rm Tot} = {\rm SFR}_{\rm FUV}^{\rm unobscured}\left({\rm FUV}\right) + {\rm SFR}_{\rm FUV}^{\rm embedded}\left({\rm FUV}, 24\mu{\rm m}\right)\ . \tag{D3}$$

The first term is the SFR implied by a particular FUV luminosity taking no account of internal extinction. The second term is the SFR that can be attributed to FUV light that does not reach us — i.e., the extinction correction for the first term —, which we infer from the 24μm luminosity and may also depend on the ratio of FUV to 24μm intensity.

We adopt the first term in Equation D3 from Salim et al. (2007), who studied the relationship between FUV emission and SFR in $\sim 50,000$ galaxies, combining multi-band photometry with population synthesis modeling and comparing to Hα emission. They found

$${\rm SFR}_{\rm FUV}^{\rm unobscured} = 0.68\times10^{-28}\ L_\nu\left({\rm FUV}\right)\ , \tag{D4}$$

with SFR in M$_\odot$ yr^{-1} and $L_\nu\left({\rm FUV}\right)$ in erg s^{-1} Hz^{-1}. This yields SFRs $\sim 30\%$ lower than the relation given by Kennicutt (1998b) because of metallicity, model, and star formation history differences between their sample and Kennicutt's model.

We calibrate the second term in Equation D3 in two ways: 1) we use simple assumptions to extrapolate ${\rm SFR}_{\rm FUV}^{\rm embedded}\left({\rm FUV}, 24\mu{\rm m}\right)$ from ${\rm SFR}_{\rm H\alpha}^{\rm embedded}\left(24\mu{\rm m}\right)$, which was measured by Calzetti et al. (2007); and 2) we make several independent estimates of ${\rm SFR}_{\rm Tot}$ — by comparing ${\rm SFR}_{\rm Tot}$ with FUV emission, we directly measure the second term in Equation D3. We phrase both analyses in terms of the factor $W_{\rm FUV}$, defined as

$$W_{\rm FUV}\left({\rm FUV}, 24\mu{\rm m}\right) = \frac{{\rm SFR}_{\rm FUV}^{\rm embedded}}{{\rm SFR}_{\rm H\alpha}^{\rm embedded}\left(24\mu{\rm m}\right)}\ . \tag{D5}$$

The numerator is the second term in Equation D3 and the denominator is the relation between embedded Hα and 24μm emission measured by Calzetti et al. (2007, Equation D2). To measure $W_{\rm FUV}$, we combine Equations D3 and D5 to obtain

$${\rm SFR}_{\rm Tot} = {\rm SFR}_{\rm FUV}^{\rm unobscured}\left({\rm FUV}\right) + W_{\rm FUV}\left({\rm FUV}, 24\mu{\rm m}\right){\rm SFR}_{\rm H\alpha}^{\rm embedded}\left(24\mu{\rm m}\right) \tag{D6}$$

and solve for $W_{\rm FUV}$ in terms of measurable quantities

$$W_{\rm FUV} = \frac{{\rm SFR}_{\rm Tot} - {\rm SFR}_{\rm FUV}^{\rm unobscured}\left({\rm FUV}\right)}{{\rm SFR}_{\rm H\alpha}^{\rm embedded}\left(24\mu{\rm m}\right)}\ . \tag{D7}$$

So that to estimate $W_{\rm FUV}$ over a line of sight we require FUV and 24μm intensities and an estimate of ${\rm SFR}_{\rm Tot}$.

Simple Extrapolation

In conjunction with a direct measurement, it is helpful to have a basic expectation for $W_{\rm FUV}$. We calculate this by combining a Galactic extinction law and a typical nebular-to-stellar extinction ratio. In terms of Hα extinction, $A_{\rm H\alpha}$, and FUV extinction, $A_{\rm FUV}$, Equations D2 and D3 are

$$\begin{aligned} {\rm SFR_{Tot}} &= {\rm SFR_{H\alpha}^{unobscured}}\ 10^{A_{\rm H\alpha}/2.5} \\ {\rm SFR_{Tot}} &= {\rm SFR_{FUV}^{unobscured}}\ 10^{A_{\rm FUV}/2.5}\ . \end{aligned} \tag{D8}$$

For a Galactic extinction law $A_{\rm FUV}/A_R \approx 8.24/2.33$ (Cardelli et al. 1989; Wyder et al. 2007). We may also expect that FUV originates from a slightly older and more dispersed population than Hα. If we assume a typical nebular-to-stellar extinction ratio of $A_{\rm H\alpha}/A_R \approx 2$ (Calzetti et al. 1994; Roussel et al. 2005), then we expect $A_{\rm FUV}/A_{\rm H\alpha} \approx 1.8$ (if FUV comes mostly from a very young population coincident with Hα, we instead expect $A_{\rm FUV}/A_{\rm H\alpha} \sim 3.6$). Combined with Equations D3 – D8 these assumptions yield

$$\frac{1}{f + W_{\rm FUV} - 1} + 1 = \left(\frac{W_{\rm FUV}}{f} + 1\right)^{1/1.8} \quad {\rm where}\ f = \frac{{\rm SFR_{FUV}^{unobscured}}\,({\rm FUV})}{{\rm SFR_{H\alpha}^{embedded}}\,(24\mu{\rm m})}\ , \tag{D9}$$

which we may solve for $W_{\rm FUV}$ given f, the ratio of observed FUV-to-24μm intensities (in SFR units).

For $A_{\rm H\alpha} = 1.1$ mag, a typical value in disk galaxies (Kennicutt 1998b), $f \approx 0.26$ and Equation D9 suggests $W_{\rm FUV} \approx 1.3$. For higher $A_{\rm H\alpha}$, expected for the inner parts of spiral galaxies or arms, f will be lower and we expect lower values of $W_{\rm FUV}$, approaching $W_{\rm FUV} = 1$ where both FUV and Hα are almost totally absorbed (and ${\rm SFR_{Tot}}$ is determined totally from 24μm emission). For lower $A_{\rm H\alpha}$, e.g., expected in dwarf galaxies or the outer parts of spirals, we expect $W_{\rm FUV}$ to approach the ratio of extinctions, 1.8, in the optically thin case.

Measuring $W_{\rm FUV}$

We measure $W_{\rm FUV}$ directly from observations by comparing FUV and 24μm emission to various estimates of ${\rm SFR_{Tot}}$. We perform these tests in the 13 galaxies with SINGS Hα data. Over a common set of lines of sight where we estimate Hα, FUV, and 24μm to all be complete, we estimate $\Sigma_{\rm SFR}$ and $W_{\rm FUV}$ (from Equation D7) in 5 ways:

1. Combining Hα+24μm using Equation D2 (Calzetti et al. 2007).

2. From 24μm emission alone, using the (nonlinear) relation found by Calzetti et al. (2007, their Equation 8).

3. From Hα alone, taking $A_{\rm H\alpha} = 1.1$ mag, a typical extinction averaged over disk galaxies, though not necessarily a good approximation for each line of sight (Kennicutt 1998b).

4. From Hα emission, estimating $A_{\rm H\alpha}$ from $\Sigma_{\rm HI}$ and $\Sigma_{\rm H2}$ following Wong & Blitz (2002). We assume a Galactic dust–to–gas ratio and treat dust associated with H I as a foreground screen obscuring the Hα while treating dust associated with H_2 as evenly mixed with Hα emission.

5. From FUV emission, estimating $A_{\rm FUV}$ for every line of sight applying the relationship between FUV–to–NUV color and $A_{\rm FUV}$ measured for nearby galaxies by Boissier et al. (2007).

In principal, the first method is superior to the others because Calzetti et al. (2007) directly calibrated it against Paα, and because it incorporates both Hα and IR emission, offering direct tracers of both ionizing photons and dust–absorbed UV light. The other four methods offer checks on ${\rm SFR_{Tot}}$ that are variously independent of 24μm, FUV, or Hα emission, allowing us to estimate the plausible range of both $W_{\rm FUV}$ and the uncertainty in $\Sigma_{\rm SFR}$.

Derived Relation

Figure D1 shows the results of these calculations. In the top panel, we plot the normalized distribution of $W_{\rm FUV}$ for each estimate of $\Sigma_{\rm SFR}$. The bottom left panel shows how each distribution of $W_{\rm FUV}$ depends on the FUV–to–24μm ratio, f (Equation D9). The bottom right panel shows how $W_{\rm FUV}$ varies with normalized galactocentric radius.

The median $W_{\rm FUV}$ derived in various ways spans a range from $\sim 1.0 - 1.8$. The two 24μm–based methods (blue and gray) both yield $W_{\rm FUV} \sim 1.3$ with relatively narrow distributions. Using FUV and UV–colors yields the highest expected $W_{\rm FUV}$, ~ 1.8; estimating $A_{\rm H\alpha}$ from gas yields the lowest $W_{\rm FUV}$, peaked near ~ 1.0, though the distribution is very wide. This range of values agrees reasonably with our extrapolation (seen as a dash–dotted curve in the top right panel), which also lead us to expect a typical $W_{\rm FUV}$ of 1.3 and a reasonable range of 1.0–1.8.

The bottom panels show that while individual methods to estimate $W_{\rm FUV}$ do exhibit significant systematics (particularly at very high and low of f), simply fixing $W_{\rm FUV} = 1.3$ is a reasonable description of most data (the dashed lines in the center panel bracket $\sim 80\%$ of the measured f). $W_{\rm FUV}$ does not have to be constant. Indeed, we expect it to vary with f based on simple assumptions and very basic arguments. However, a constant $W_{\rm FUV}$ is consistent with the data and is also the simplest, most conservative approach. Therefore, this is how we proceed: taking $W_{\rm FUV} = 1.3^{+0.5}_{-0.3}$, Equation D3 becomes

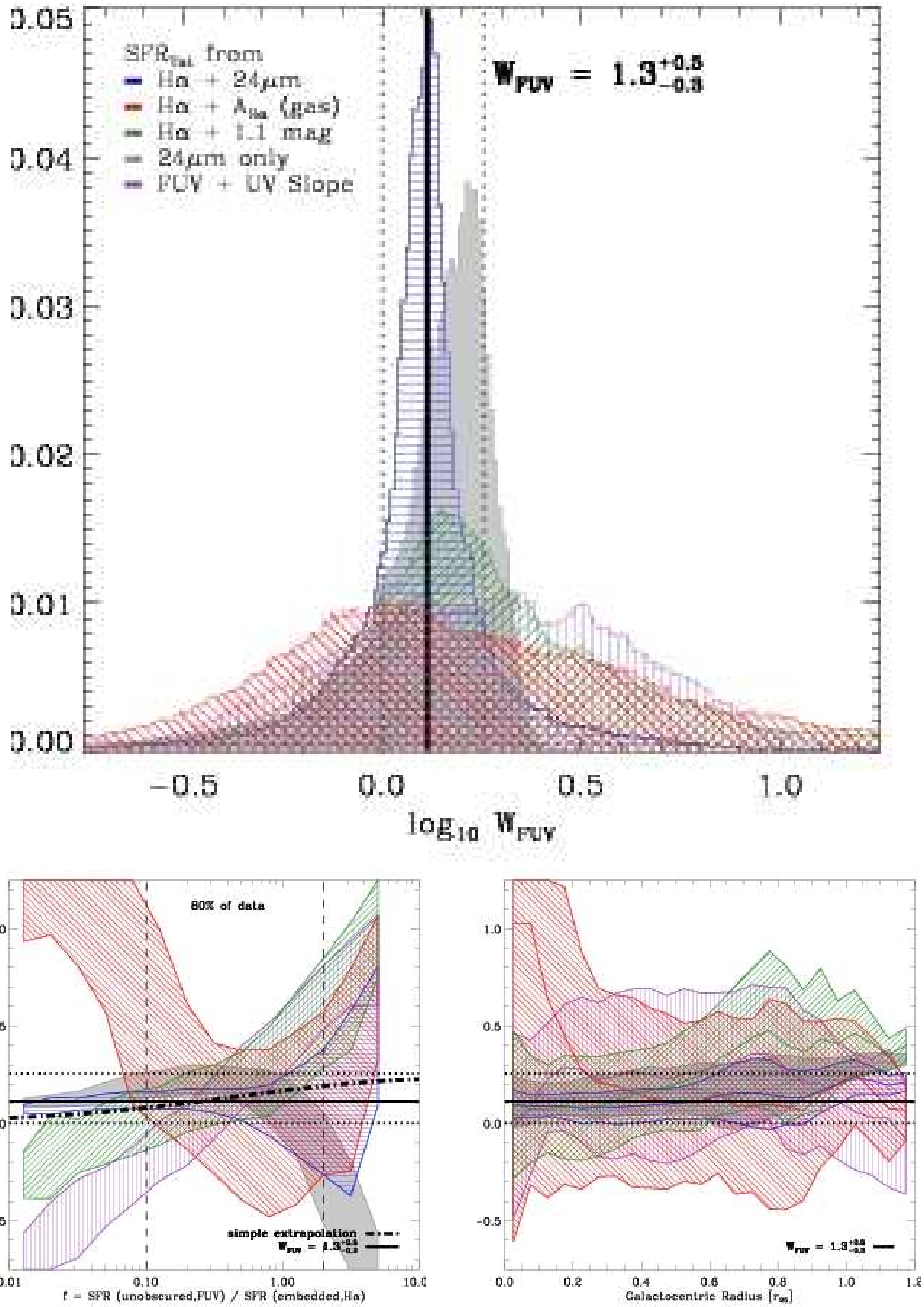

Fig. D1.— $W_{\rm FUV}$, the calibration of the 24μm term to estimate the SFR from a linear combination of FUV and 24μm emission. We measure $W_{\rm FUV}$ pixel–by–pixel by comparing FUV and 24μm intensity to $\Sigma_{\rm SFR}$ estimated in five ways: (*blue*) combining Hα and 24μm; (*gray*) using only 24μm; (*red*) using Hα, estimating extinction from the gas; (*green*) using Hα, assuming a typical extinction; and (*purple*) using FUV emission, estimating $A_{\rm FUV}$ from the UV color. We plot the resulting $W_{\rm FUV}$ in three ways: (*top*) as normalized histograms; (*bottom left*) as a function of f, the ratio FUV to 24μm emission along a line of sight (see Equation D9); and (*bottom right*) as a function of galactocentric radius normalized by r_{25}. The hatched regions in the bottom panels show the median trend $\pm 1\sigma$ for each case. In each panel, we indicate our adopted $W_{\rm FUV} = 1.3^{+0.5}_{-0.3}$. The dash–dotted curve in the bottom left panel shows the expectation for a typical extinction law and nebular-to-stellar extinction ratio and the vertical dashed lines show the range of f that includes 80% of the data.

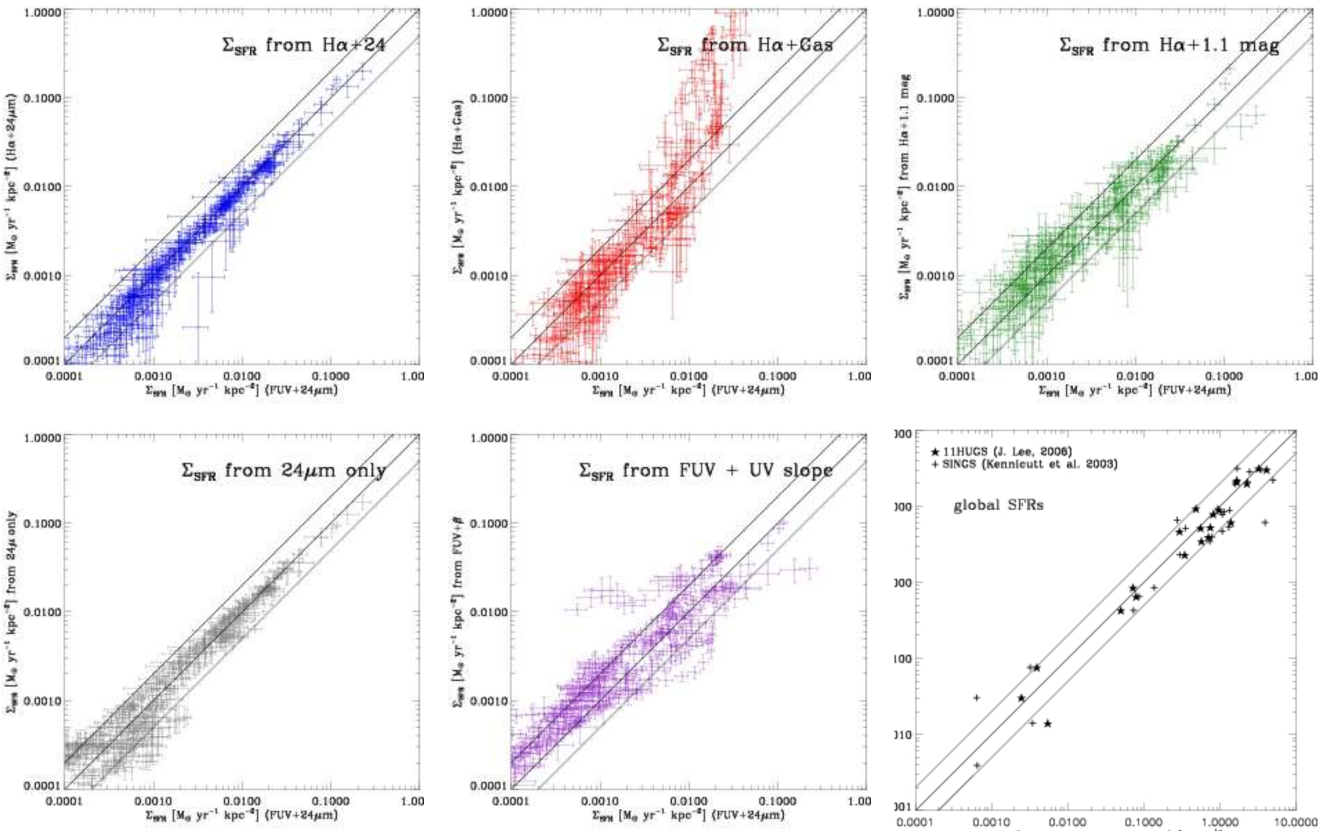

FIG. D2.— Five estimates of $\Sigma_{\rm SFR}$ (y-axis) as a function of $\Sigma_{\rm SFR}$ predicted by our combination of FUV and 24μm. The color scheme is the same as Figure D1 and the methodology used to derive $\Sigma_{\rm SFR}$ for comparison is labeled in each plot. In the bottom right panel, each point shows the integrated SFR for a galaxy derived from Hα as a function of the SFR derived from FUV+24μm emission. In all plots, solid lines show slopes of 0.5, 1, and 2.

$$\mathrm{SFR_{Tot}} = 0.68 \times 10^{-28}\ L_\nu\,(\mathrm{FUV}) + 2.14^{+0.82}_{-0.49} \times 10^{-42}\ L\,(24\mu\mathrm{m})\ , \quad \text{(D10)}$$

We convert Equation D10 from luminosity to intensity units using $\nu_{24\mu\rm m} = 1.25 \times 10^{13}$ Hz, 1 MJy$=10^{-17}$ erg s^{-1} Hz^{-1} cm^{-2}, and $L_\nu = 4\pi\ A\ I_\nu$, where A is the physical area subtended by the patch of sky being considered. This yields Equation D1,

$$\Sigma_{\rm SFR} = 8.1 \times 10^{-2} I_{\rm FUV} + 3.2^{+1.2}_{-0.7} \times 10^{-3} I_{24}\ , \quad \text{(D11)}$$

with $I_{\rm FUV}$ and I_{24} in units of MJy ster^{-1} and $\Sigma_{\rm SFR}$ in units of M$_\odot$ kpc^{-2} yr^{-1}.

Uncertainty in $\Sigma_{\rm SFR}$

In Figure D2, we plot our 5 alternate estimates of $\Sigma_{\rm SFR}$ (y–axis) as a function of $\Sigma_{\rm SFR}$ derived from Equation D11 (x–axis). Each point corresponds to a $10''$-wide tilted ring. In the bottom right panel, we plot the SFR integrated over the disk (over $r_{\rm gal} < r_{25}$) as a function of SFR estimated from nebular line emission by Kennicutt et al. (2003) and Hα by Lee (2006). Solid lines in all six panels show the line of equality plus or minus a factor of 2.

If we adopt the naive tack of treating all approaches as equal, the aggregate data in Figure D2 yield a median ratio $\Sigma_{\rm SFR}$ (other)/$\Sigma_{\rm SFR}$(FUV + 24) ≈ 1.05 with ≈ 0.22 dex (i.e., $\sim 65\%$) 1σ scatter. The dominant sources of this scatter are the choice of "other" $\Sigma_{\rm SFR}$ and galaxy–to–galaxy variations. Once a galaxy and methodology are chosen, the data tend to follow a fairly well–defined and often nearly linear relation. For comparison, the 24μm part of the Hα+24μm calibration has $\approx$ 20–30% uncertainty (Calzetti et al. 2007; Kennicutt et al. 2007) only considering star forming peaks. In light of the wider range of star formation histories and geometries encountered working pixel–by–pixel or averaging over whole rings, the estimate of $\sim 65\%$ seems quite reasonable. Comparing our *integrated* SFRs (Figure D2, bottom right) to those estimated by 11HUGS Lee (2006) and SINGS Kennicutt et al. (2003) bears out this estimate; we match these estimates with a similar scatter. Another view of this comparison may be seen in Appendix F, where we present radial profiles of $\Sigma_{\rm SFR}$ based on Hα on the same plots as our FUV+24μm profiles.

Despite the overall good agreement between our $\Sigma_{\rm SFR}$ and other estimates, Figures D1 and D2 do show systematic differences among tracers. We note several of these before moving on:

1. Using only 24μm emission (gray) yields a low estimate of $\Sigma_{\rm SFR}$ for the two low metallicity galaxies in our comparison sample: Holmberg II and IC 2574. Dust is known to be deficient in these galaxies (Walter et al. 2007), which is likely to lead to a breakdown in the fit between 24μm emission and Paα. This effect, already recognized by Calzetti et al. (2007), highlights the importance of including a non–IR component in a SFR tracer.

2. Estimating $A_{\rm H\alpha}$ from gas (red, Wong & Blitz 2002) yields very high $\Sigma_{\rm SFR}$ (and high $W_{\rm FUV}$) in the inner parts of galaxies. This underscores the complexity of the geometry and timescale effects at play; it is extremely challenging to reverse engineer the true luminosity of a heavily obscured source knowing only the amount of nearby interstellar matter. These high values are almost certainly overestimates; stellar feedback, turbulence, or simply favorable geometry likely always allows at least some light from deeply embedded H II regions to escape.

3. Particularly at low $\Sigma_{\rm SFR}$, inferring $A_{\rm FUV}$ from UV colors (purple) yields higher embedded SFR than using 24μm emission (and this method appears to completely fail in NGC 6946, the horizontal row of points). A possible explanation is that where $\Sigma_{\rm SFR}$ is relatively low, the UV originates from a somewhat older (and thus redder) population (e.g. Calzetti et al. 2005); the FUV–UV color relation depends on the recent star formation history (e.g., differing between starbursts and more quiescent galaxies, Boissier et al. 2007; Salim et al. 2007).

   This discrepancy (and the close association between our SFR tracer and stellar mass seen in the main text) argues for a comparison among metallicity, stellar populations, and mid–IR emission that is beyond the scope of this paper. We restrict ourselves to a first–order check: we compare the ratio of 24μm–to–3.6μm and FUV–to–3.6μm emission in our sample to those in elliptical galaxies, which should be good indicators of how much an old population contributes to 24μm or FUV emission. Very approximately, in ellipticals $I_{24}/I_{3.6} \sim 0.1$ (Temi et al. 2005; Dale et al. 2007; Johnson et al. 2007), with ~ 0.03 expected from stellar emission alone (Helou et al. 2004), while $I_{\rm FUV}/I_{3.6} \sim 2$–$4 \times 10^{-3}$ (Dale et al. 2007; Johnson et al. 2007, taking the oldest bin from the latter). We measure $I_{24}/I_{3.6}$ and $I_{\rm FUV}/I_{3.6}$ for each ring in our sample galaxies and compare these to the elliptical colors. In both cases, only $\sim 5\%$ of individual tilted rings have ratios lower than those seen in elliptical galaxies and the mean color is ~ 10 times that found in elliptical galaxies, though the ratio $I_{\rm FUV}/I_{3.6}$ shows large scatter due to the effects of extinction. Both the 24μm and FUV bands do appear to be dominated by a young stellar population almost everywhere in our sample. Discrepancies among various tracers thus seem likely to arise from the different geometries and age sensitivities of FUV ($\tau \sim 100$ Myr), Hα ($\tau \sim 10$ Myr), and 24μm (likely intermediate) emission.

Finally, we emphasize that uncertainties inferred via these comparisons mainly reflect the ability to accurately infer the total UV light or ionizing photon production from young stars. They do not include uncertainty in the IMF, ionizing photon production rate (e.g., at low metallicity), or any of the other factors involved in converting an ionizing photon count or FUV intensity into a SFR.

RADIAL PROFILES

Table E1 presents radial profiles of $\Sigma_{\rm HI}$, $\Sigma_{\rm H2}$, Σ_*, and $\Sigma_{\rm SFR}$. Combined with kinematics, which may be calculated using Equation B1 taking $v_{\rm flat}$ and $l_{\rm flat}$ from Table 4, these profiles are intended to provide a database that can be used to test theories of galaxy–wide star formation or to explore the effects of varying our assumptions. Results for all galaxies are available in an electronic table online. Table E1 in the print edition shows the results for our lowest–mass spiral galaxy, NGC 628, as an example.

The individual columns are as follows. *Ring identifiers:* (1) galaxy name; galactocentric radius of ring center (2) in kpc and (3) normalized by r_{25}. *Mass surface densities* (in $M_\odot$ pc^{-2}) along with associated uncertainty of (4–5) H I; (6–7) H_2; and (8–9) stars. *Star formation rate surface density*, $\Sigma_{\rm SFR}$, with associated uncertainty (10–11) from combining FUV and 24μm emission in units of 10^{-4} $M_\odot$ yr^{-1} kpc^{-2}; and the individual contributions to $\Sigma_{\rm SFR}$ from (12) FUV and (13) 24μm emission (i.e., the left and right terms in D1) in the same units.

We derive radial profiles from maps using the mean (for $\Sigma_{\rm HI}$, $\Sigma_{\rm H2}$, $\Sigma_{\rm SFR}$) or median (Σ_*) value within $10''$-wide tilted rings (so that the rings are spaced by half of our typical working resolution). The rings use the position angle and inclination in Table 4, adopted from Walter et al. (2008). We adopt the THINGS center for each galaxy (Walter et al. 2008; Trachternach et al. 2008) except for Holmberg I, where we use the dynamical center derived by Ott et al. (2001) rather than the photometric center. We consider only data within 60° of the major axis, measured in the plane of the galaxy. This minimizes our sensitivity to the adopted structural parameters, which most strongly affect the deprojection along the minor axis. Where there are no data, we take $\Sigma_{\rm HI} = 0$ and $\Sigma_{\rm H2} = 0$. These are regions that have been observed but masked out because no signal was identified. We ignore pixels with no measurement of $\Sigma_{\rm SFR}$, these are simply missing data.

We take the uncertainty in a quantity averaged over a tilted ring to be

$$\sigma = \frac{\sigma_{\rm RMS}}{\sqrt{N_{\rm pix,ring}/N_{\rm pix,beam}}} \tag{E1}$$

where $\sigma_{\rm RMS}$ is the RMS scatter within the tilted ring, $N_{\rm pix,ring}$ is the number of pixels in the ring, and $N_{\rm pix,beam}$ is the number of pixels per resolution element. This σ captures both random scatter in the data and variations due to

TABLE E1
TABLE OF RADIAL PROFILES[a]

Galaxy	r_{gal} (kpc)	r_{gal} (r_{25})	Σ_{HI} ($M_\odot$ pc^{-2})	Σ_{H2} ($M_\odot$ pc^{-2})	Σ_* ($M_\odot$ pc^{-2})	FUV+24 (10^{-4} $M_\odot$ yr^{-1} kpc^{-2})	FUV part	24μm part
NGC0628	0.2	0.02	1.6 ± 0.3	22.7 ± 1.2	1209.4 ± 18.3	105.1 ± 14.0	19.3	85.8
NGC0628	0.5	0.05	2.1 ± 0.3	20.2 ± 1.3	557.8 ± 4.8	92.3 ± 9.9	17.1	75.1
NGC0628	0.9	0.08	2.6 ± 0.4	16.1 ± 1.2	313.6 ± 1.0	76.7 ± 5.1	15.1	61.6
NGC0628	1.2	0.12	3.1 ± 0.4	12.7 ± 0.8	231.9 ± 0.5	65.5 ± 4.2	14.2	51.3
NGC0628	1.6	0.15	3.7 ± 0.3	11.4 ± 1.1	194.3 ± 0.5	62.2 ± 3.7	13.8	48.4
NGC0628	1.9	0.19	4.6 ± 0.3	11.1 ± 1.2	163.5 ± 0.7	72.4 ± 12.2	15.3	57.1
NGC0628	2.3	0.22	5.3 ± 0.4	11.1 ± 1.7	143.9 ± 0.8	90.2 ± 23.5	18.0	72.2
NGC0628	2.7	0.25	5.8 ± 0.5	10.6 ± 1.9	123.5 ± 0.5	90.7 ± 21.3	19.1	71.6
NGC0628	3.0	0.29	6.1 ± 0.5	8.9 ± 1.5	107.5 ± 0.4	71.9 ± 11.9	17.7	54.2
NGC0628	3.4	0.32	6.5 ± 0.5	7.2 ± 1.2	151.0 ± 10.5	57.9 ± 8.5	15.7	42.2
NGC0628	3.7	0.36	7.3 ± 0.7	6.2 ± 1.5	81.6 ± 0.4	55.8 ± 11.3	14.3	41.6
NGC0628	4.1	0.39	7.9 ± 0.8	5.9 ± 1.7	68.0 ± 0.4	59.6 ± 14.1	13.5	46.1
NGC0628	4.4	0.42	8.1 ± 0.8	5.4 ± 1.5	61.6 ± 0.4	59.9 ± 15.2	13.9	46.0
NGC0628	4.8	0.46	7.9 ± 0.9	4.3 ± 1.1	48.3 ± 0.2	48.8 ± 11.0	13.6	35.2
NGC0628	5.1	0.49	8.2 ± 1.0	3.1 ± 0.8	41.8 ± 0.2	37.4 ± 6.6	12.7	24.7
NGC0628	5.5	0.53	8.5 ± 1.0	2.1 ± 0.7	37.0 ± 0.2	33.5 ± 8.7	12.3	21.2
NGC0628	5.8	0.56	8.6 ± 0.8	1.2 ± 0.5	33.2 ± 0.4	30.2 ± 10.0	11.9	18.4
NGC0628	6.2	0.59	8.6 ± 0.7	≤ 1.0	37.0 ± 2.3	23.5 ± 6.5	10.1	13.5
NGC0628	6.5	0.63	8.8 ± 0.6	≤ 1.0	52.9 ± 6.1	17.4 ± 3.1	8.0	9.4
NGC0628	6.9	0.66	8.8 ± 0.5	≤ 1.0	19.5 ± 0.1	13.6 ± 1.9	6.6	7.0
NGC0628	7.3	0.69	8.6 ± 0.5	≤ 1.0	18.9 ± 0.1	11.6 ± 2.3	5.7	5.9
NGC0628	7.6	0.73	8.2 ± 0.6	≤ 1.0	18.7 ± 0.7	9.8 ± 2.2	5.1	4.8
NGC0628	8.0	0.76	7.6 ± 0.6	≤ 1.0	12.9 ± 0.1	7.5 ± 1.5	4.1	3.4
NGC0628	8.3	0.80	7.1 ± 0.6	≤ 1.0	17.6 ± 1.3	5.4 ± 0.9	3.1	2.3
NGC0628	8.7	0.83	6.7 ± 0.5	≤ 1.0	17.0 ± 1.6	4.1 ± 0.6	2.4	1.7
NGC0628	9.0	0.86	6.5 ± 0.4	≤ 1.0	10.8 ± 0.4	3.2 ± 0.4	2.0	1.3
NGC0628	9.4	0.90	6.0 ± 0.5	≤ 1.0	8.0 ± 0.1	2.5 ± 0.3	1.7	0.8
NGC0628	9.7	0.93	5.2 ± 0.4	≤ 1.0	7.5 ± 0.2	1.8 ± 0.3	1.3	0.5
NGC0628	10.1	0.97	4.5 ± 0.4	≤ 1.0	5.0 ± 0.1	1.2 ± 0.2	0.9	0.3
NGC0628	10.4	1.00	4.1 ± 0.3	≤ 1.0	4.1 ± 0.0	≤ 1.0	···	···
NGC0628	10.8	1.03	3.9 ± 0.3	≤ 1.0	3.6 ± 0.0	≤ 1.0	···	···
NGC0628	11.1	1.07	3.9 ± 0.4	≤ 1.0	3.9 ± 0.1	1.0 ± 0.4	0.7	0.3
NGC0628	11.5	1.10	4.0 ± 0.4	≤ 1.0	4.4 ± 0.2	≤ 1.0	···	···
NGC0628	11.9	1.13	4.3 ± 0.5	≤ 1.0	9.5 ± 0.9	≤ 1.0	···	···
NGC0628	12.2	1.17	4.6 ± 0.5	≤ 1.0	5.8 ± 0.2	≤ 1.0	···	···

[a]The full table of radial profile data is available in electronic form.

azimuthal structure within the ring. It does not capture systematic uncertainties, e.g., due to choice of X_{CO} or star formation tracer, discussed in these appendices.

ATLAS OF MAPS AND PROFILE PLOTS

In Figure F, we present maps, profiles, and calculations for individual galaxies. Each page shows results for one galaxy. The top row shows maps of atomic gas (Σ_{HI}), molecular gas (Σ_{H2}), and total gas ($\Sigma_{gas} = \Sigma_{HI} + \Sigma_{H2}$). The second row shows unobscured (FUV), dust-embedded (24μm), and total star formation surface density (Σ_{SFR}). These maps use a color scheme based on the modified magnitude system described by Lupton et al. (1999); a bar to the right of each row of plots illustrates the scheme. The gas maps and star formation maps for each galaxy use a single color scheme, but the scheme does vary from galaxy to galaxy, so care should be taken when comparing different galaxies. Also note that we construct the table to show empty values below our working sensitivity (i.e., any data below $\Sigma_{gas} = 1$ $M_\odot$ pc^{-2} or $\Sigma_{SFR} = 10^{-4}$ $M_\odot$ yr^{-1} kpc^{-2} appear as white) but the data (especially THINGS) often show evidence of real emission below this value. We refer the readers to the original data papers for more information on each data set.

The dotted circle indicates the optical radius, r_{25}, in the plane of the galaxy for the structural parameters given in Table 4. A small black circle in the bottom right panel shows our working resolution.

In the left panel on the third row, we plot mass surface density profiles. We show H I (blue), H_2 (magenta, where available), stars (red stars), and total gas (thick gray profile). Vertical dotted lines indicate 0.25, 0.5, 0.75, and 1.0 times r_{25}. Horizontal dotted lines show fixed mass surface density. The thick gray vertical line shows where the intensity scale for the images is set, i.e., 0.1 r_{25}.

In the right panel on the third row, we plot star formation rate surface density profiles. We show the total Σ_{SFR} (thick gray profile) and the separate contributions from dust-embedded (green, 24μm) and unobscured (blue, FUV) star formation, which add up to Σ_{SFR}. Where they are available, we plot Σ_{SFR} from the SINGS DR4 Hα (red) and points measured from the Hα profiles of Martin & Kennicutt (2001) (magenta) and Wong & Blitz (2002) (purple). All Hα profiles assume 1.1 mag of extinction (a typical average value in disk galaxies, Kennicutt 1998b). The other markings are as in the left panel.

In the left panel of the fourth row, we show the observed SFE for the galaxy. We use the same color scheme as in §4, i.e., magenta points indicate rings where $\Sigma_{\rm H2} > \Sigma_{\rm HI}$, blue points show rings where $\Sigma_{\rm H2} < \Sigma_{\rm HI}$, and red arrows indicate upper limits. The ensemble of points in this panel combine to form Figure 1. Dashed, dotted, and dash-dotted lines show the SFE predicted following the method described in §6 with no threshold applied (the thresholds appear in the right panel). The other markings are as in the panels on the third row.

In the right panel of the fourth row we show azimuthally averaged values for thresholds described in §2.2. We expect widespread star formation (conditions are "supercritical") where the value of a profile is below 1 (the shaded area) and isolated or nonexistent star formation (conditions are "subcritical") above 1. We plot the Toomre Q parameter for a gas disk, $Q_{\rm gas}$ (black), and for a gas disk in the presence of stars, $Q_{\rm stars+gas}$ (green). We show the shear criterion described by Hunter et al. (1998a), $\Sigma_{\rm crit,A}/\Sigma_{\rm gas}$ in purple and the condition for the formation of a cold phase given by Schaye (2004), $\Sigma_{\rm S04}/\Sigma_{\rm gas}$ in orange. The other markings are as in the panels on the third row.

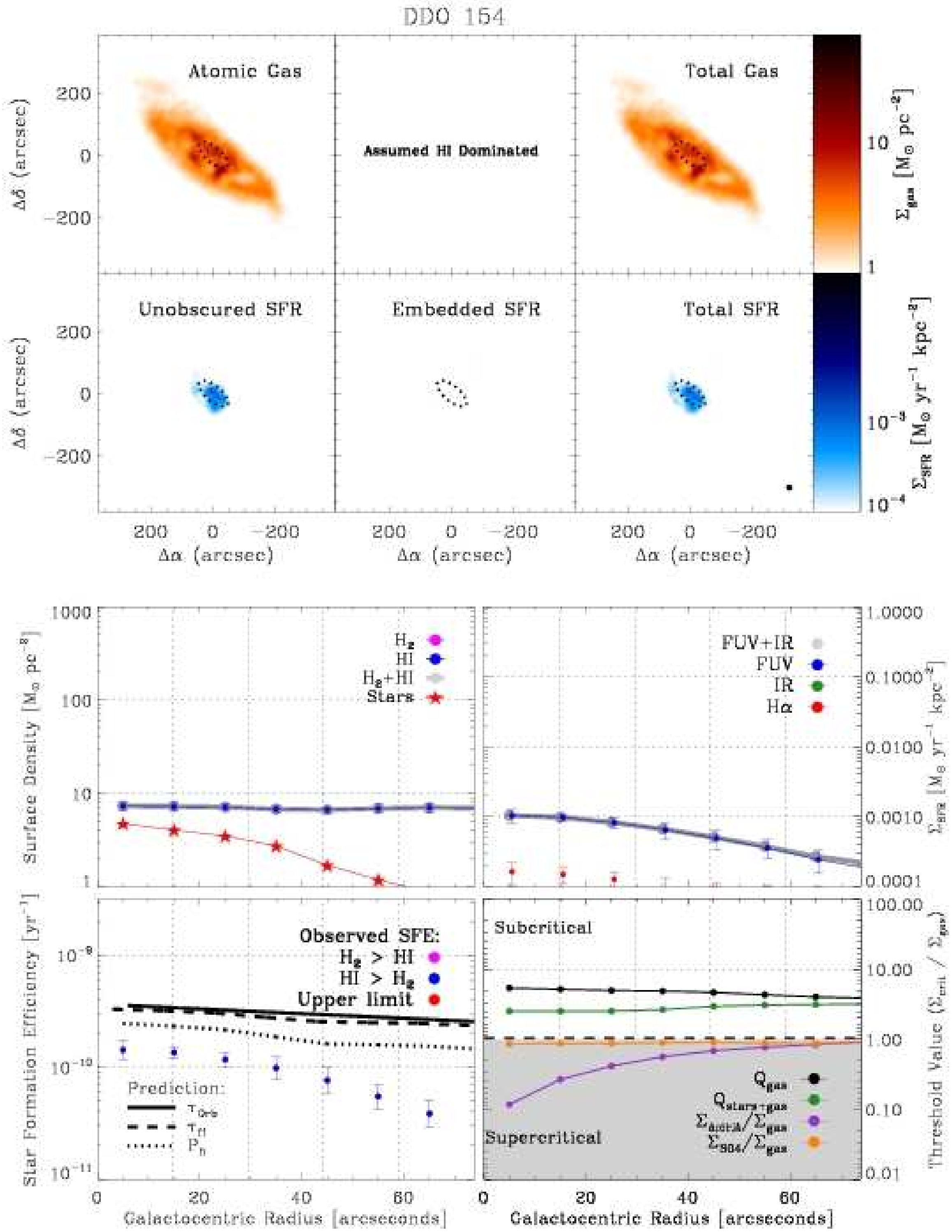

FIG. F1.— Atlas of data and calculations for DDO 154.

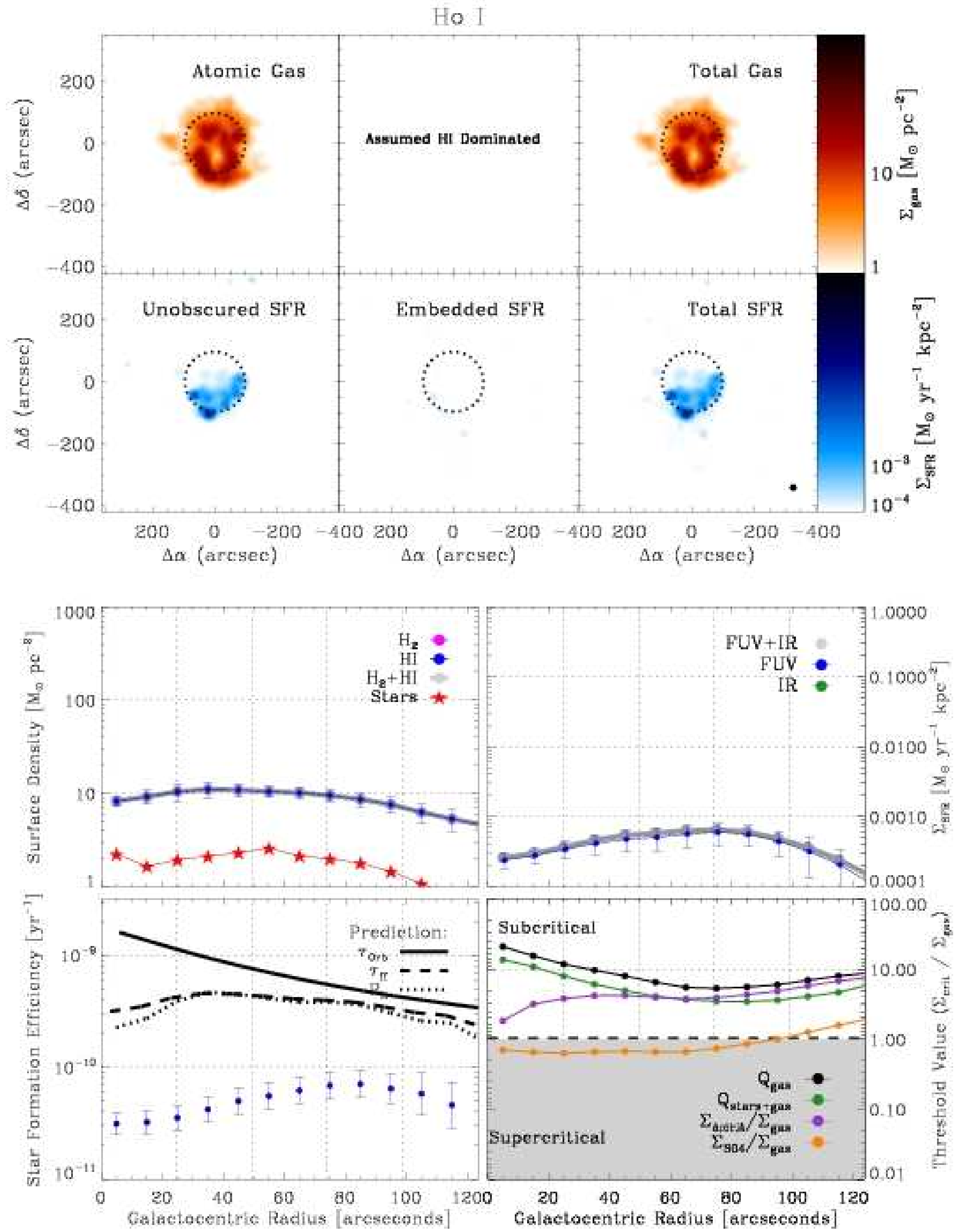

FIG. F.— Atlas of data and calculations for Holmberg I.

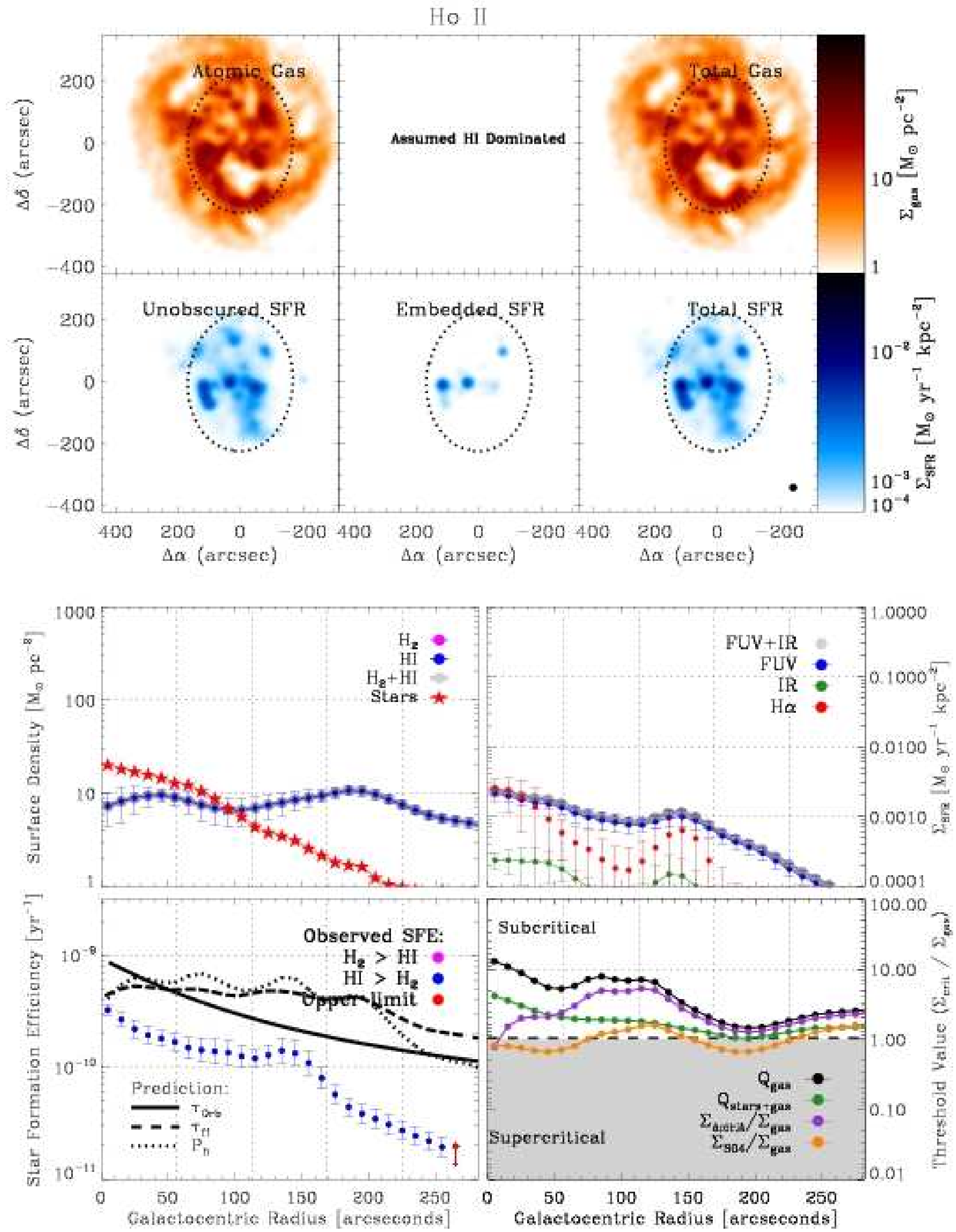

FIG. F.— Atlas of data and calculations for Holmberg II.

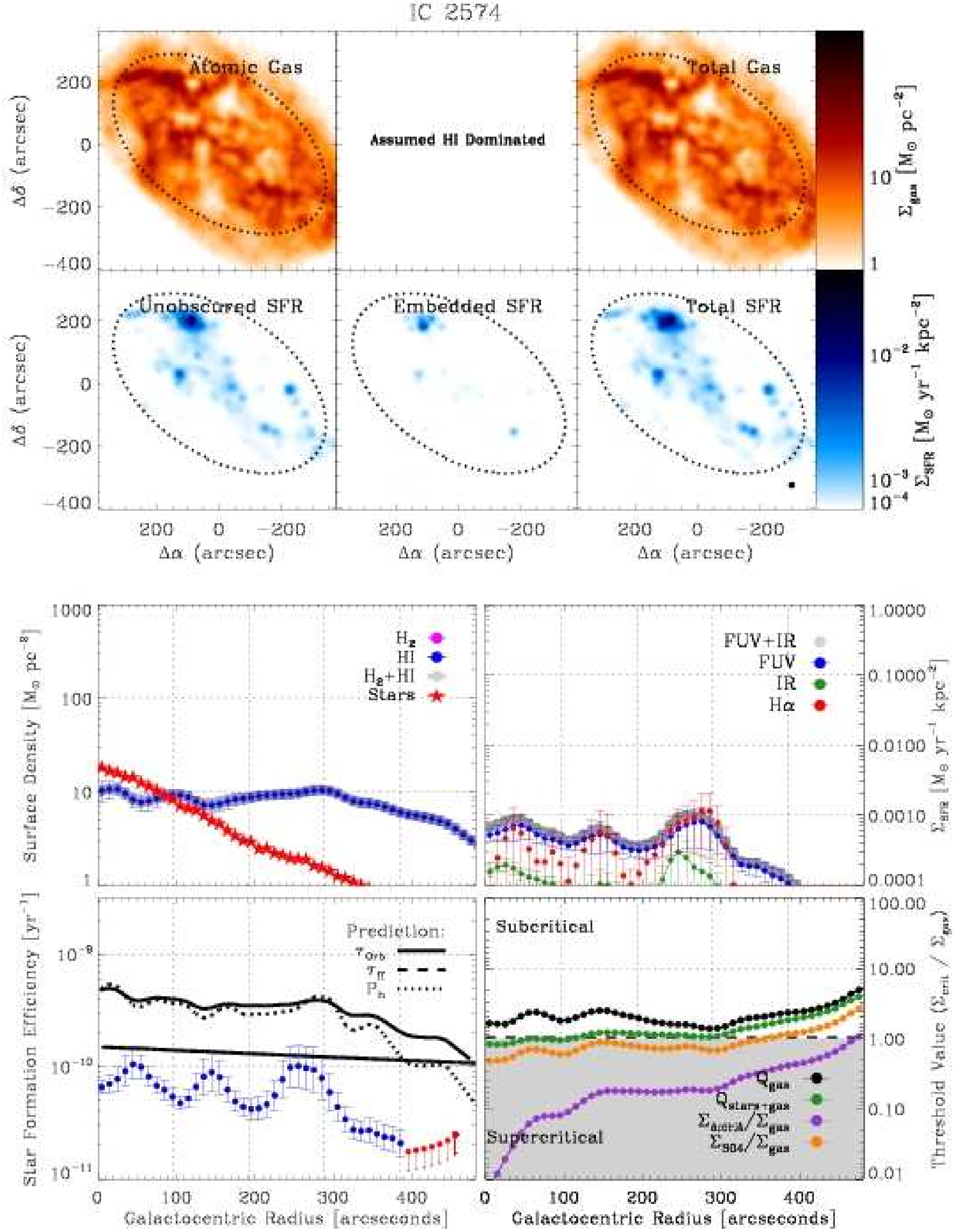

FIG. F.— Atlas of data and calculations for IC 2574.

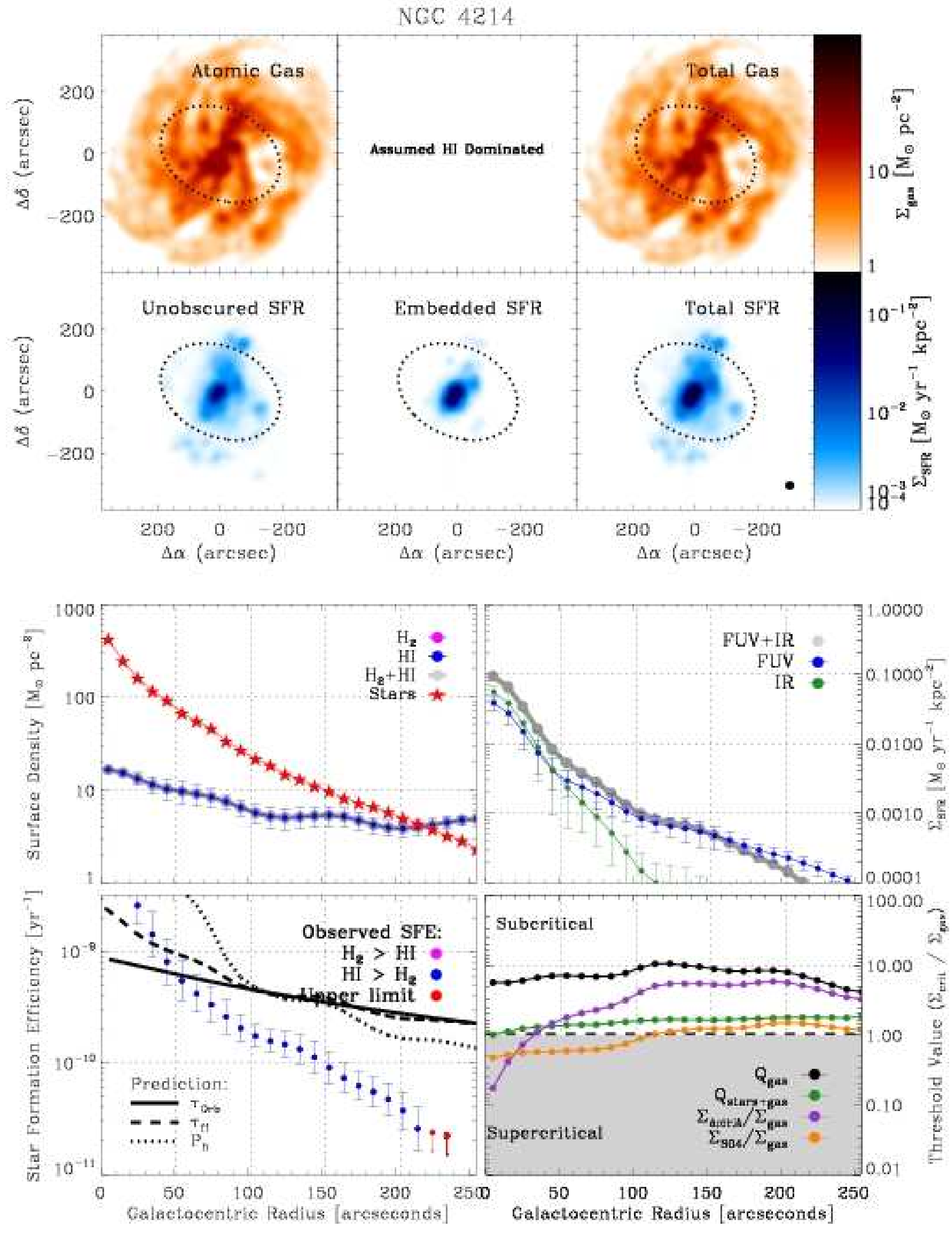

FIG. F.— Atlas of data and calculations for NGC 4214.

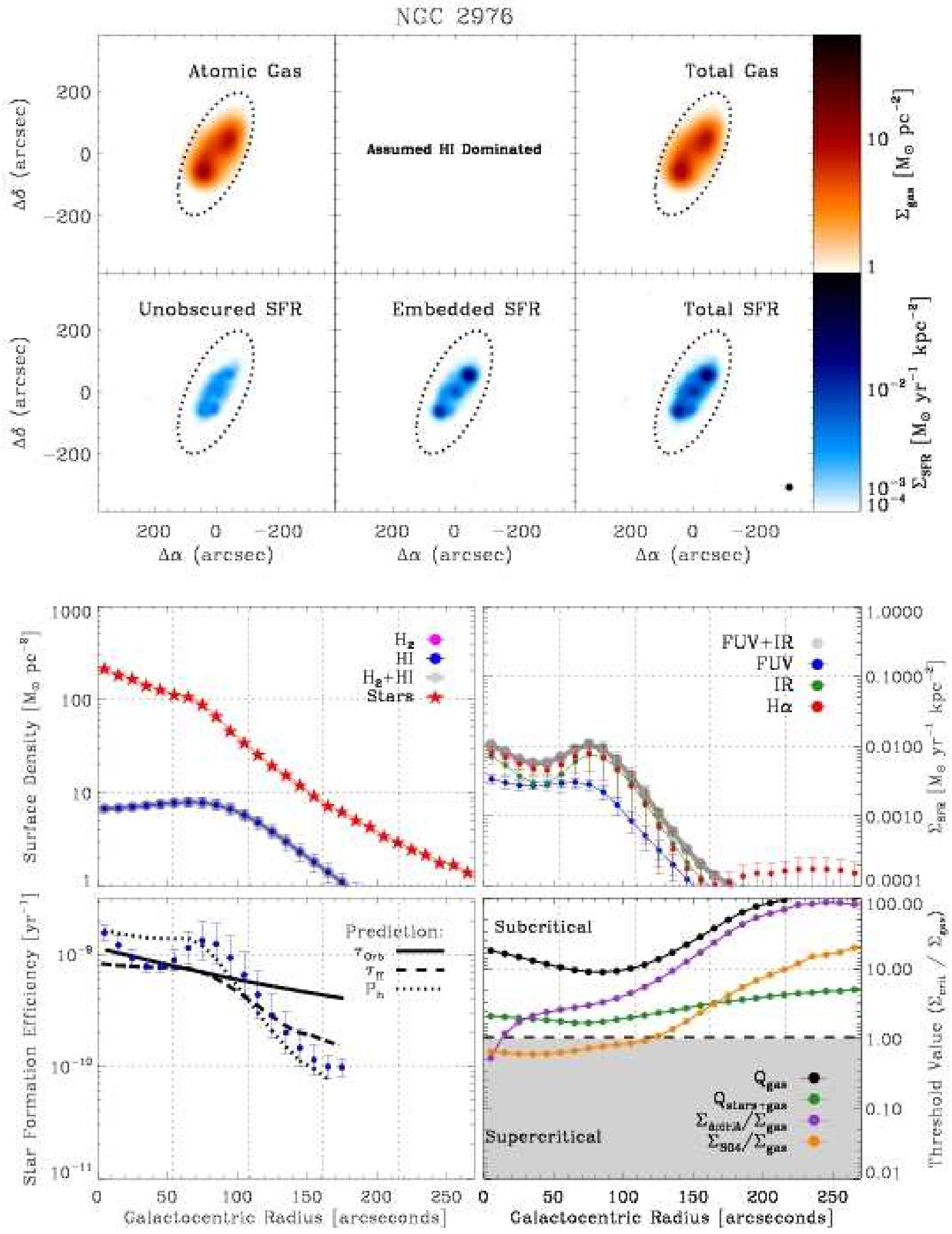

FIG. F.— Atlas of data and calculations for NGC 2976.

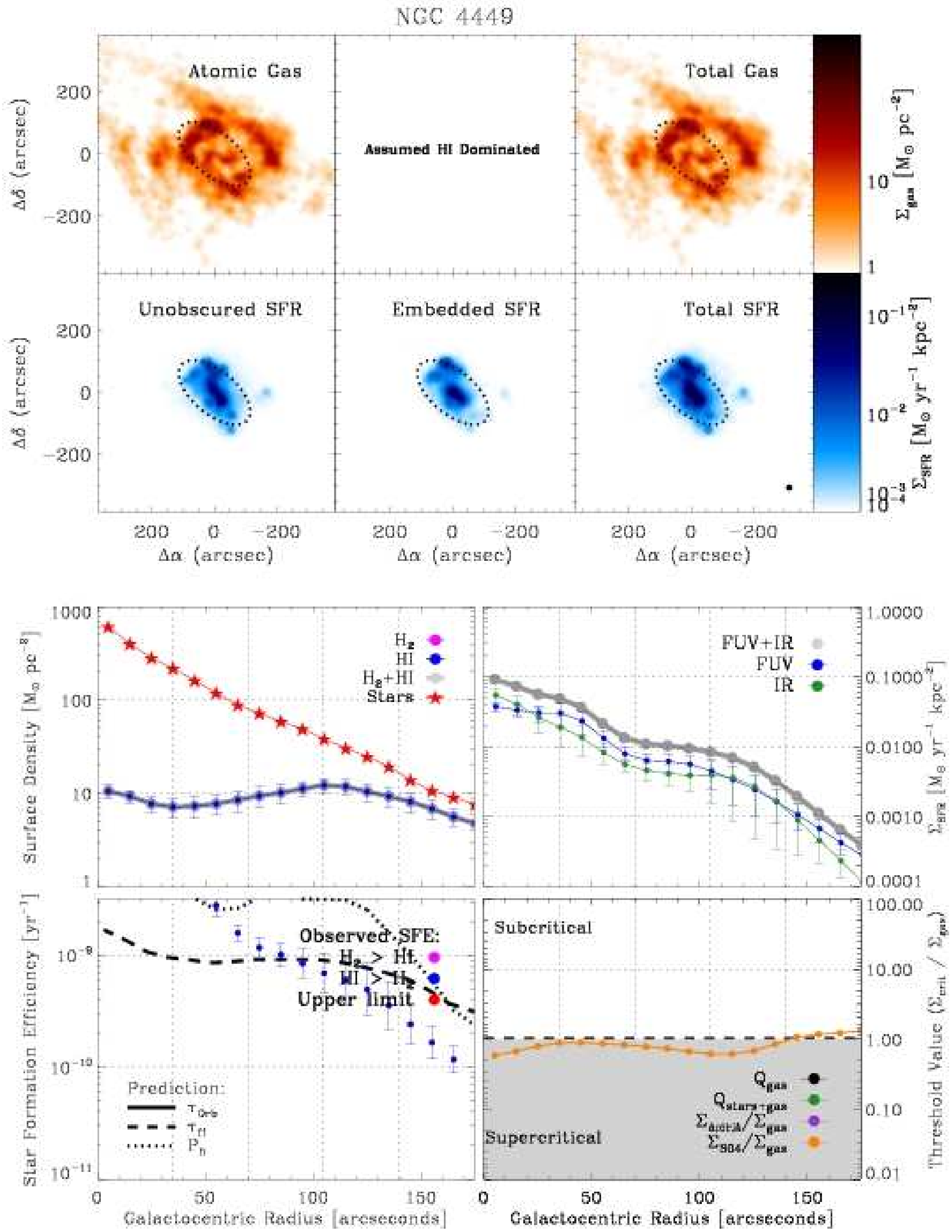

FIG. F.— Atlas of data and calculations for NGC 4449.

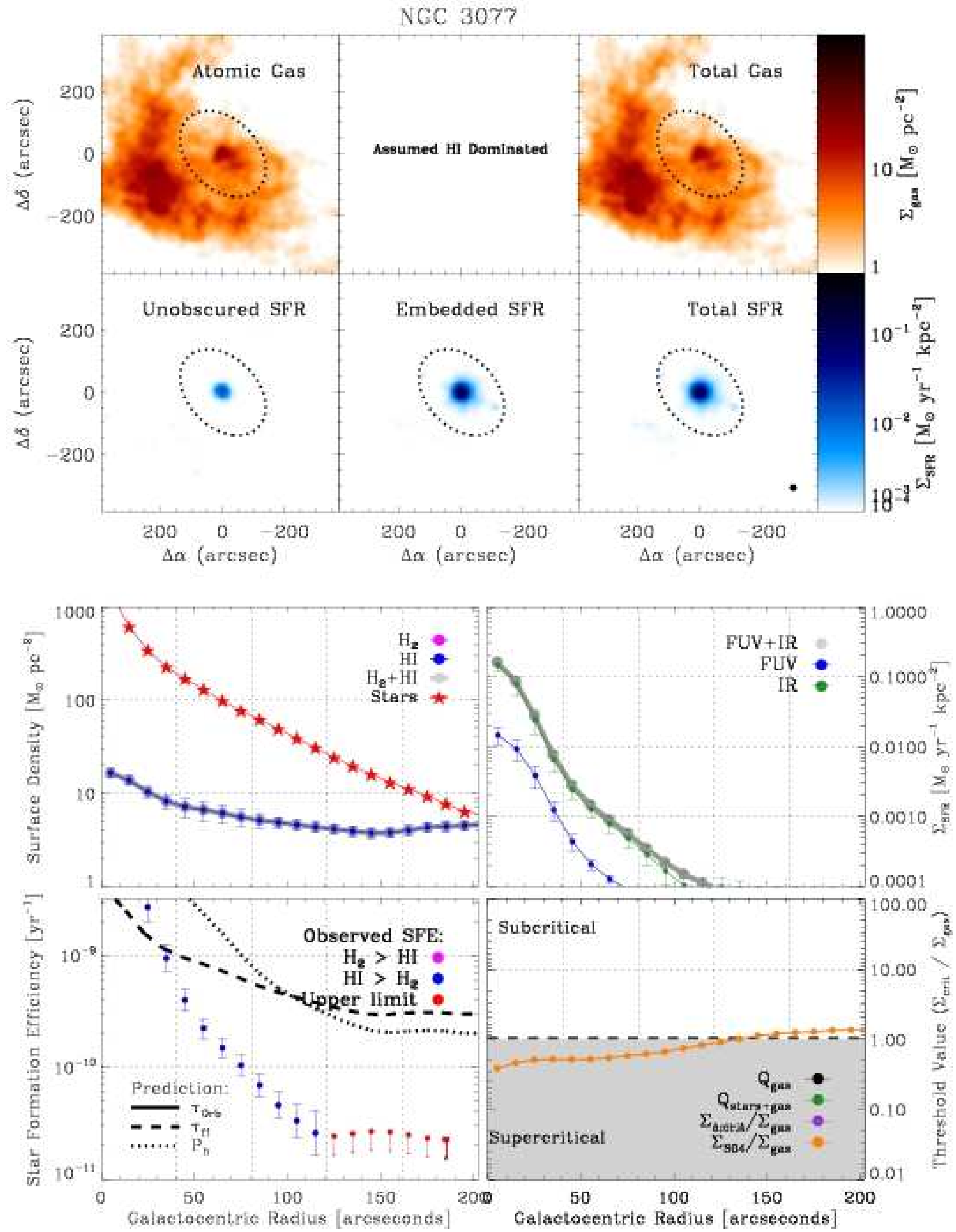

FIG. F.— Atlas of data and calculations for NGC 3077.

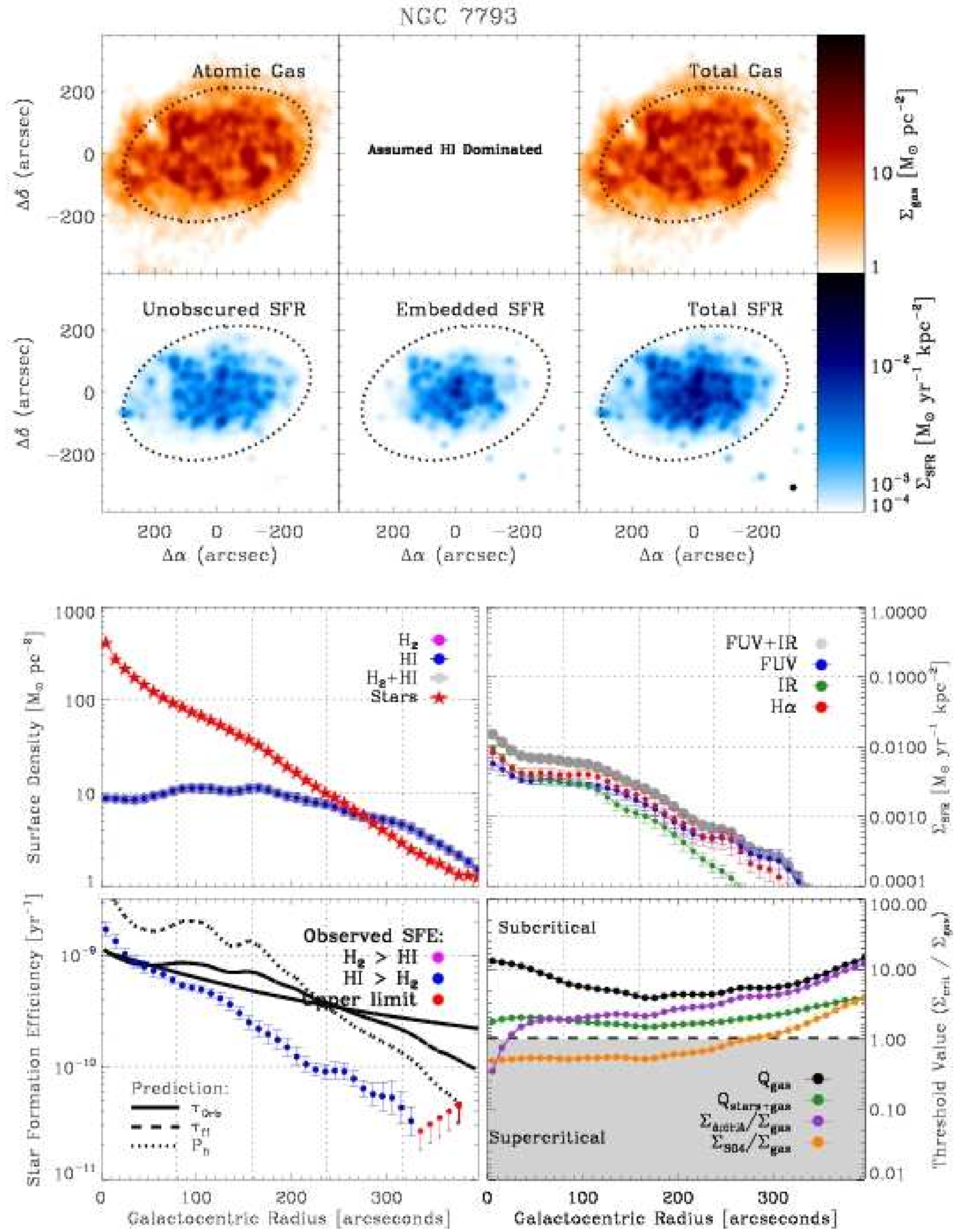

FIG. F.— Atlas of data and calculations for NGC 7793.

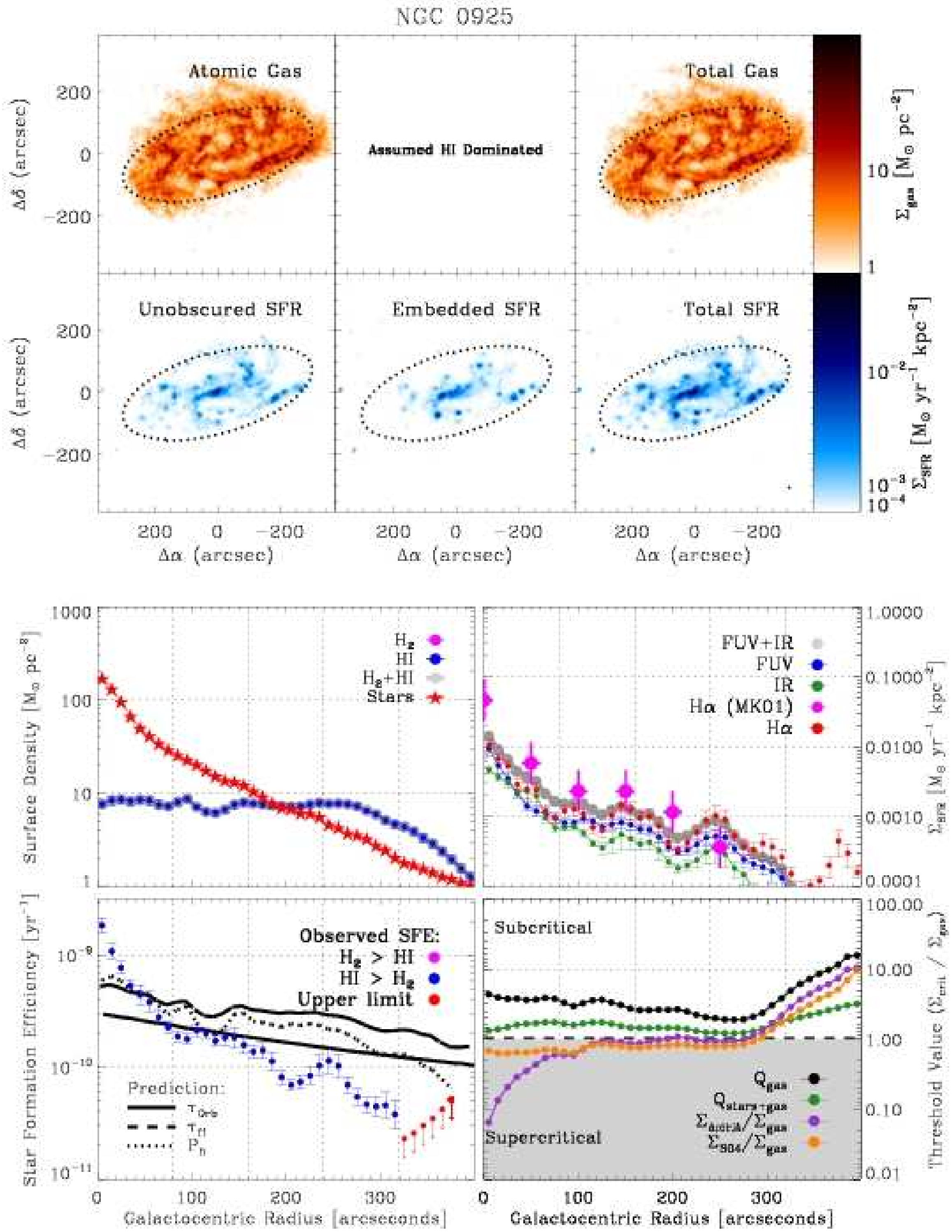

FIG. F.— Atlas of data and calculations for NGC 925.

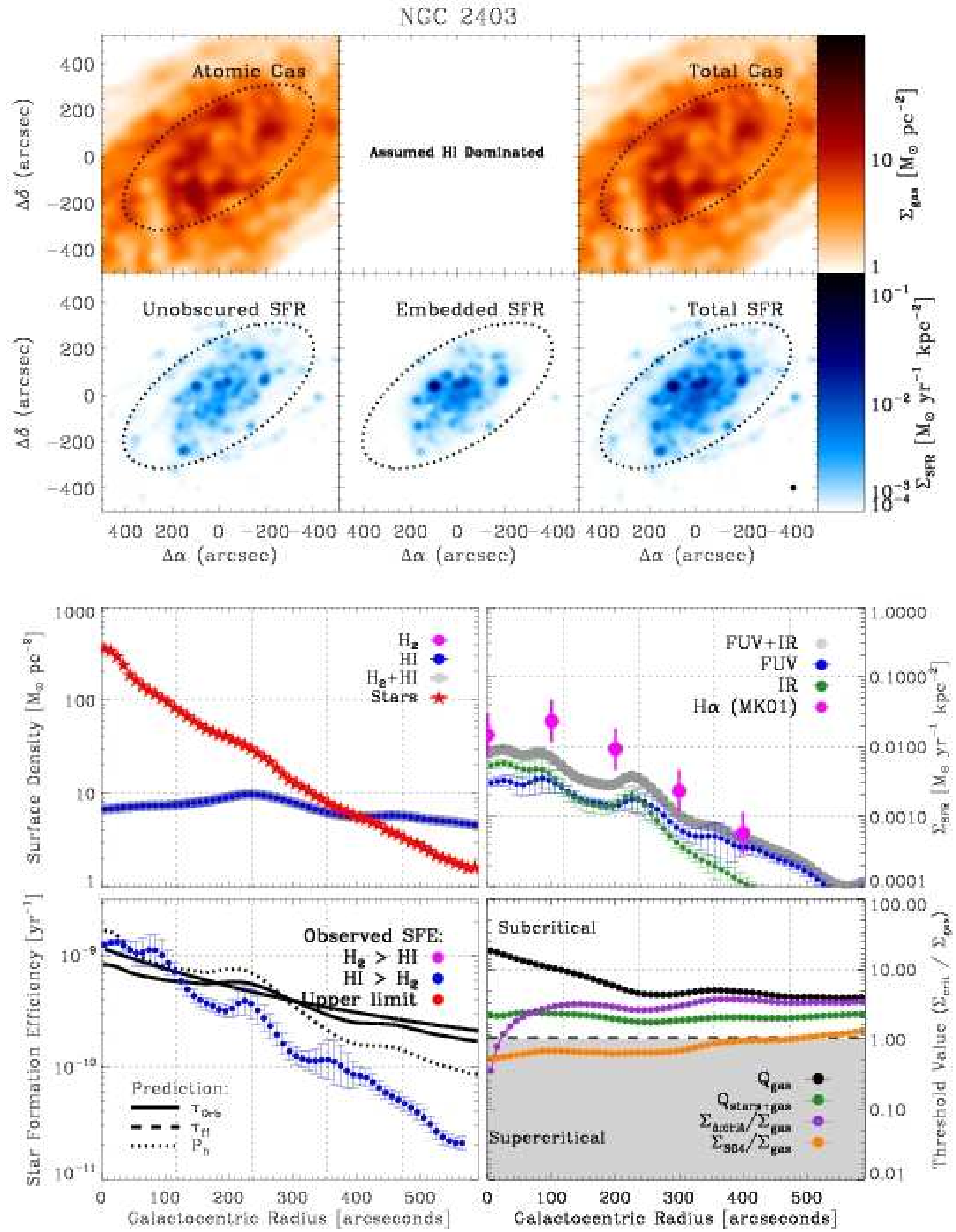

FIG. F.— Atlas of data and calculations for NGC 2403.

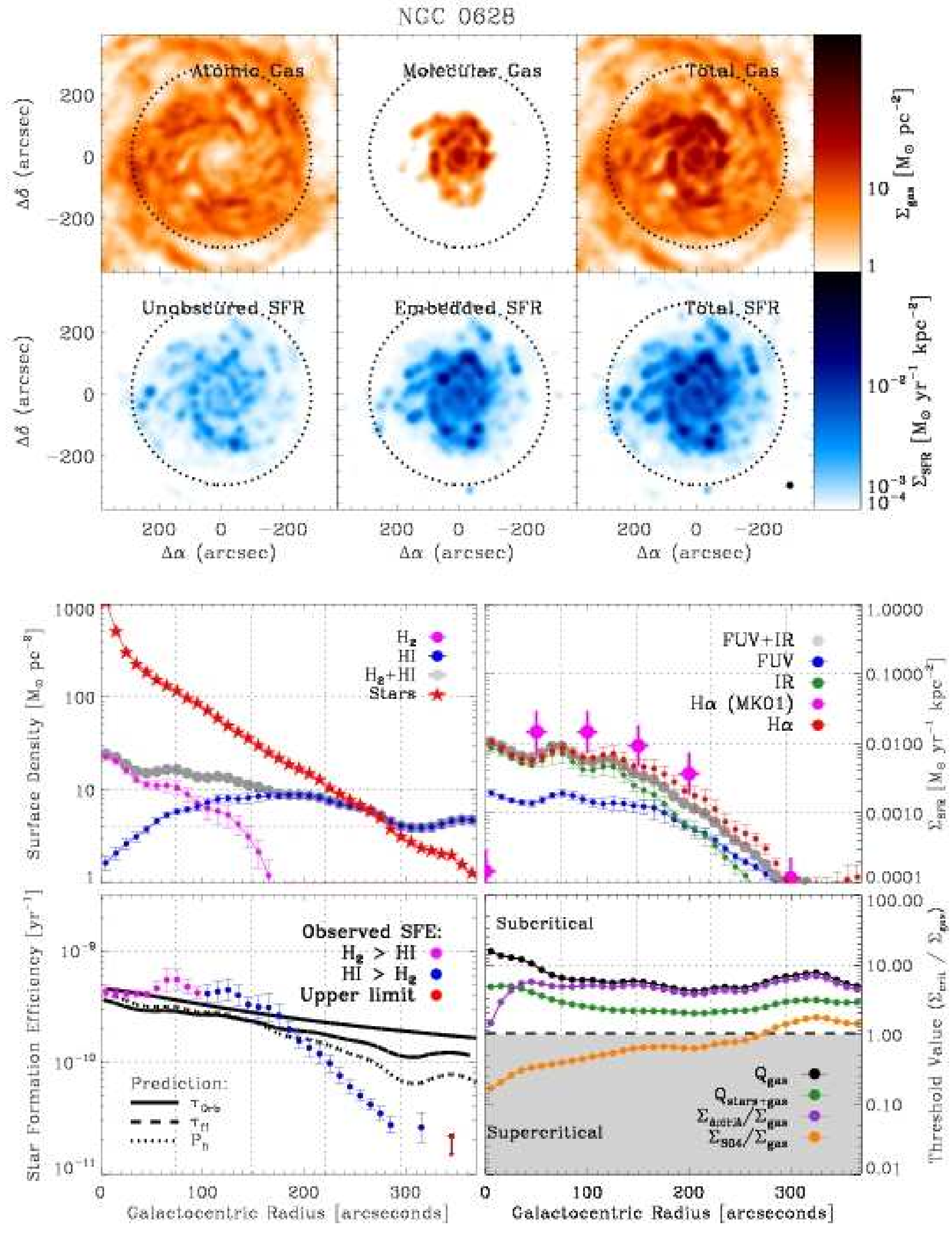

FIG. F.— Atlas of data and calculations for NGC 628.

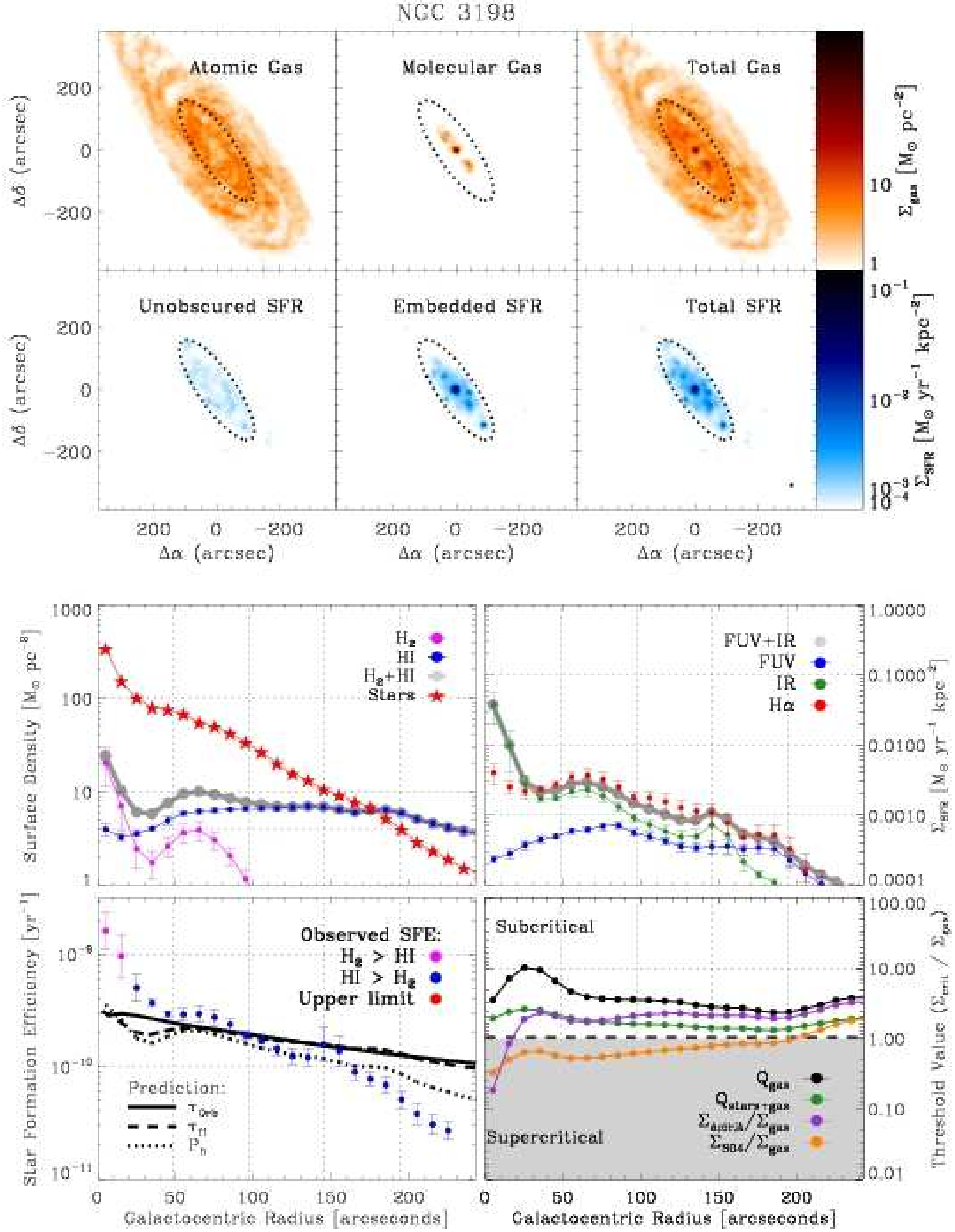

FIG. F.— Atlas of data and calculations for NGC 3198.

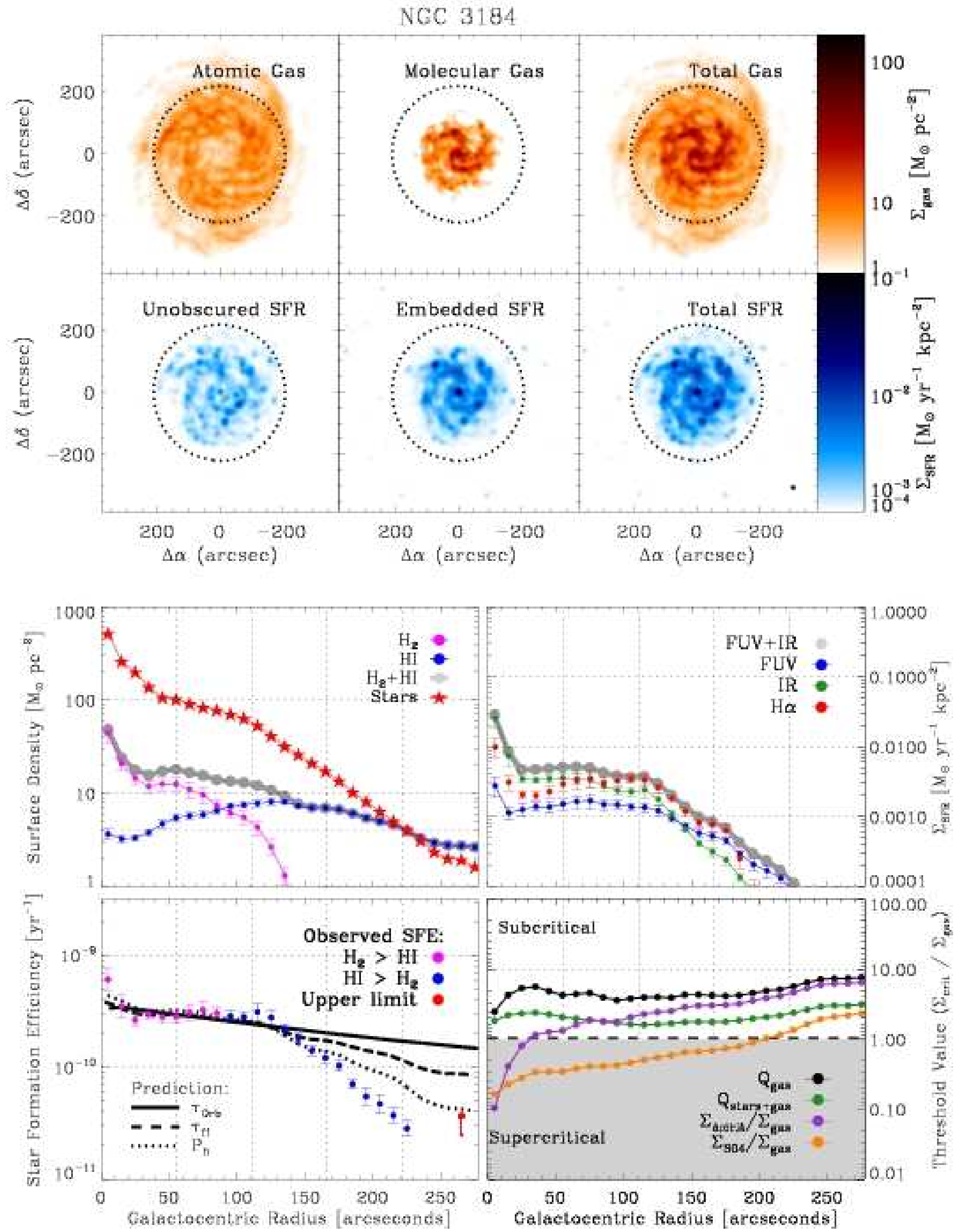

FIG. F.— Atlas of data and calculations for NGC 3184.

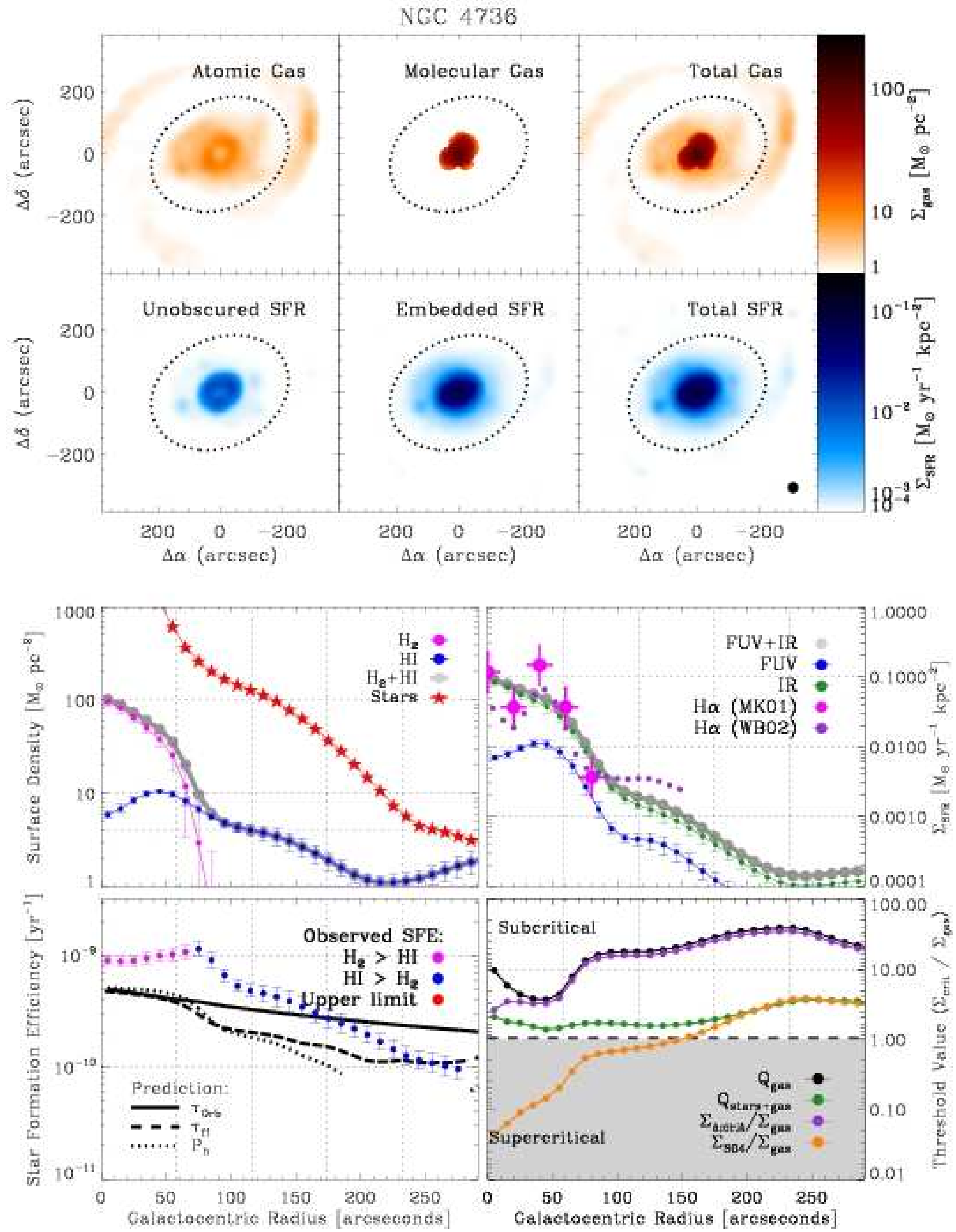

FIG. F.— Atlas of data and calculations for NGC 4736.

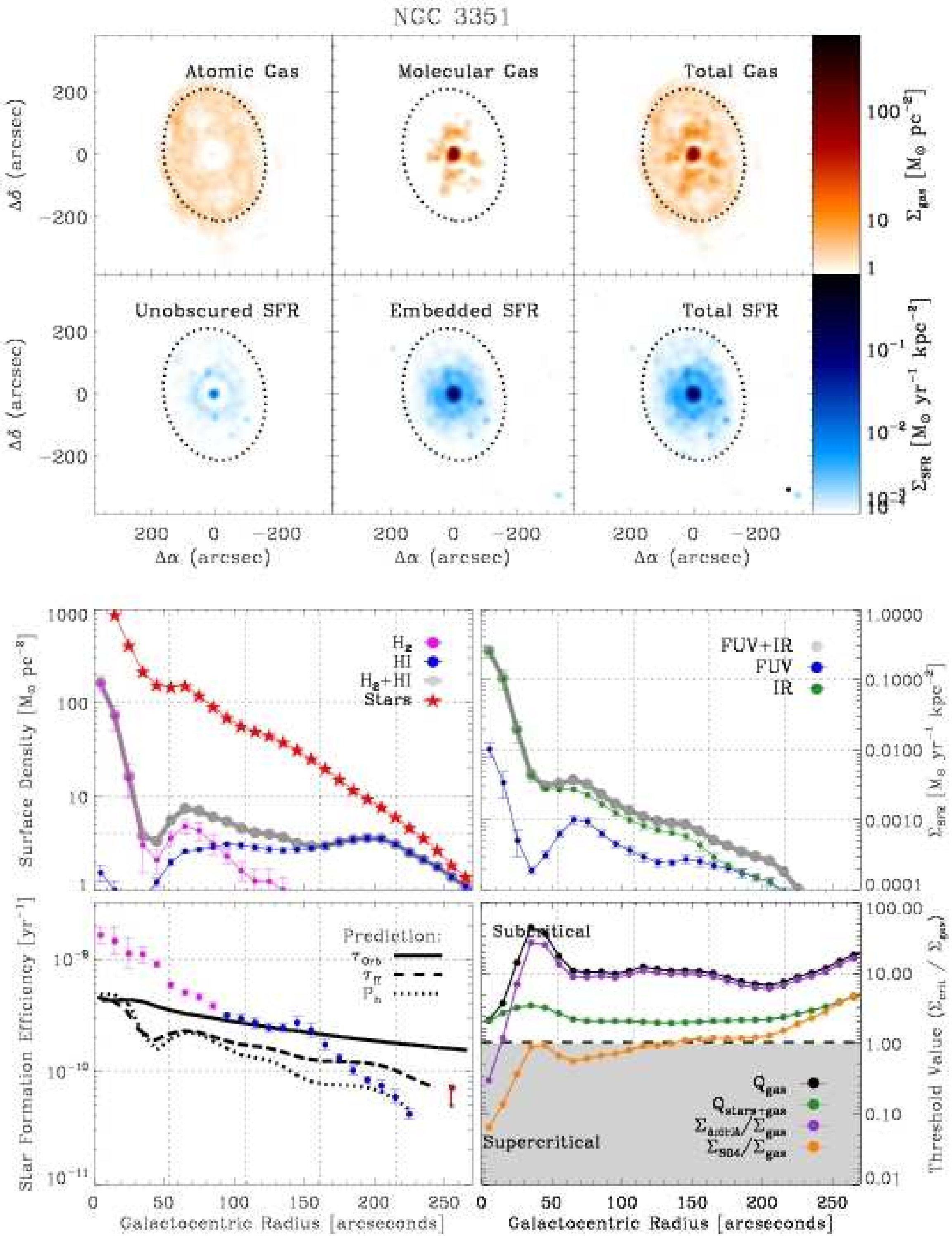

FIG. F.— Atlas of data and calculations for NGC 3351.

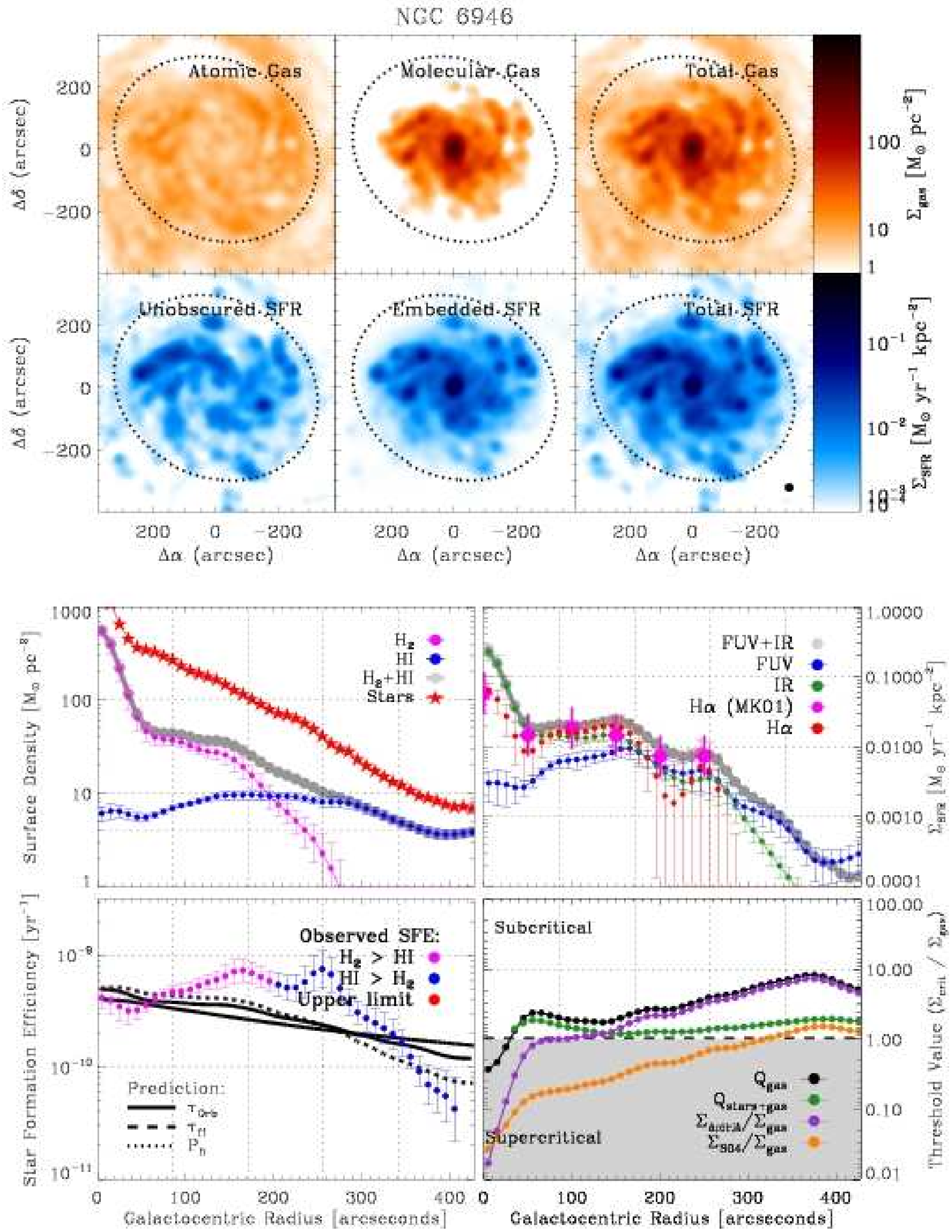

FIG. F.— Atlas of data and calculations for NGC 6946.

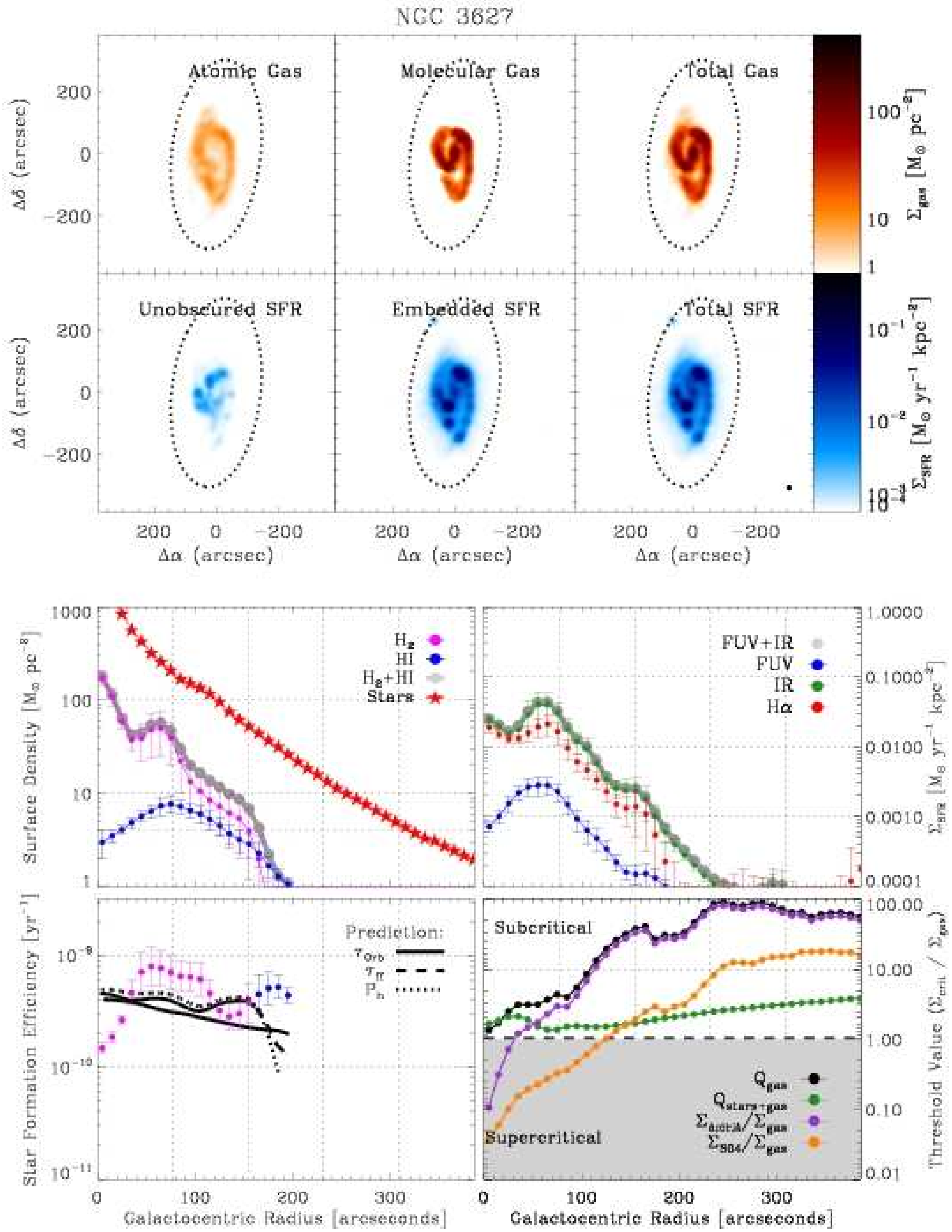

FIG. F.— Atlas of data and calculations for NGC 3627.

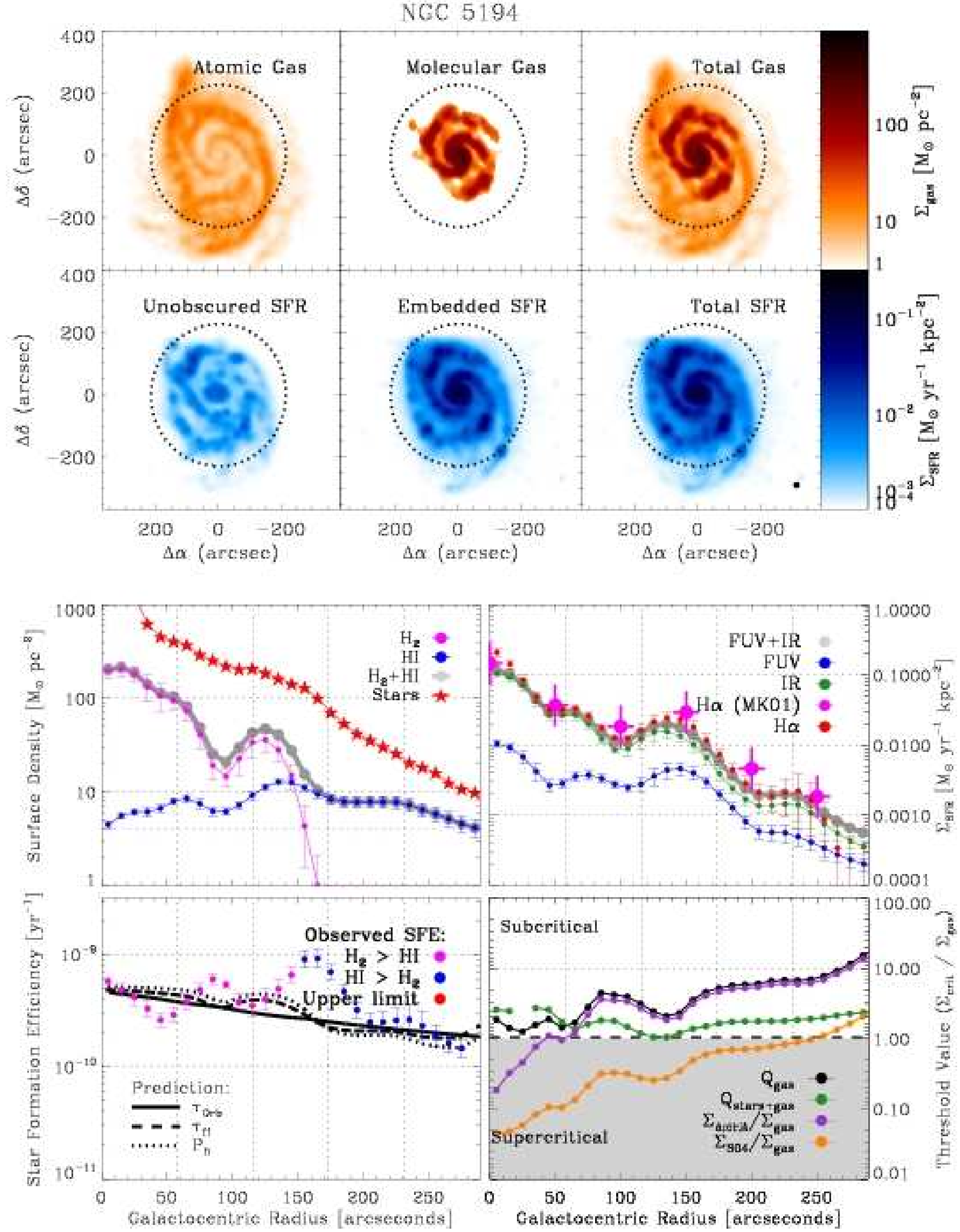

FIG. F.— Atlas of data and calculations for NGC 5194.

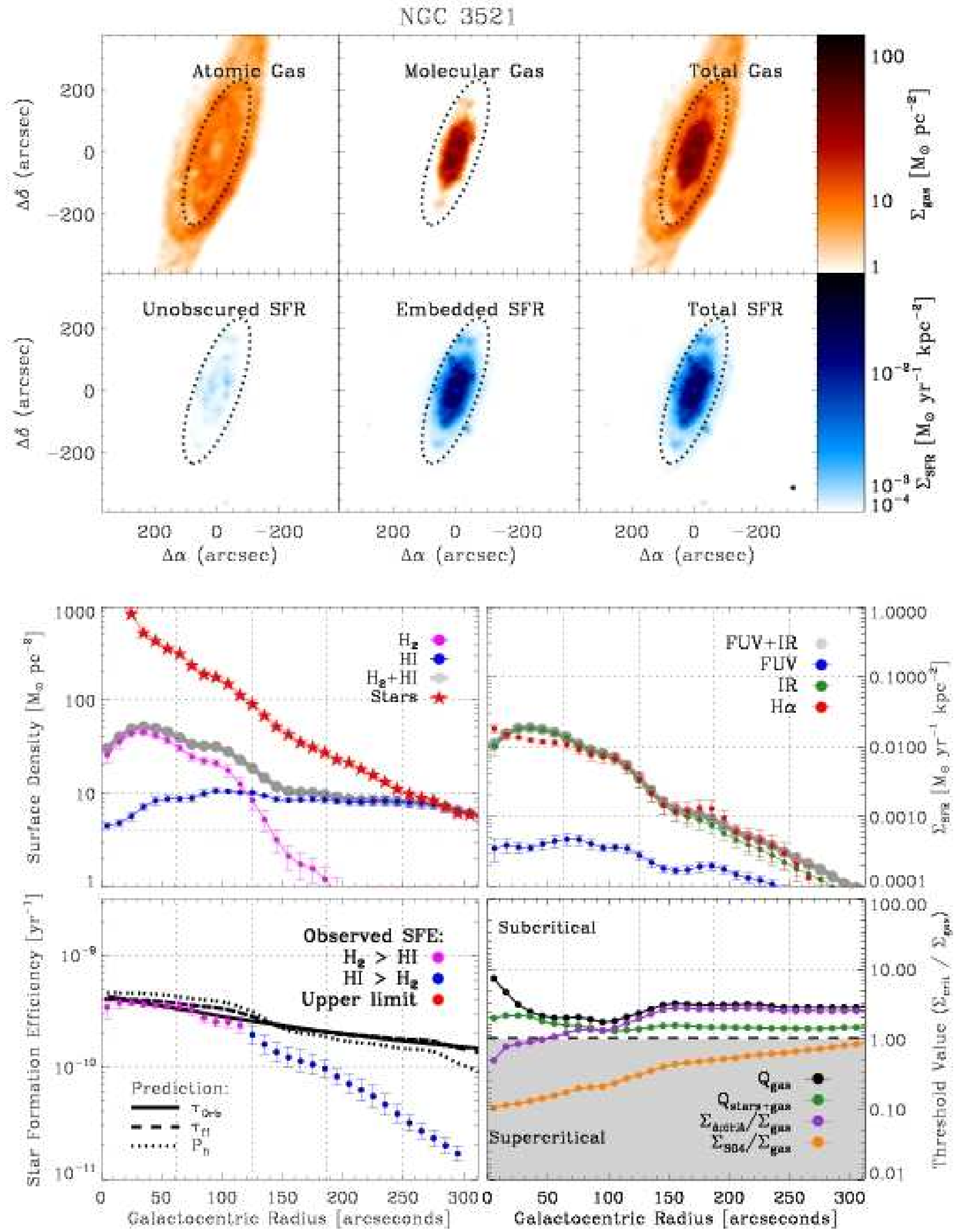

FIG. F.— Atlas of data and calculations for NGC 3521.

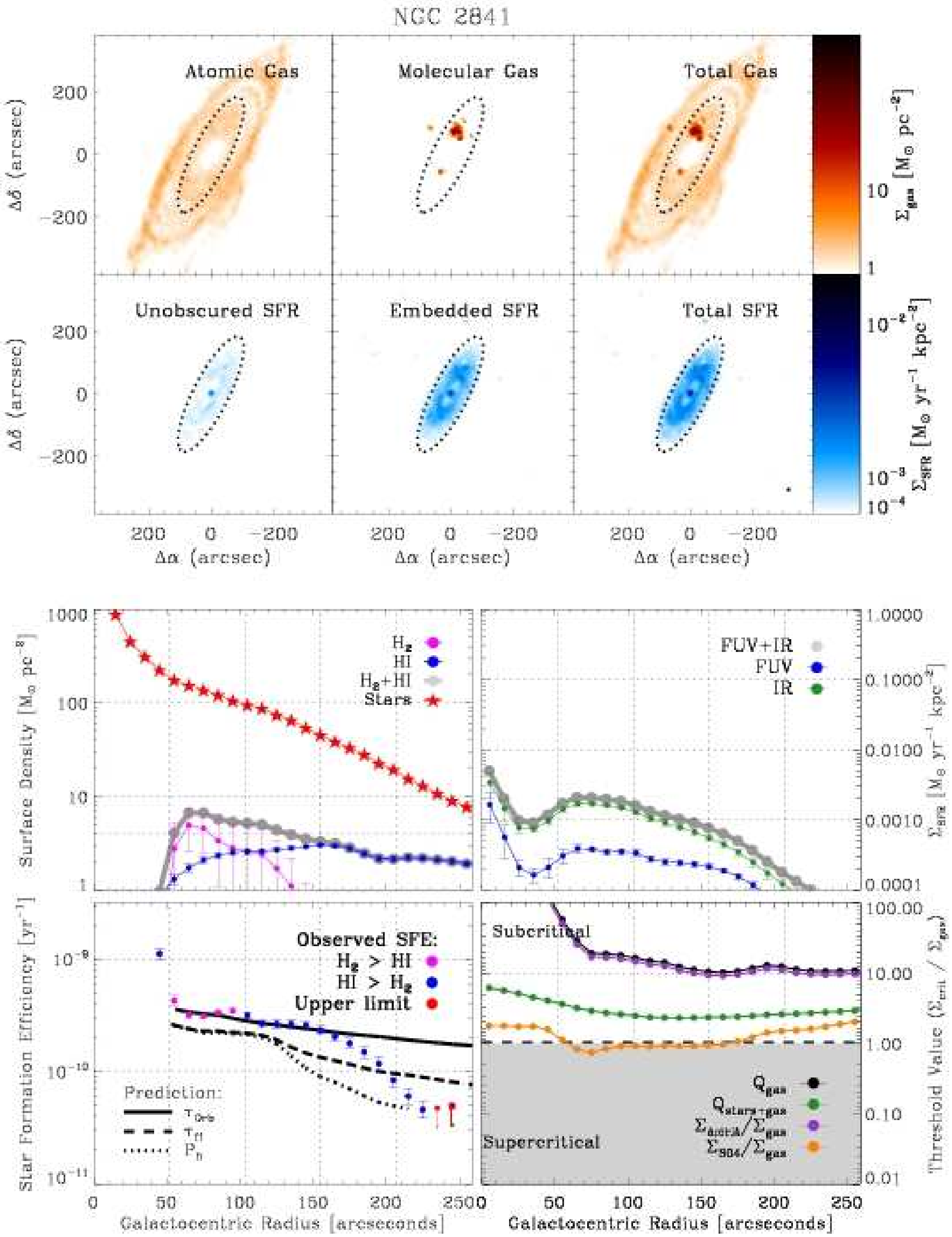

FIG. F.— Atlas of data and calculations for NGC 2841.

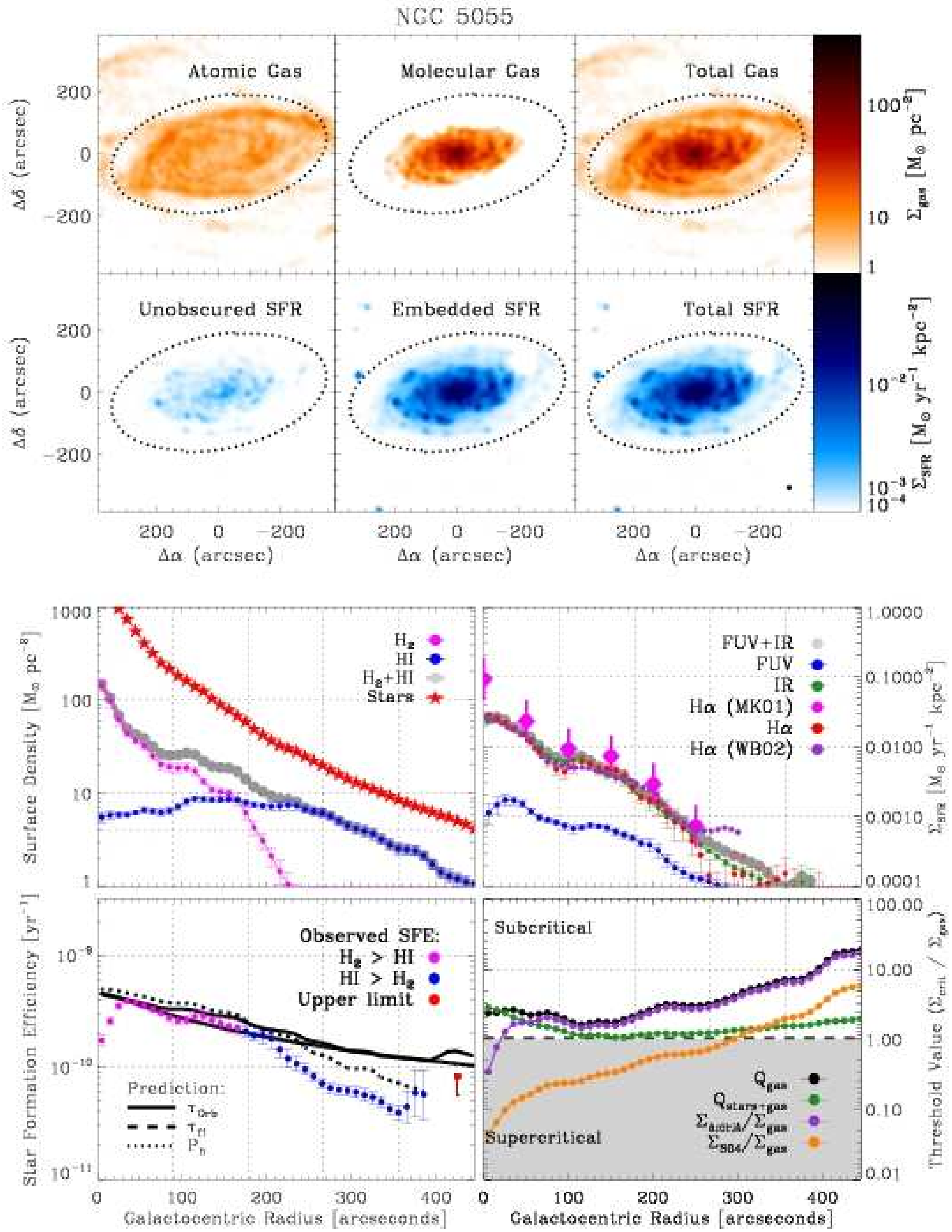

FIG. F.— Atlas of data and calculations for NGC 5055.

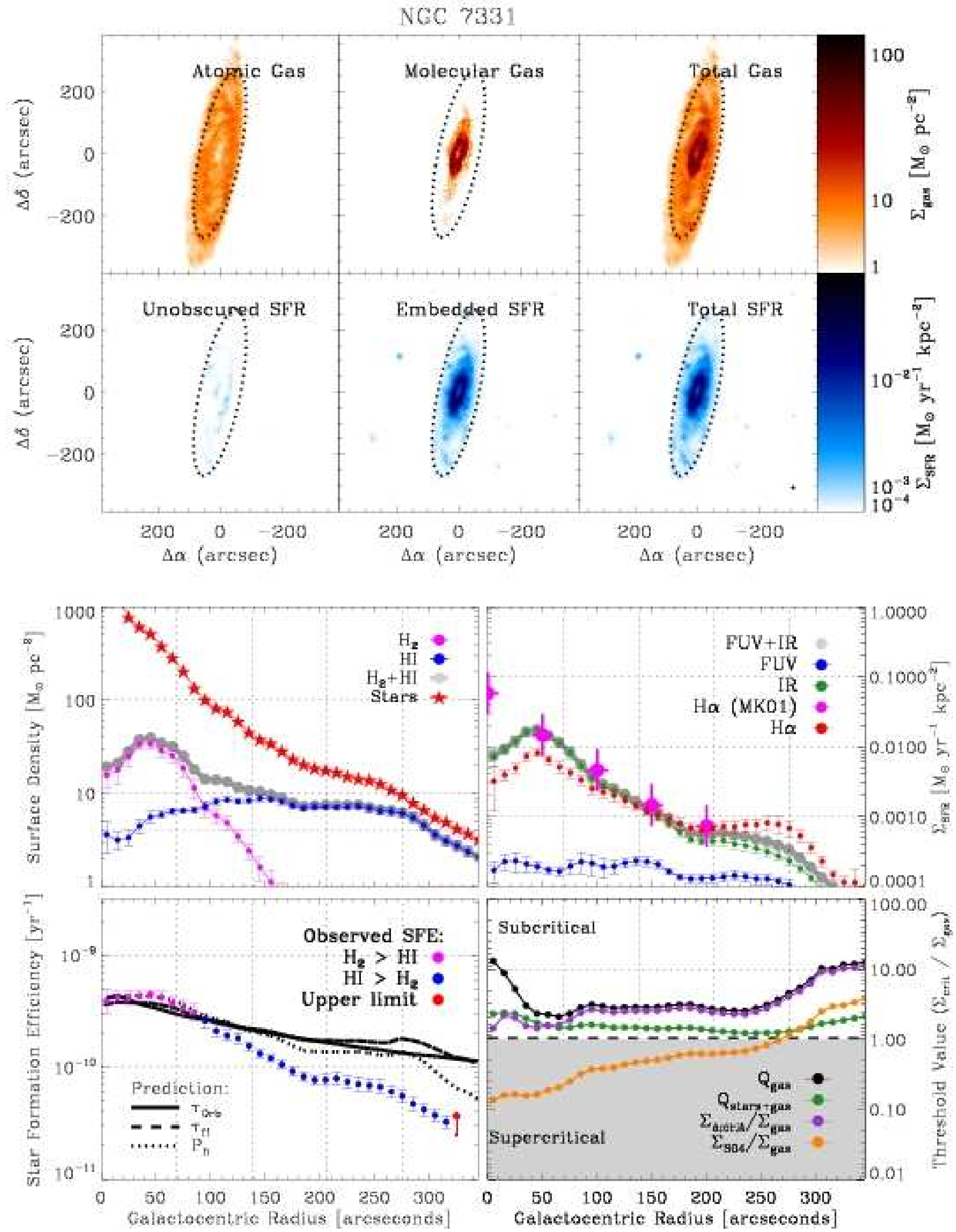

FIG. F.— Atlas of data and calculations for NGC 7331.